DEUTSCHES ELEKTRONEN-SYNCHROTRON

DESY 94–022
February 1994

HERA Physics

G. Wolf

Deutsches Elektronen-Synchrotron DESY, Hamburg

ISSN 0418-9833

NOTKESTRASSE 85 - 22603 HAMBURG

To be sure that your preprints are promptly included in the HIGH ENERGY PHYSICS INDEX, send them to (if possible by air mail):

DESY
Bibliothek
Notkestraße 85
22603 Hamburg
Germany

DESY-IfH
Bibliothek
Platanenallee 6
15738 Zeuthen
Germany

DESY 94-022
February 1994

ISSN 0418-9833

HERA Physics*

Günter Wolf

Deutsches Elektronen Synchrotron DESY
Hamburg, Germany

1 INTRODUCTION

Scattering experiments have been marvelously successful in unravelling the structure of matter. The basic concept is quite simple. A point - like and energetic test particle is scattered on the probe and its angular and energy distribution are measured. An early example is the experiment of Rutherford and his coworkers Geiger and Marsden (1909 - 1911) who scattered α - particles on a metal foil. The observation of occasional scatterings at large angles led Rutherford to the assumption of a hard core in the atom (1911). The experimental verification of his scattering formula (1911) by Geiger and Marsden (1913) resulted in the conclusion that the atom has a positively charged core with a radius of less than 30 fm.

The structure of the nucleon has been explored mostly with lepton beams. Elastic scattering of electrons with beam energies of the order of 1 GeV showed that the proton is an extended object with a radius of 0.8 fm (see e.g. Janssens et al. 1966). Inelastic scattering of 20 GeV electrons on nucleons (SLAC - MIT, see e.g. Taylor 1969) revealed approximate scaling of the structure functions (Bjorken 1969) resulting from scattering on charged, point - like constituents in the nucleon as explained by the quark - parton model (Feynman 1972). The observation of logarithmic violations of scaling (Fox et al. 1974, Watanabe et al. 1975, Chang et al. 1975, SLAC - MIT 1974, 1976), which became particularly clear with beam energies of several hundred GeV, was instrumental for the formulation of Quantum Chromodynamics, QCD (Fritzsch and Gell-Mann 1972, Fritzsch et al. 1973, Weinberg 1973, Gross and Wilczek 1973).

The object size Δ that can be resolved in the scattering process is determined by the four momentum Q transferred to the probe particle. From the uncertainty relation it follows that $\Delta \approx 1/Q$. Better resolution requires larger momentum transfers and hence higher energies. This is best achieved in a storage ring where the test and the probe particles collide head-on. With the electron-proton collider HERA at DESY c.m. energies of 300 GeV can be reached compared to 30 GeV in current fixed target experiments. The result is a vast increase in phase space and physics potential for lepton-nucleon scattering, the maximum momentum transfer Q rising by a factor of ten and the energy transfer ν by a factor of hundred.

The physics that can be done at an electron - proton collider such as HERA has been developed in numerous theoretical and experimental studies. An introduction can be found in the proceedings of two recent workshops held in 1987 (Peccei) and 1991 (Buchmüller and Ingelman).

* Lectures given at the 42nd Scottish Universities Summer School in Physics, 1993

The HERA project (HERA 1981, Wiik 1982, 1992, Voss 1988) was approved in 1984. Operation of HERA for physics started in 1992 with the two large general purpose detectors H1 (1986) and ZEUS (1986) taking data. A third experiment, HERMES (1990), which has been approved recently for the measurement of the nucleon spin structure by colliding the polarized electron beam with a gas jet of polarized nucleons, is under construction. A fourth experiment, HERA-B (HERA-B 1992), which aims at measuring CP violation in the $b\bar{b}$ system by scattering beam protons on a fixed target, is under discussion.

These lectures are intended for the newcomer to the field and focus on results obtained by H1 and ZEUS.

2 THE HERA COLLIDER

2.1 Layout

The layout of HERA is shown in fig.1. Two separate magnet systems guide the e and p beams around the 6.3 km long ring. DESY and PETRA serve as injectors. There are four experimental halls, two of which are occupied by H1 and ZEUS. A third hall has been allocated to HERMES.

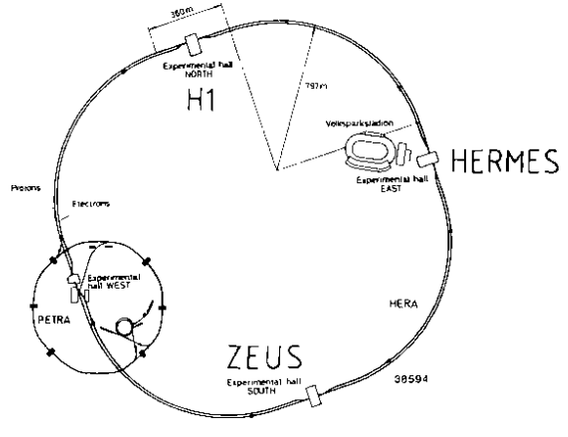

Fig. 1 Layout of HERA

Table 1 shows some of the parameters of the collider. In order to maximize the luminosity up to 210 bunches of particles can be stored for each beam. The time interval between bunches is 96ns.

Table 1 HERA design parameters

	electron ring		proton ring
circumference		6336 m	
energy	30 GeV		820 GeV
e - p c.m. energy		314 GeV	
magnetic bending field	0.164 T		4.682 T
bending radius of dipoles	610 m		584 m
circulating current	60 mA		160 mA
number of particles/beam	$0.8 \cdot 10^{13}$		$2.1 \cdot 10^{13}$
number of bunch buckets	220		220
number of bunches	210		210
current/bunch	0.3 mA		0.8 mA
time between beam crossings		96 ns	
luminosity		$1.5 \cdot 10^{31}$ cm^{-2}s^{-1}	
specific luminosity		$3.3 \cdot 10^{29}$ cm^{-2}s^{-1}mA^{-2}	
polarization time at E_e = 30 GeV	25 min		

2.2 Performance

For the first physics runs the beam energies chosen were 26.67 GeV for electrons and 820 GeV for protons. Since May 1992, when H1 and ZEUS observed the first ep collisions in their central detectors, data were taken in three running periods, July 1992, September - October 1992 and July - October 1993. Over this time, beam currents and luminosity were gradually increased. In 1993 HERA was operated with 90 bunches per beam and typical (maximum) beam currents of 13 (25) mA for electrons and (13) 20 mA for protons yielding a typical (maximum) luminosity of $0.7 \cdot 10^{30}$cm^{-2}s^{-1} ($1.5 \cdot 10^{30}$cm^{-2}s^{-1}). The maximum specific luminosity observed was $6 \cdot 10^{29}$ cm^{-2}s^{-1}mA^{-2}, which is above the design value. The evolution of the luminosity during the three running periods is shown in fig. 2. The total integrated luminosity per experiment reached 33 nb^{-1} in 1992 and 600 nb^{-1} in 1993.

After coasting for some time the electrons become polarized with spins being antiparallel to the direction of the bending field as a result of the Sokholov - Ternov effect (Sokholov and Ternov 1964). The build - up time for the polarization P(t) is determined by the synchrotron radiation and is given by

$$P(t) = P_0 (1 - \exp(-t/t_p))$$

$$t_p = 98\, r^2\, R\, E^{-5} \qquad (1.1)$$

with $P_0 = 92\%$, t_p in s, r the bending radius in m, R the average radius in m and E the electron beam energy in GeV. This prediction holds for a perfect machine. Already small imperfections, e.g. in the magnet lattice, may produce depolarization effects and make the depolarization time shorter than the build-up time thereby reducing the polarization.

Electron beam polarization was observed for the first time in Fall of 1991 at the level of P = 5 - 9%. Studies of the polarization (Barber et al. 1992, 1993) were performed at 26.67 GeV also in parallel to data taking of H1 and ZEUS. After

realignment of magnets and empirical tuning of correction magnets with the guidance from a tracking program polarization values close to 70% could be attained (fig. 3).

For particle physics electrons of definite helicity (left - and right-handed) rather than with transverse polarization are needed. This can be achieved with the help of a pair of spin rotators which was designed and built (Buon and Steffen 1985) and is being installed in hall East for HERMES. Given satisfactory performance, the interaction regions of H1 and ZEUS will also be equipped with spin rotators.

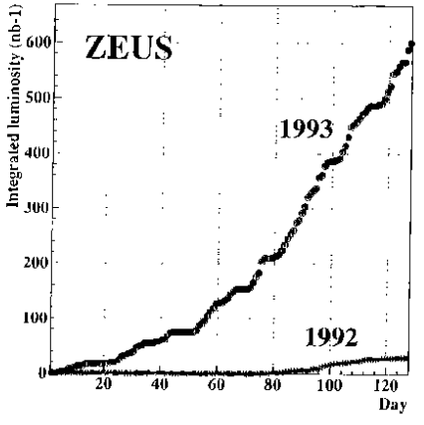

Fig. 2 Integrated luminosity collected by ZEUS during the 1992 and 1993 running periods as a function of time (from G. Iacobucci)

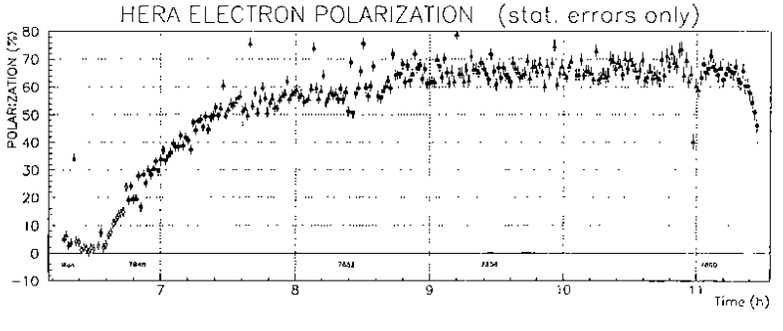

Fig. 3 Build-up of transverse electron polarization at E_e = 26.67 GeV versus time. A change of the machine tune made around 8:30 leads to an increase of the polarization.

3 THE EXPERIMENTS

3.1 Detector Challenges

HERA produces a large variety of reactions with widely differing energy flows. This feature together with the desire for detecting and identifying the constituents which participate in these reactions such as electron, neutrino, photon, quark and gluon places different requirements on the detector. The large momentum imbalance between incident electron and proton and the nature of space - like processes send most particles into a narrow cone around the proton direction. The observation of deep inelastic (DIS) neutral current (NC) scattering, e p -> e X (fig. 4a), is fairly straightforward. It produces a high energy electron whose transverse momentum is balanced by the current jet. The remnants from the breakup of the proton escape mostly unseen down the beam pipe. The variables x and Q^2 which describe the process (see below) can be determined from the energy and angle of either the electron or the current jet. This requires a precise electromagnetic and hadronic calorimeter with the calibration known at the 1 - 2% level.

In charged current (CC) scattering, e p -> ν X (fig. 4b), only the current jet can be detected. The identification of such events is based on the observation of missing transverse momentum carried away by the neutrino. It requires a hermetic calorimeter which covers the full solid angle such that e.g. photons, neutrons or K^0_L's cannot escape undetected. The variables x and Q^2 are measured from the current jet.

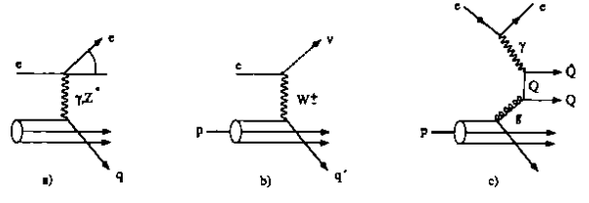

Fig. 4 Diagrams for NC and CC scattering and for photon - gluon fusion

The observation of processes at low Q^2 with scattering on soft partons (e.g. fig. 4c) is more difficult. The energy deposited in the calorimeter often is only a few GeV. Additional information from tracking detectors which surround the interaction point is necessary for their identification.

Background presents another challenge. The number of events from e - p interactions is tiny (10^{-3} - 10^{-5}) compared to the background events produced for instance by beam protons on the beam pipe wall or in the residual gas. What is worse, this type of background often deposits a large amount of energy in the detector. A typical background event is shown in fig. 5 where 225 GeV are observed in the calorimeter and many tracks in the tracking detector. At proton design current the background rate is expected to be around 10 - 100 kHz. The detector must be able to discriminate quickly - within a few microseconds - and deadtime free against background events although both beams cross each other every 96 ns. The high background rates combined with the short bunch crossing interval forced the HERA experiments to develop novel concepts of electronic readout and triggering, concepts which are suitable also for detectors at the next generation of pp colliders, such as the LHC.

The H1 and ZEUS detectors are driven by their choice of calorimeter. ZEUS uses a compensating uranium - scintillator calorimeter which provides the best possible energy resolution for hadrons. Compensation means that electromagnetic particles (electrons, photons) and hadrons of the same energy yield the same pulse height, e/h = 1. The radioactivity of the (depleted) uranium provides an extremely stable calibration signal, the mean life time of ^{238}U being 6.5 . 10^9 years. The H1 calorimeter uses liquid argon for readout which allows for a very stable and precise energy calibration and a high transverse and longitudinal segmentation. The calorimeter is noncompensating, e/h = 1.1 - 1.25. However, due to the high segmentation, using software weighting with the observed shower profile equal signals for electrons and hadrons can be obtained.

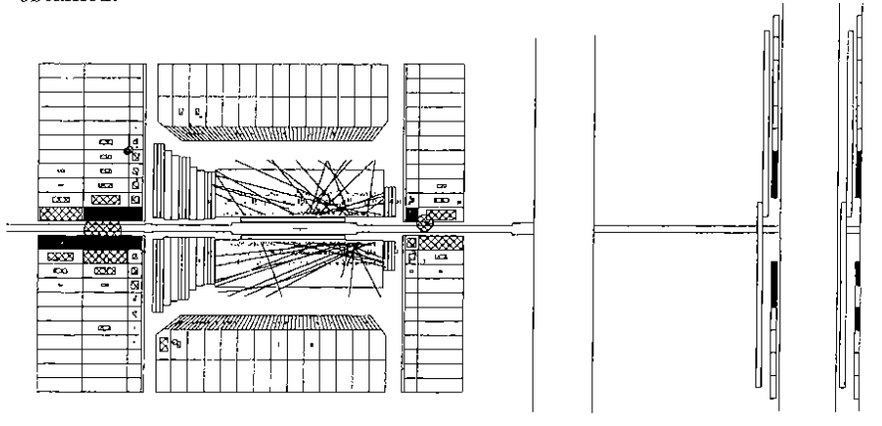

Fig. 5 A background event produced by a proton interaction upstream (to the right) of the ZEUS detector

3.2 The H1 Detector

The H1 detector (H1 1986, 1993d) is displayed in fig. 6. The proton beam enters from the right, the electron beam from the left.

Charged particles are tracked in a magnetic field of 1.2 T which is produced by a superconducting solenoid that surrounds the calorimeter. The effect of the magnetic field on the beams is compensated by a small solenoid (in fig. 6 located on the right side). The tracking system consists of two cylindrical jet - and z - drift chambers in the central region, and of three radial and three planar drift chambers in the forward direction. The drift chambers are interleaved with proportional wire chambers for a fast trigger selection. The backward direction is covered by a four layer proportional wire chamber providing space points up to a scattering angle of 175^0. In the forward direction a transition radiation detector (TRD) enhances the electron identification. The central drift chambers provide up to 56 space points with a resolution of 170 μm in rφ and 2.2 cm in z. The z-drift chambers measure the z-coordinate with an accuracy of 200 - 260 μm.

The liquid - argon calorimeter (LAC) covers the angular region $4^0 < \theta < 153^0$ (the forward direction, $\theta = 0^0$, is given by the direction of the proton beam). The calorimeter is longitudinally subdivided into an electromagnetic section with

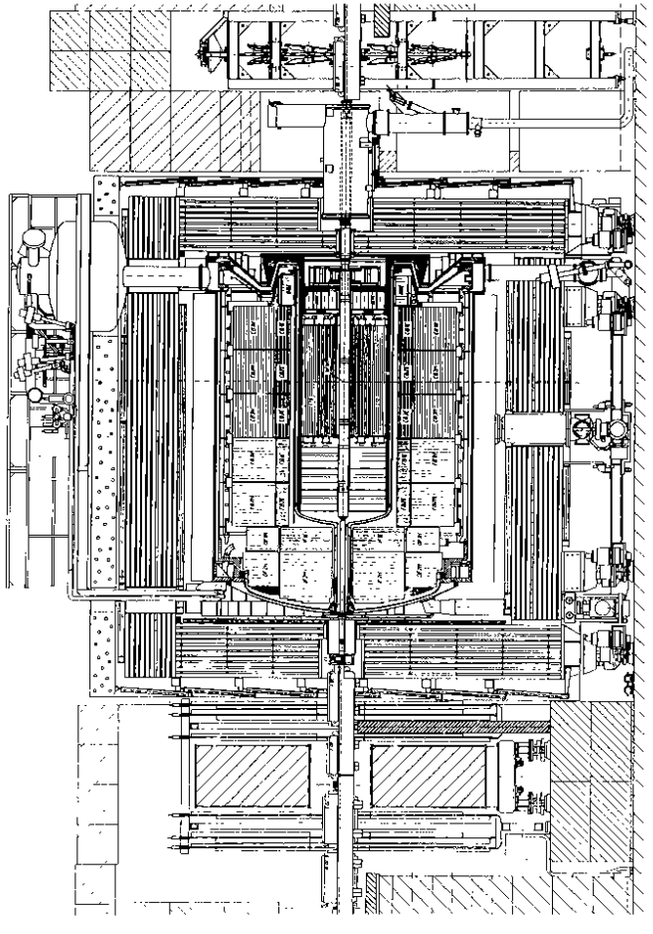

Fig. 6 Longitudinal cut through the H1 detector along the beam line

lead plates and a hadronic section with stainless steel plates as absorbers. The total depth varies between 8 and 4.5 absorption lengths. The calorimeter is finely segmented into a total of 45 000 channels. The calorimeter was optimized for a precise measurement and identification of electrons and for a stable energy calibration for electrons and hadrons. The energy resolution σ/E for electrons is $12\%/\sqrt{E} \oplus 1\%$ (E in GeV, $\oplus$ means quadratic addition) and $50\%/\sqrt{E} \oplus 2\%$ for hadrons (after weighting) as measured with test beams (figs. 7. 8). The calorimeter has been in operation since April 1991. With the same load of liquid argon the signal was found to decrease less than 0.5% per year.

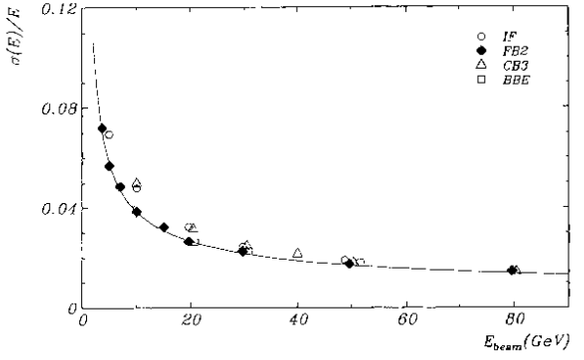

Fig. 7 Energy resolution of the H1 calorimeter for electrons for different parts of the calorimeter (H1 1993)

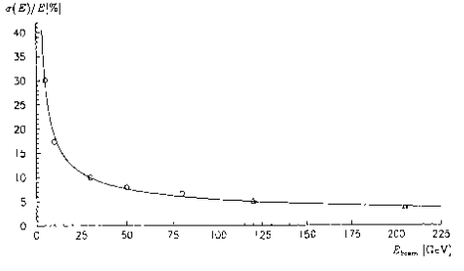

Fig. 8 Energy resolution of the H1 calorimeter for pions (H1 1993)

In the backward direction the LAC is supplemented by an electromagnetic lead - scintillator calorimeter (BEMC), covering $151^0 < \theta < 177^0$, followed by time-of-flight counters (TOF - VETO). In the forward direction the plug calorimeter with copper plates and silicon diode readout extends the energy measurement for hadrons down to angles of 0.7^0.

The magnet yoke is made of 10 layers of 7.5 cm thick iron plates. The gaps are instrumented with limited streamer tube (LST) chambers for measuring energy which has not been fully absorbed in the liquid argon calorimeter and for tracking of muons. Large area LST chambers in front and behind the iron yoke and an iron toroid magnet plus 6 layers of drift chambers in the forward direction complete the muon detection system.

The luminosity is measured by observing the bremsstrahlung process e p -> e'pγ at very small angles to the electron beam direction. The final state electron and photon are detected in coincidence in electromagnetic calorimeters of the luminosity detector LUMI positioned at 33 m (electron tagger ET) and 100 m (photon tagger PD) downstream of the central detector in the electron direction (fig. 9). At nominal luminosity the rate of luminosity events is between 50 - 100 kHz depending on the selection criteria.

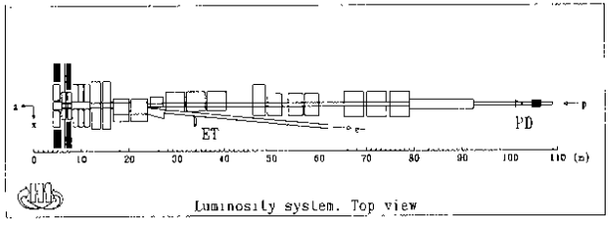

Fig. 9 Layout of the H1 luminosity detector

The H1 collaboration at present consists of about 390 physicists from 36 institutes and 12 countries.

3.3 The ZEUS detector

A view of the central part of the ZEUS detector (ZEUS 1986, 1993a) is shown in fig. 10. Charged particles are tracked by the inner tracking system, consisting of a vertex detector (VXD), a central tracking detector (CTD), planar drift chambers in the forward and rear directions (FTD, RTD). A transition radiation detector (TRD) helps with electron identification in the forward direction. The VXD consists of 12 layers of axial sense wires. The CTD has 9 superlayers (5 axial and 4 small angle stereo), each with 8 layers of sense wires. The three innermost axial layers (1, 3 and 5) are additionally instrumented with z-by-timing electronics mainly for triggering purposes. A thin (0.9 r.l.) superconducting solenoid surrounding the inner tracking system produces a magnetic field of 1.43 T. A compensator solenoid suppresses the effects on the beams.

A uranium - scintillator calorimeter (CAL) encloses the solenoid. It is subdivided mechanically into the forward (FCAL), barrel (BCAL) and rear (RCAL) calorimeters. The CAL covers polar angles θ from 2.6° to 176.1° and 99.7% of the total solid angle. In the HERA reference system the coverage in pseudorapidity $\eta = -\ln\tan(\theta/2)$ is as follows: FCAL: $4.3 > \eta > 1.1$, BCAL: $1.1 > \eta > -0.75$ and RCAL: $-0.75 > \eta > -3.8$. The calorimeter consists of a total of 80 modules. Every module is made of up to 185 layers of 3.3 mm thick depleted uranium plates plus 2.6 mm thick scintillator plates. Wavelength shifter bars transport the light to photomultipliers. The modules are subdivided longitudinally into an electromagnetic and two (one) hadronic sections in FCAL, BCAL (RCAL) representing a total depth of 7 to 4 absorption lengths. The scintillator plates form 5 x 20 cm^2 (10 x 20 cm^2) cells in the electromagnetic section and 20 x 20 cm^2 in the hadronic sections of FCAL, BCAL (RCAL). The total number of cells is 5918.

The calibration of the photomultipliers is monitored with the signal from the radioactivity of the uranium (UNO) to a precision of < 0.2%. The pulse

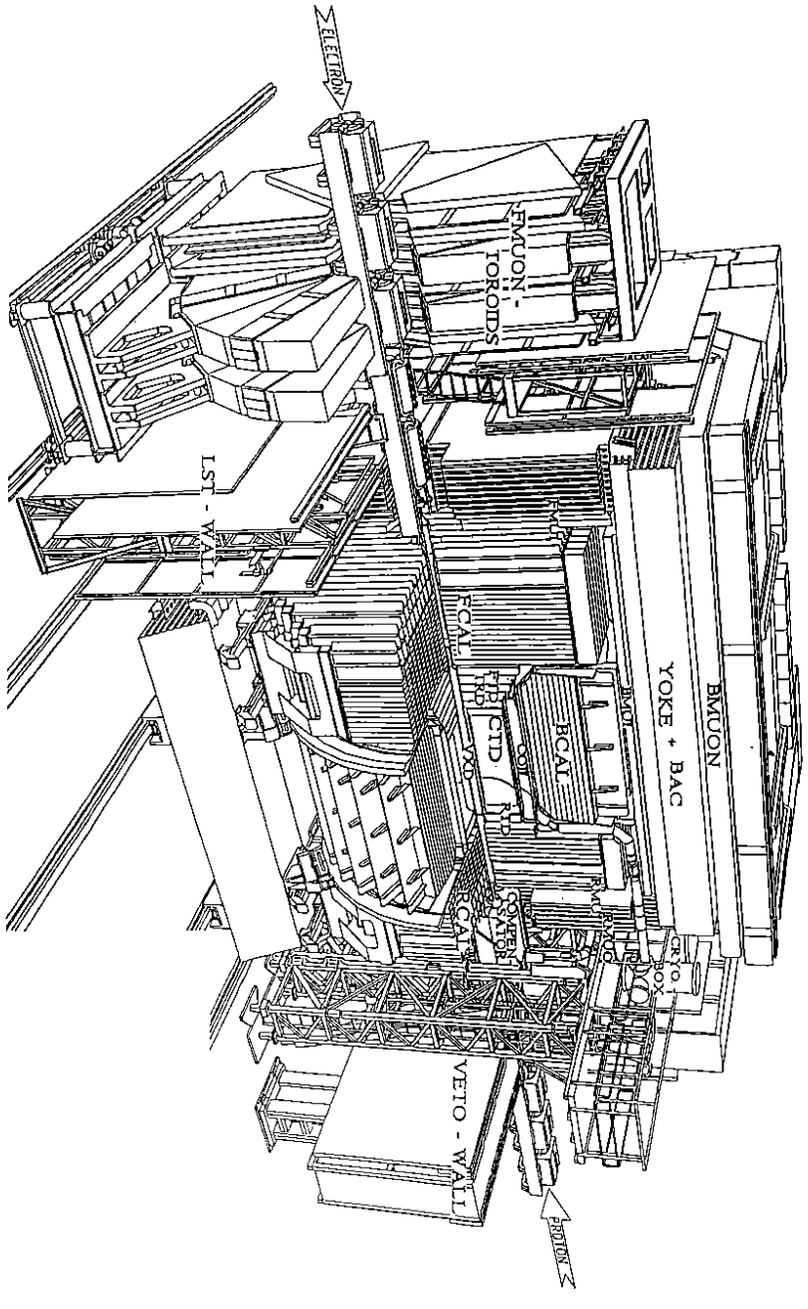

Fig. 10 Schematic view of the central part of the ZEUS detector

heights of electrons and hadrons (fig. 11a) are equal to within 3%, i.e. e/h = 1.0 ± 0.03 (fig. 11b), for momenta above 3 GeV/c. The energy resolution as measured in the test beam is for electrons $\sigma/E = 18\%/\sqrt{E}$ (E in GeV) and for hadrons $35\%/\sqrt{E}$ (fig. 11c). The calorimeter noise, which is dominated by the uranium radioactivity, is typically 15 MeV in the EMC cells and 25 MeV in the HAC cells. The calorimeter also yields an accurate time measurement. The time resolution of a calorimeter cell is $\sigma = 1.5/\sqrt{E} \oplus 0.5$ ns or < 1 ns above 3 GeV.

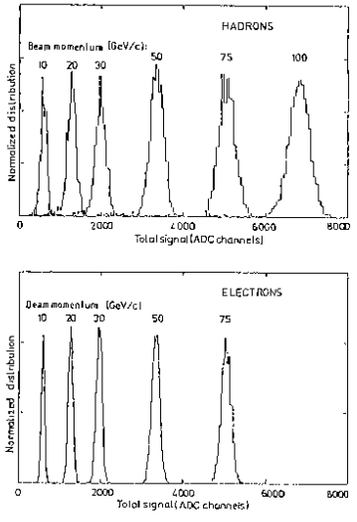

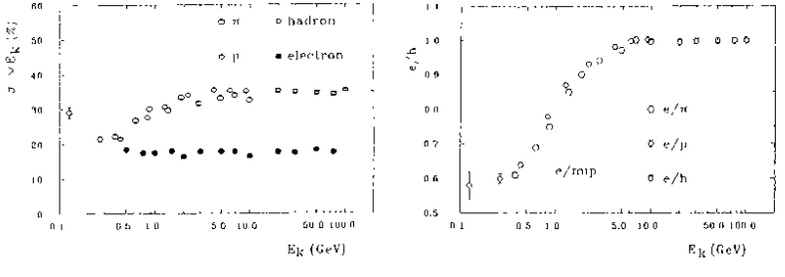

Fig. 11 Measurements with the ZEUS prototype calorimeter
(a) Pulse height distributions for electrons and hadrons
(b) Energy resolution for electrons and hadrons
(c) e/h ratio as a function of particle momentum

In the course of an upgrade program, the transverse segmentation of the rear and forward parts of the calorimeter is being increased by inserting a plane of 3 x 3 cm^2 silicon diodes after the first 3 radiation lengths.

A small tungsten - silicon calorimeter (BPC) positioned at the beam pipe behind RCAL tags electrons scattered with Q^2 up to 0.5 GeV^2.

The iron yoke serves as the absorber for the backing calorimeter and as a muon filter. It is made of 7.5 cm thick iron plates and is instrumented with proportional tube chambers for measuring the energy not absorbed in the uranium calorimeter. For identification and momentum measurement of muons the yoke is magnetized to 1.6 T with copper coils. Large area LST chambers measure the position and direction of muons in front and behind the iron yoke (BMUON, RMUON). In the forward direction a spectrometer of two iron toroids and drift - and LST chambers (FMUON) identifies muons and measures their momenta up to 100 - 150 GeV/c.

For luminosity measurement the same reaction and a setup similar to that of H1 is used (fig. 12a).

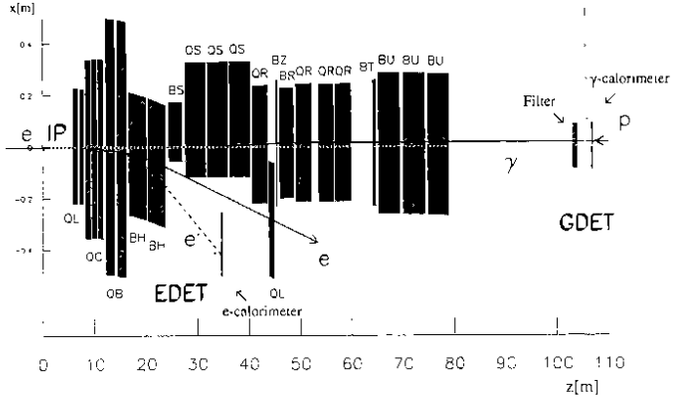

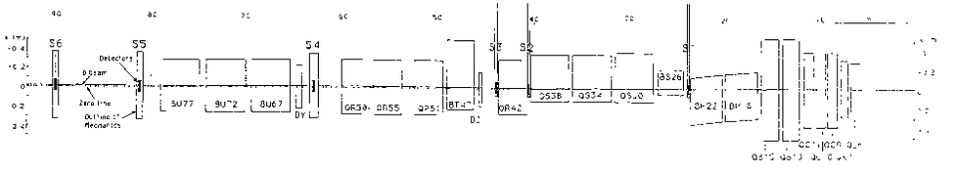

Fig.12 (a) The ZEUS luminosity detector: shown are the detectors for photons (GDET) and the scattered electron (EDET) together with the beam elements
(b) Layout of the leading proton spectrometer of ZEUS

Very forward scattered protons (transverse momenta < 1 GeV/c) are measured in the leading proton spectrometer (LPS) which uses the proton ring magnets for momentum analysis and detects the scattered protons in 6 stations with silicon strip detectors mounted very close to the beam at distances between 26 and 96 m from the interaction point (fig. 12b). First data were taken in 1993 with the stations S4 - S6.

In 1993 a prototype hadron calorimeter (FNC) was installed behind S6 for detecting very forward produced neutrons.

Particles produced by the proton beam upstream of the detector are detected in the VETOWALL. For monitoring the time structure and other properties of the two beams a ring counter C5 has proven to be invaluable. It is made of two lead - scintillator layers and mounted on the beam pipe behind RCAL. C5 registers the halo particles accompanying both beams.

The ZEUS collaboration consists of about 460 physicists from 12 countries and 50 institutes.

3.3 Trigger Selection

The selection of interesting events during data acquisition proceeds in four (three) trigger steps for H1 (ZEUS). The selection at trigger level one is made after 2.4μs (H1) and 4.4 μs (ZEUS), respectively. Up to this point information from 200 000 to 300 000 electronic channels are stored dead time free in analog or digital pipelines for 25 (H1) and 46 (ZEUS) consecutive beam crossings, respectively. Global information from various components like the calorimeter energy sums obtained by summing over specific regions of the calorimeter are processed in trigger pipelines. In case an interesting event is detected, the signal pipelines are stopped and the data for the bunch crossing(s) in question are digitized. The digitized data are used at the next trigger level(s) for a more restrictive event selection.

The final event selection is done in computer farms. At this point the completely digitized information for the event is available and a first reconstruction of the event is performed. The filter farms consist of a large number of fast processors with computing power of about 1000 MIPS (million instructions/s), each processor processing one event at a time. The rate of accepted events varies in both experiments between about 3 and 7 Hz; typical event sizes are 60 kByte (H1) to 140 kByte (ZEUS). The accepted events are reconstructed off-line in processor farms with sufficient computing power to have the reconstructed events available for analysis within a few hours after data taking.

4 RUNNING CONDITIONS

The typical bunch configuration of HERA is sketched in fig.13: consecutive proton bunches and electron bunches are filled which collide with each other. In addition there are unpaired proton bunches which have no electron partner, and vice versa. The unpaired bunches are used for the study of beam induced background and the determination of the luminosity.

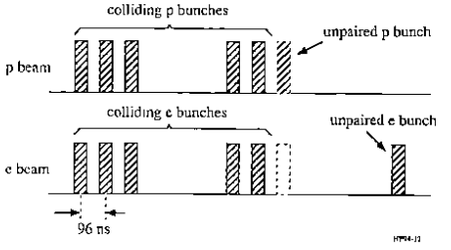

Fig. 13 Sketch of the HERA bunch configuration

The luminosity was measured by detecting the process ep -> e'p γ as mentioned before. Figure 14 shows the scatter plot of the energies E_e', E_γ for the final state electron and photon as determined by the luminosity detector. There is a well isolated band of events for which the sum of the two energies is equal to the energy of the electron beam, $E_e' + E_\gamma = E_e$, as expected for the luminosity reaction. However, bremsstrahlung of the electron beam on the residual gas in the beam pipe, e A -> e' A' γ, satisfies the same condition. The subtraction of this background was done by measuring the gas bremsstrahlung with the unpaired electron bunch and scaling with the currents of the unpaired electron bunch and of the total electron beam (see fig. 15). The achieved precision of the luminosity measurement is at present about 5 %.

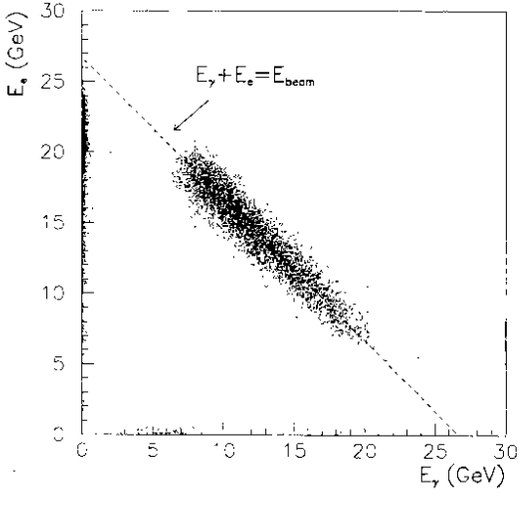

Fig. 14 Scatter plot of the electron energy versus the photon energy measured in the ZEUS luminosity detector

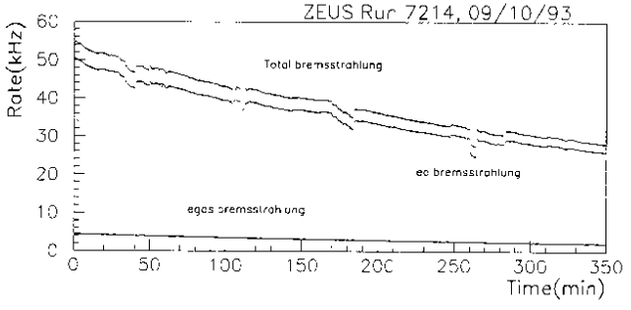

Fig. 15 The total bremsstrahlung rate (upper curve) and the luminosity after subtraction of beam gas bremsstrahlung (lower curve) as a function of time (from ZEUS)

The high background in combination with the 96 ns bunch spacing makes triggering at HERA a challenging task. The major source of background, proton interactions with the residual gas and the beampipe, called beam gas (see fig. 5), must be eliminated without losing efficiency for deep inelastic ep scattering and possible new physics processes of very low cross section. Not all of the large photoproduction cross section can be recorded, so the trigger acceptance is reduced for the standard processes and is maximized for specific sub-processes such as hard scattering and heavy quark production.

The strategies for suppressing unwanted background and selecting electron - proton collisions were different for the two experiments.

4.1 ZEUS Data Taking

In the ZEUS experiment, the trigger selection was made on the basis of the total transverse energy E_T and missing E_T measured by the calorimeter, veto signals from the vetowall or the C5 counter, electron tagging by the luminosity detector and combinations of tracking and calorimeter information at the first and second trigger levels, making tight timing cuts with the calorimeter at the second and third levels and running many physics filters at the third level.

The calorimeter time information has turned out to be a powerful handle for rejecting proton beam background. This is illustrated in fig. 16. In an ep collision particles are emitted from the interaction point, IP, and arrive at the calorimeter cells of RCAL and FCAL at equal times t = 0 while a proton interaction upstream of the detector such as shown in fig. 5 deposits energy in the RCAL about 10 ns earlier. The 10 ns difference corresponds to twice the distance between RCAL and the IP. Of course, in FCAL also the proton induced background arrives at t = 0. The measured distribution of FCAL (t_F) versus RCAL (t_R) times is shown in fig. 16 for events with more than 1 GeV deposited in a calorimeter cell in both FCAL and RCAL. The ep events with $t_F \approx t_R \approx 0$ are well separated from the background which clusters around $t_R = -10$ ns, $t_F - t_R = 10$ ns. Note, there are about 1000 times more background than ep events.

Samples of event pictures are shown in fig. 17. The first event stems from neutral current scattering at $Q^2 \approx 5300$ GeV^2, $x \approx 0.11$, with an electron seen in BCAL and a high energy jet in FCAL (fig. 17a). The jet near the proton beam is presumably produced by the proton remnants. The high energy jet and the electron are back-to-back in the transverse plane and balance transverse momentum as expected for an NC event. The interaction point is marked by tracks detected in the cylindrical drift chamber (CTD). The second event (fig. 17b) shows a low Q^2, low x event ($Q^2 \approx 48$ GeV^2, $x \approx 0.003$. The electron is produced very close to the beam and is only seen in RCAL. The third event (fig. 17c) is due to NC scattering ($Q^2 \approx 53$ GeV^2) and shows a large rapidity gap between the proton direction and the first particle observed in the detector.

The event pictures were produced by including every calorimeter cell with an energy more than 60 (100) MeV in the electromagnetic (hadronic) section. The calorimeter is seen to be very clean of noise and background.

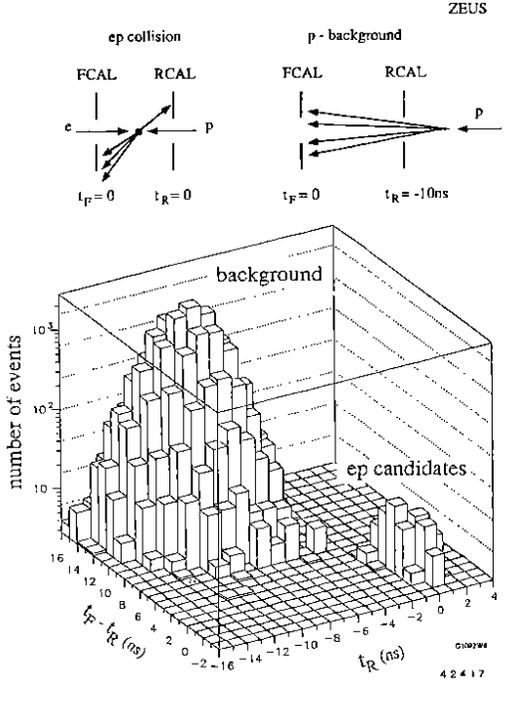

Fig. 16 Distribution of the signal time measured by ZEUS in the RCAL (t_R) versus the difference $t_F - t_R$ between signal times seen in FCAL and RCAL

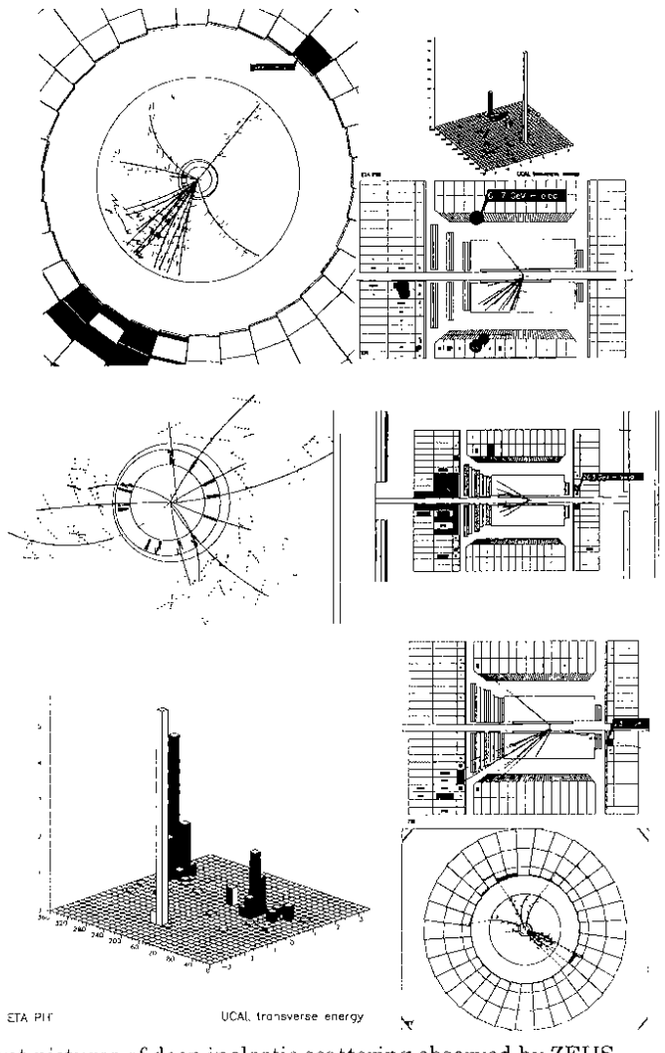

Fig. 17 Event pictures of deep inelastic scattering observed by ZEUS
Top: at $Q^2 \approx 5300$ GeV^2, $x \approx 0.11$; the scattered electron is opposite a jet of particles
Middle: at $Q^2 \approx 48$ GeV^2, $x \approx 0.003$; on the left a blow-up of the vertex and CTD region. The stereo hits (layers 2, 4, 6, 8) are plotted assuming $\theta = 90^0$
Bottom: at $Q^2 \approx 53$ GeV^2, $x \approx 0.004$ for an event with a large rapidity gap and two jets

4.2 H1 Data Taking

Events were accepted by H1 at the trigger stage using the information on E_T and missing E_T measured in the calorimeter, on electron tagging by the luminosity detector and on charged particles recorded by the tracking detectors. Background was rejected primarily with the time measurement provided by the time-of-flight counters and the z-coordinate of the event vertex determined by the proportional wire chambers.

A spectacular event produced by a proton interaction on the residual gas in the beam pipe is shown in fig. 18. It has 21 protons identified via dE/dx in the central jet chamber. The dE/dx distribution for background events shows well isolated bands of π, K, p and d (fig. 19).

The overall response of the detector is illustrated in fig. 20 with events from NC scattering and photoproduction. The high longitudinal and transverse segmentation of the liquid argon calorimeter gives a detailed account of the energy deposition for single particles and jets.

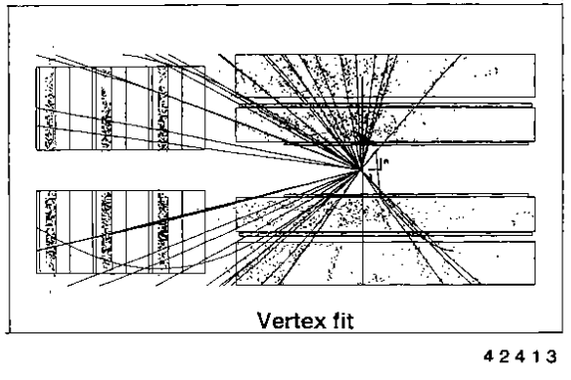

Fig. 18 Example of a proton-gas interaction in the H1 detector with 21 final state protons identified by dE/dx

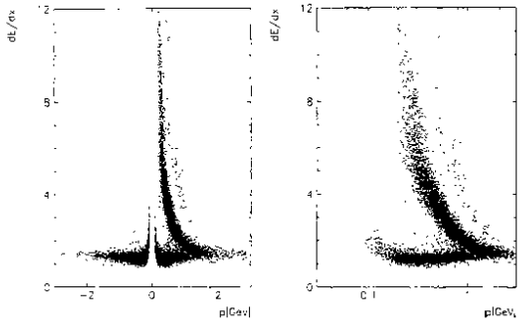

Fig. 19 Specific ionization loss dE/dx versus momentum p as observed by the central detector of H1 for negative ($p < 0$) and positive particles ($p > 0$)

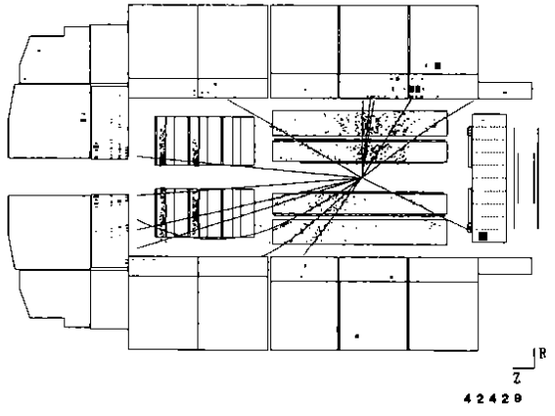

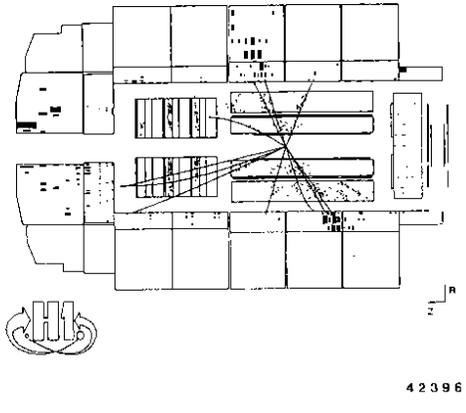

Fig. 20 Event pictures observed by H1
(a) Deep inelastic NC scattering at $Q^2 = 103\ GeV^2$, $x = 0.004$
(b) Photoproduction with two jets in the final state

5 Introduction to deep inelastic lepton nucleon scattering

In deep inelastic scattering the incoming electron couples to the electroweak current J which probes the structure of the proton. The neutral (NC) and charged (CC) components of the current can be distinguished by the final state electron or neutrino. The basic deep inelastic scattering process (DIS) is illustrated in fig. 21. For Q^2 much larger than the mass squared of the proton the proton can be thought of as a group of quasifree constituents - quarks, gluons... - one of which interacts with the current while the rest of the group (= proton remnant) moves on unperturbed.

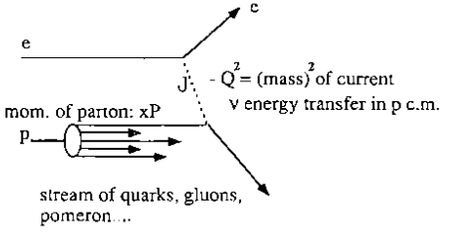

Fig. 21 Diagram for ep scattering

5.1 Kinematics

The large imbalance between electron and proton beam momenta makes the kinematics at HERA quite different from that of other colliders where both beams have equal momenta or from fixed target experiments where the nucleon is stationary. Since a good grasp of the kinematical situation is useful for an understanding of the underlying processes, it will be discussed in some detail for DIS.

The relevant kinematic variables are

E_e, E_p		electron and proton beam energies
$e = (0, 0, -E_e, E_e)$	$p = (0, 0, E_p, E_p)$	four momenta of incoming e, p
$e' = (E_e' \sin\theta_e', 0, E_e' \cos\theta_e', E_e')$		four momentum of scattered e'
$s = (e+p)^2 = 4 E_e E_p$		square of total c.m. energy
$q^2 = (e-e')^2 = -2 E_e E_e' (1+\cos\theta_e') = -Q^2$		square of four momentum transfer
$Q^2_{max} = s$		maximum possible Q^2 value
$\nu = q \cdot p / m_p$		energy of current J in p rest system
$\nu_{max} = s / (2 m_p)$		maximum energy transfer
$y = (q \cdot p)/(e \cdot p) = \nu / \nu_{max}$		fraction of energy transfer
$x = Q^2/(2 q \cdot p) = Q^2/(2 m_p \nu) = Q^2/(y s)$		Bjorken scaling variable
$W^2 = (p+q)^2 = m_p^2 - Q^2 + 2 m_p \nu$		mass squared of the total hadronic
$= m_p^2 + Q^2 (1/x - 1)$		system produced
$\Delta = \hbar / Q$		smallest object size that can be resolved in proton

where E_e' and θ_e' are the energy and angle (w.r.t. the incoming proton) of the scattered lepton and where the electron and proton masses, m_e, m_p, have been neglected.

For fixed c.m. energy, inclusive scattering, ep -> eX, is described by two variables for which e.g. x and Q^2 can be chosen. The same variables describe the lowest order process where the electron scatters elastically on a free constituent of the proton (fig. 21). For NC events these variables can be determined either from the energy and angle of the scattered electron, or of the final state hadron system, or from a mixture of both. For CC events, only the hadron system is accessible for measurement.

The electron side yields:

$$\begin{aligned} y &= 1 - (E_e'/2E_e)(1 - \cos\theta_e') \\ Q^2 &= 2E_e E_e'(1 + \cos\theta_e') \\ x &= E_e'(1 + \cos\theta_e')/(2yE_p) \end{aligned} \qquad (5.1)$$

and the inverse relations

$$\begin{aligned} E_e' &= (1 - y)E_e + xyE_p \\ \cos\theta_e' &= [xyE_p - (1 - y)E_e]/[xyE_p + (1 - y)E_e] \\ E_e'^2 \sin^2\theta_e' &= 4xy(1 - y)E_e E_p \end{aligned} \qquad (5.2)$$

From the hadron system j (excluding the proton remnant) with energy E_j and production angle θ_j one finds:

$$\begin{aligned} y &= (E_j/2E_e)(1 - \cos\theta_j) \\ Q^2 &= E_j^2 \sin^2\theta_j/(1 - y) \\ x &= E_j(1 + \cos\theta_j)/[(1 - y)(2E_p)] \end{aligned} \qquad (5.3)$$

and

$$\begin{aligned} E_j &= yE_e + x(1 - y)E_p \\ \cos\theta_j &= [-yE_e + (1 - y)xE_p]/[yE_e + (1 - y)xE_p] \\ E_j^2 \sin^2\theta_j &= 4xy(1 - y)E_e E_p = Q^2(1 - y) \end{aligned} \qquad (5.4)$$

Using the method of Jacquet - Blondel (1979) the hadron variables can be determined approximately by summing the energies (E_h) and transverse (p_{Th}) and longitudinal momenta (p_{zh}) of all final states. The method rests on the assumption that the total transverse momentum carried by those hadrons which escape detection through the beam hole in the proton direction as well as the energy carried by particles escaping through the beam hole in the electron direction can be neglected. The result is:

$$\begin{aligned} y_{JB} &= \Sigma_h (E_h - p_{zh})/(2E_e) \\ Q_{JB}^2 &= [(\Sigma_h p_{xh})^2 + (\Sigma_h p_{yh})^2]/[1 - y_{JB}] \\ x_{JB} &= Q_{JB}^2/(y_{JB} s) \end{aligned} \qquad (5.5)$$

The mixed or double-angle method (Bentvelsen et al., 1991) uses the electron scattering angle and the angle γ_h which characterizes the longitudinal and transverse momentum flow of the hadronic system (in the naive parton model

γ_h is the scattering angle of the struck quark):

$$\cos\gamma_h = \frac{(\Sigma_h p_{xh})^2 + (\Sigma_h p_{yh})^2 - (\Sigma_h (E_h - p_{zh}))^2}{(\Sigma_h p_{xh})^2 + (\Sigma_h p_{yh})^2 + (\Sigma_h (E_h - p_{zh}))^2}$$

$$\begin{aligned} Q_{DA}^2 &= 4E_e^2 \sin\gamma_h (1 + \cos\theta_e')/[\sin\gamma_h + \sin\theta_e' - \sin(\gamma_h + \theta_e')] \\ x_{DA} &= (E_e/E_p)[\sin\gamma_h + \sin\theta_e' + \sin(\gamma_h + \theta_e')]/[\sin\gamma_h + \sin\theta_e' - \sin(\gamma_h + \theta_e')] \\ y_{DA} &= Q_{DA}^2/(x_{DA} s) \end{aligned} \qquad (5.6)$$

As the double - angle method relies on ratios of energies it is less sensitive to a scale uncertainty in the energy measurement of the final state particles.

For NC events the precision of x and Q^2 can be improved by a simultaneous fit to all measured variables (Chaves et al. 1991).

The Bjorken variable x, defined above from the electron side, for the lowest order process (fig 22 a) is equal to the fraction η of the proton momentum carried by the struck quark. This can be seen as follows:

ηp		incident momentum of struck quark
$j = \eta p + q$		outgoing momentum of struck quark (system) (5.7)
$j^2 = \eta^2 p^2 + 2\eta p \cdot q - Q^2$		mass squared of the outgoing struck quark (system)

If the mass of the outgoing quark is zero, $M_j^2 \equiv j^2 = 0$ and for $Q^2 \gg \eta^2 p^2 = \eta^2 m_p^2$:

$$Q^2 \approx 2\eta p \cdot q \qquad (5.8)$$

and therefore $\eta = x$.

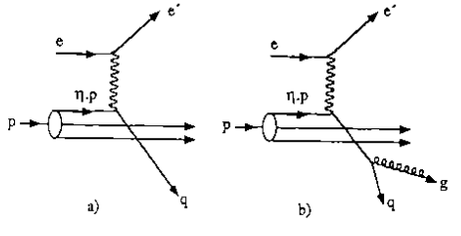

Fig. 22 Diagrams for (a) DIS in lowest order and (b) with gluon bremsstrahlung

If the mass of the outgoing struck quark is not equal to zero, for instance due to gluon radiation (e.g. fig. 22 b), then

$$\eta = x + M_J^2 / 2 (q \cdot p) = x + M_J^2 / (2 m_p \nu). \quad (5.9)$$

In this case $\eta > x$. In order to produce a *massive* hadronic system for the same energy transfer ν from the electron side, the struck quark must carry a larger fraction of the proton momentum. As a consequence, in the massive case the hadronic energy flow moves closer to the direction of the incident proton than given by the angle γ_h calculated for the massless case.

5.2 Kinematic regime of HERA

Table 2 compares the kinematic ranges accessible at HERA and in previous lepton - nucleon scattering experiments.

Table 2 Kinematic regions accessible at HERA (E_e = 30 GeV, E_p = 820 GeV) and in previous experiments

	HERA	pre - HERA
s (GeV^2)	10^5	10^3
maximum practical Q^2 (GeV^2)	40 000	400
Δ (cm^{-1})	$1 . 10^{-16}$	$1 . 10^{-15}$
ν_{max} (GeV)	52 000	500
minimum x at Q^2 = 10 GeV^2	$1 . 10^{-4}$	$1 . 10^{-2}$

The maximum energy transfer is increased by a factor of ~ 100: HERA is equivalent to a fixed target experiment with an incident electron beam of 52 TeV. The Q^2 domain over which lepton nucleon scattering can be measured is also increased by two orders of magnitude. Since the typical Q^2 values in DIS are much larger than the proton mass the electron interacts with one of the partons (quarks, gluons, ..) rather than with the proton as a whole: HERA is in reality an electron - parton collider.

The correlations between energy and angle of electron and current jet (ignoring gluon emission) are shown in fig. 23 in the x - Q^2 plane. For the purpose of orientation fig. 24 shows in the x - Q^2 plane lines of constant y and W and the kinematic region covered by non-HERA experiments.

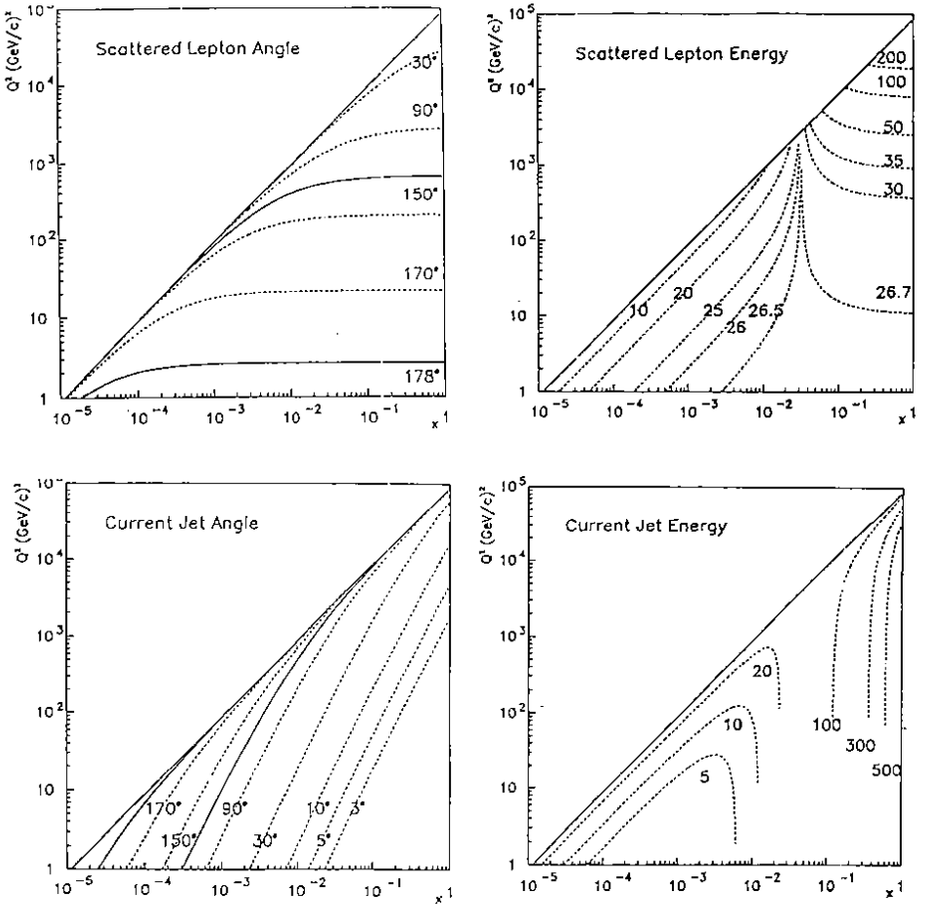

Fig. 23 The x - Q^2 dependence of the angle and energy of the scattered electron and the current jet (ignoring gluon radiation) for beam energies of E_e x E_p = 26.7 GeV x 820 GeV. The angles are measured w.r.t. the proton direction.

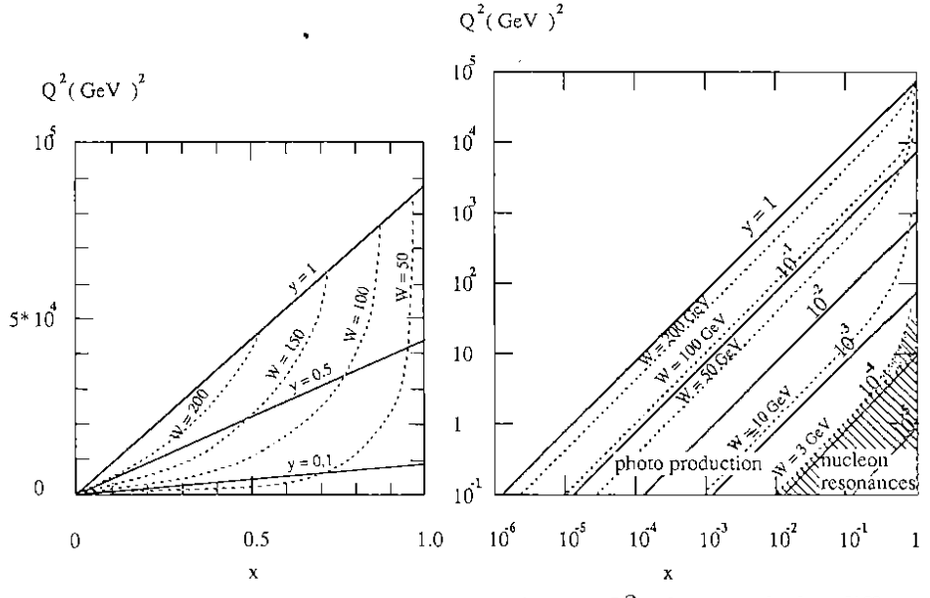

Fig. 24 Lines of constant y in the x - Q^2 plane and the different kinematical regimes as a function x

5.3 Cross sections for DIS

The cross sections for NC and CC scattering are related to the structure functions F_i of the proton (see e.g. Ingelman and Rückl 1988, PDG 1992):

NC, e p -> e X:

$$\frac{d^2\sigma(\gamma+Z^0)}{dx\,dy} = \frac{4\pi\alpha^2}{s\,x^2\,y^2}\,[(1 - y + y^2/2)\,F_2(x,Q^2) - y^2/2\,F_L(x,Q^2) \pm (y - y^2/2)\,xF_3(x,Q^2)] \qquad (5.10)$$

The upper (lower) sign applies to e^- (e+) p scattering. The longitudinal structure function is related to F_1, F_2 via

$$F_L(x,Q^2) = F_2(x,Q^2) - 2\,xF_1(x,Q^2) = 2\,x\,F_1(x,Q^2)\,R(x,Q^2)$$

with

$$R(x,Q^2) = F_L(x,Q^2)/[2\,xF_1(x,Q^2)] = [F_2(x,Q^2)/2\,xF_1(x,Q^2)] - 1 \qquad (5.11)$$

For $Q^2 \gg 1$ GeV^2 and not too small x the contribution of the longitudinal structure function F_L is small. The F_3 term measures parity violating contributions which arise from Z^0 exchange. It is significant only when Q is comparable to or larger than the Z^0 mass.

For some applications it is useful to express the photon part of the DIS cross section in terms of the total cross sections σ_T, σ_L for the scattering of transverse and longitudinal photons, respectively, on the proton. Neglecting contributions from Z^0 exchange:

$$2\,x\,F_1(x,Q^2) = Q^2/(4\pi^2\alpha)\,[1 - x]\;\sigma_T(x,Q^2)$$

$$F_2(x,Q^2) = Q^2/(4\pi^2\alpha)\,[1 - x]\;[\sigma_T(x,Q^2) + \sigma_L(x,Q^2)] \qquad (5.12)$$

Here, the assumption $4\,m_p^2x^2 \ll Q^2$ was made. A convenient expression for $x \ll 1$ is $\sigma_T(x,Q^2) \approx 112\ \mu b/Q^2 \cdot [2\,x\,F_1(x,Q^2)]$, Q^2 in GeV^2.

CC, e p -> ν X:

$$\frac{d^2\sigma(W)}{dx\,dy} = \frac{G_F^2\,s}{2\pi}\,\frac{1}{(1 + Q^2/M_W^2)^2}\,[(1 - y)\,F_2(x,Q^2) + y^2x\,F_1(x,Q^2) \pm (y - y^2/2)\,xF_3(x,Q^2)] \qquad (5.13)$$

where G_F is the Fermi coupling constant, $G_F = 1.02 \cdot 10^{-5}/m_p^2$. As before, the upper (lower) sign applies to e^- (e^+) p scattering. For scattering on pointlike spin-1/2 constituents by vector exchange $F_2(x,Q^2) = 2\,x\,F_1(x,Q^2)$ (Callan-Gross 1969).

The expressions for the NC and CC cross sections have very similar structures. This is particularly evident when G_F is expressed in terms of the electroweak coupling,

$$G_F = \pi\alpha/(\sqrt{2}\sin^2\theta_W M_W^2) \qquad (5.14)$$

where θ_W is the electroweak angle, $\sin^2\theta_W = 0.23$. The result is

$$\frac{d^2\sigma(W)}{dx\,dy} = \frac{\pi\alpha^2}{4\sin^4\theta_W\,sx^2y^2}\,\frac{Q^4}{(Q^2+M_W^2)^2}\,[(1 - y)\,F_2(x,Q^2) + y^2\,x\,F_1(x,Q^2) \pm (y^2/2 - y)\,xF_3(x,Q^2)] \qquad (5.15)$$

The main difference between the NC cross section from photon exchange and the CC cross section from W exchange is due to the different propagator terms,

$$d^2\sigma(W)\ /\ d^2\sigma(\gamma) \approx [Q^2/(Q^2 + M_W^2)]^2 \qquad (5.16)$$

The r.h.s. gives $2.4 \cdot 10^{-8}$, $2.4 \cdot 10^{-6}$, 0.02 and 0.4 at Q^2 = 1, 10, 1000 and 10^4 GeV^2. It is the heavy W mass which is responsible for the "weak" CC cross section at small Q^2 values.

5.4 DIS cross sections in the quark-parton model

The structure functions F_i from NC and CC scattering are in principle independent. They can be related via the quark - parton model (QPM), however. The underlying process of the lowest order diagram depicted by fig. 22a is elastic electron - quark scattering, e q -> e q. Photon exchange leads to the following cross section for this process:

$$\frac{d\sigma\,(eq \to eq)}{dQ^2} = \frac{4\pi\alpha^2 e_q^2}{Q^4}\,[\,1 - Q^2/s_{eq} + Q^4/(2\,s_{eq}^2)] \qquad (5.17)$$

where s_{eq} is the square of the (eq) c.m. energy, e_q is the electric charge of the quark and the assumption $s \gg m_e^2, m_q^2$ is made. Defining q(x) dx as the probability to find in the proton a quark of type q carrying a momentum fraction between x and x+dx, the resulting cross section for electron proton scattering via quark q is

$$\frac{d\sigma^q\,(ep \to eX)}{dx\,dQ^2} = \frac{4\pi\alpha^2}{Q^4}\,[\,1 - Q^2/s_{eq} + Q^4/(2\,s_{eq}^2)]\,e_q^2\,q(x). \qquad (5.18)$$

By noting that $s_{eq} = x\,s$ and $Q^2 = x\,y\,s$ this can be rewritten as follows:

$$\frac{d\sigma^q\,(ep \to eX)}{dx\,dy} = \frac{4\pi\alpha^2}{x^2 y^2 s}\,[\,1 - y + y^2/2]\,e_q^2\,x\,q(x). \qquad (5.19)$$

The total ep cross section is obtained by summing over all quark contributions:

$$\frac{d\sigma\,(ep \to eX)}{dx\,dy} = \frac{4\pi\alpha^2}{x^2 y^2 s}\,[\,1 - y + y^2/2]\,\Sigma_q\,e_q^2\,x\,q(x). \qquad (5.20)$$

This is the QPM prediction. The comparison with eq. (5.10) leads to the QPM expression for the structure function F_2 for the case of photon exchange:

$$F_2^{ep\to eX}(x) = \Sigma_q\,e_q^2\,x\,q(x) = x\,[4/9\,u(x) + 4/9\,\bar{u}(x) + 1/9\,d(x) + 1/9\,\bar{d}(x) + ..] \qquad (5.21)$$

Since only pointlike spin-1/2 constituents contribute, $2xF_1(x) = F_2(x)$ and $F_L(x,Q^2) = 0$. Inclusion of Z^0 exchange leads to the following expressions (see e.g. Ingelman and Rückl 1987):

$$F_2^{ep\to eX}(x) = \Sigma_q\,A_q(Q^2)\,x\,[\,q(x) + \bar{q}(x)]$$

$$xF_3^{ep\to eX}(x) = \Sigma_q\,B_q(Q^2)\,x\,[\,q(x) - \bar{q}(x)] \qquad (5.22)$$

where $A_q(Q^2) = e_q^2 - 2\,e_q v_e v_q\,[Q^2/(Q^2 + M_Z^2)] + (v_e^2 + a_e^2)(v_q^2 + a_q^2)\,[Q^2/(Q^2 + M_Z^2)]^2$

$B_q(Q^2) = -2\,e_q a_e a_q\,[Q^2/(Q^2 + M_Z^2)] + 4\,v_e v_q a_e a_q\,[Q^2/(Q^2 + M_Z^2)]^2$

The corresponding QPM expressions for the CC case are (see Rückl 1987):

$$F_2^{ep\to\nu X}(x) = x\Sigma_{i,j}\{\,|V_{u_i d_j}|^2\,u_i(x) + |V_{u_j d_i}|^2\,\bar{d}_i(x)\}$$
$$x\,F_3^{ep\to\nu X}(x) = x\Sigma_{i,j}\{\,|V_{u_i d_j}|^2\,u_i(x) - |V_{u_j d_i}|^2\,\bar{d}_i(x)\} \qquad (5.23)$$

where $V_{u_i d_j}$ are the elements of the CKM matrix, u_i and d_j denote up-type and down-type flavors, respectively, and i, j are family indices. At energies well above flavor thresholds eqs. (5.23) simplify to

$$F_2^{ep\to\nu X}(x) = x\,[u(x) + c(x) + \bar{d}(x) + \bar{s}(x) + ..]$$
$$x\,F_3^{ep\to\nu X}(x) = x\,[u(x) + c(x) - \bar{d}(x) - \bar{s}(x) + ..]. \qquad (5.24)$$

In QCD, the parton densities become Q^2 dependent, $u(x) \to u(x, Q^2)$, due to gluon radiation or photon-gluon interactions via an intermediate quark. Structure function measurements at a given value of Q^2 can be extrapolated to other Q^2 values by QCD evolution with the help of the GLDAP formalism (Gribov and Lipatov 1972, Lipatov 1974, Dokshitzer 1977, Altarelli and Parisi 1977). In the derivation of the evolution equations ln (1/x) terms are neglected over ln Q^2 terms. While this is justified for the range $x > 10^{-2}$ covered by fixed target experiments it may not be so for x values as small as 10^{-4} accesible at HERA. This approximation is avoided in the BFKL equations (Lipatov 1976, Kuraev, Lipatov and Fadin 1977, Balitskii and Lipatov 1978).

5.4 Guessing the parton distributions of the proton

It is instructive to estimate the general behavior of the parton distributions with a toy model. We shall do this for the proton.

Step A: The proton consists of valence quarks only, p = uud. Flavor conservation requires:

$$\int_0^1 u(x)\,dx = 2 \qquad \int_0^1 d(x)\,dx = 1. \qquad (5.25)$$

The u and d quarks carry the momentum of the proton which implies

$$x_{u_1} + x_{u_2} + x_d = 1 \qquad (5.26)$$

$$\int_0^1 x\,u(x)\,dx + \int_0^1 x\,d(x)\,dx = 1 \qquad \text{(momentum sum rule)}. \qquad (5.27)$$

The assumption of a uniform distribution in the plane (5.26) combined with the normalisation conditions (5.25) leads to

$$u(x) = 4\,(1 - x) \qquad d(x) = 2\,(1 - x) \qquad (5.28)$$

with average momentum fractions $\langle x_u \rangle = 2/3$, $\langle x_d \rangle = 1/3$.

Step B. DIS data show that quarks carry only about half of the proton momentum, the other half is carried by gluons:

$$\int_0^1 x\,[u(x) + d(x)]\,dx \approx 0.5 \qquad \int_0^1 x\,g(x)\,dx \approx 0.5, \qquad (5.29)$$

where g(x) gives the number of gluons carrying a fraction of the proton momentum between x and x + dx. Assuming $\langle x_u \rangle = 1/3$, $\langle x_d \rangle = 1/6$ and making the ansatz $u(x) = a\,(1-x)^n$ leads to

$$u(x) = 10\,(1 - x)^4 \qquad d(x) = 5\,(1 - x)^4. \qquad (5.30)$$

Since gluons carry no electric charge, flavor etc. their number in the proton is not constrained,

$0 \leq \int_0^1 g(x)\,dx.$

As a first guess for the gluon x spectrum one may assume one part to be similar to that for u and d quarks, and a second part to arise from gluon bremsstrahlung by quarks, which will depend on Q^2 and on α_S, the strong coupling:

$$g(x) = a(1-x)^4 + b\,x^{-1}(1-x)^4.$$

The gluon momentum sum rule (5.29) requires (a/6 + b) = 2.5. A possible choice is a = 3, b = 2 (actually, the resulting g(x) does not vary much in $0.1 < x < 0.5$ for a wide set of a,b values) leading to:

$$g(x) = 3(1-x)^4 + 2\,x^{-1}(1-x)^4. \qquad (5.31)$$

Step C: Gluons can split into a quark-antiquark pair, g -> q $\bar{q}$, called sea quarks (q_S) as distinguished from the valence quarks (q_V) considered before. The splitting depends on α_S and Q^2. Inclusion of the sea quarks leads to the following constraints:

$$u_S(x) = \bar{u}_S(x) = \bar{u}(x), \qquad d_S(x) = \bar{d}_S(x) = \bar{d}(x)$$

$$u(x) = u_V(x) + u_S(x) \qquad d(x) = d_V(x) + d_S(x)$$

$$\int_0^1 [u(x) - \bar{u}(x)]\,dx = \int_0^1 u_V(x)\,dx = 2$$

$$\int_0^1 [d(x) - \bar{d}(x)]\,dx = \int_0^1 d_V(x)\,dx = 1$$

$$\int_0^1 [s(x) - \bar{s}(x)]\,dx = 0$$

$$\int_0^1 x\,[u(x) + \bar{u}(x) + d(x) + \bar{d}(x) + s(x) + \bar{s}(x)]\,dx \approx 0.5$$

$$\int_0^1 x\,g(x)\,dx \approx 0.5. \qquad (5.32)$$

In view of the splitting process g -> $q_S\,\bar{q}_S$ it seems natural to assume that a sea quark carries half of the momentum of the parent gluon. Replacing x by 2x in the gluon distribution gives for the shape of the sea quark distribution

$$q_S(x) = \text{const.}\ [3(1-2x)^4 + x^{-1}(1-2x)^4] \qquad \text{for } x < 0.5.$$

In order to fix the constant we need to take recourse to data. From structure function fits to data (Martin, Stirling and Roberts 1993) the total momentum fraction carried by sea quarks at $Q^2 = 4$ GeV^2 is about 0.18 which determines the constant, provided all sea quark distributions are identical. The valence distributions need now to be corrected for the momentum carried by the sea quarks. With the ansatz $u_V(x) = a(1-x)^n$ the final result is

$$u_V(x) = 16(1-x)^7$$

$$d_V(x) = 8(1-x)^7$$

$$u_S(x) = d_S(x) = s_S(x) = (1-2x)^4 + (3x)^{-1}(1-2x)^4 \qquad \text{for } x < 0.5$$

$$g(x) = 3(1-x)^4 + 2\,x^{-1}(1-x)^4 \qquad (5.33)$$

The resulting parton density for the toy model are shown in fig. 25a. What can one learn from this exercise? The average momentum fraction of the sea quarks is expected to be smaller than that of gluons and the latter to be smaller than that of valence quarks. Furthermore, the proton structure function at $x < 0.01$ will be dominated by the sea quark and gluon contributions.

For comparison, fig. 25b shows the parton distributions obtained from a recent fit to data and evaluated at $Q^2 = 20$ GeV^2 (MRS 1993). The qualitative behavior shown by the toy model is quite similar to that found from the data. A quantitative comparison shows the data to require a wider valence quark distribution, more momentum for the valence u than for the valence d quarks and a steeper gluon distribution.

The parton distributions change with Q^2. Bremsstrahlung of gluons and gluon splitting will become more frequent as Q^2 increases, with the result, that valence quarks will carry less while gluons and sea quarks will carry more of the proton momentum. The predicted evolution of parton distributions with Q^2 is shown in fig. 26.

A recent review of pre-HERA experimental data on the nucleon structure functions has been given by Milsztajn and Virchaux (1993).

5.5 DIS cross sections at HERA energies

The structure functions measured in previous experiments have been extrapolated by QCD evolution with LEPTO (1988) using the parametrization EHLQ (Eichten et al. 1984, 1986) to the HERA regime. The numbers of events expected from NC and CC scattering are shown in fig. 27 at $Q^2 > 1000$ GeV^2 for an integrated luminosity of 500 pb^{-1}. The large NC rates at low Q^2 stem from photon exchange. At $Q^2 > M_Z^2$ contributions from Z - exchange become equally important. The requirement of a minimum of 100 events leads to a maximum Q^2 value of 35 000 GeV^2 up to which NC measurements are feasible.

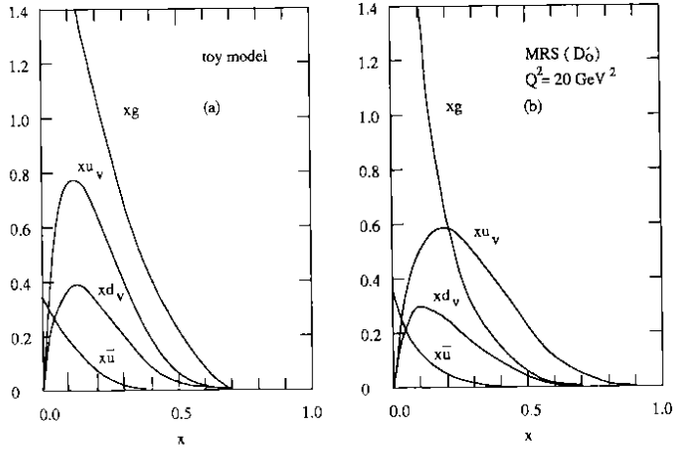

Fig. 25 Parton distributions of the proton
(a) from the toy model
(b) calculated for $Q^2 = 20$ GeV^2 from a fit to data (MRS 1993)

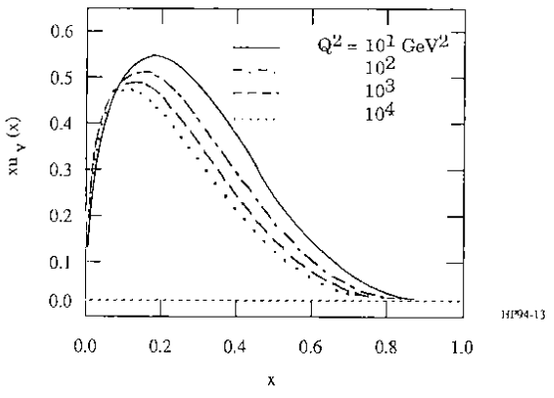

Fig. 26 The evolution of the valence u-quark distribution with Q^2: Q^2 = 10 (full), 10^2 (dash-dotted), 10^3 (dashed) and 10^4 (dotted) GeV^2, from Ingelman and Rückl (1987)

The event rate for CC scattering at low Q^2 is much smaller, for the reason discussed above. However, for Q^2 around M_Z^2 the CC and NC cross sections become approximately equal (see fig. 28); weak and electromagnetic interactions are of the same strength. The practical Q^2 limit for CC studies is around 40 000 GeV^2.

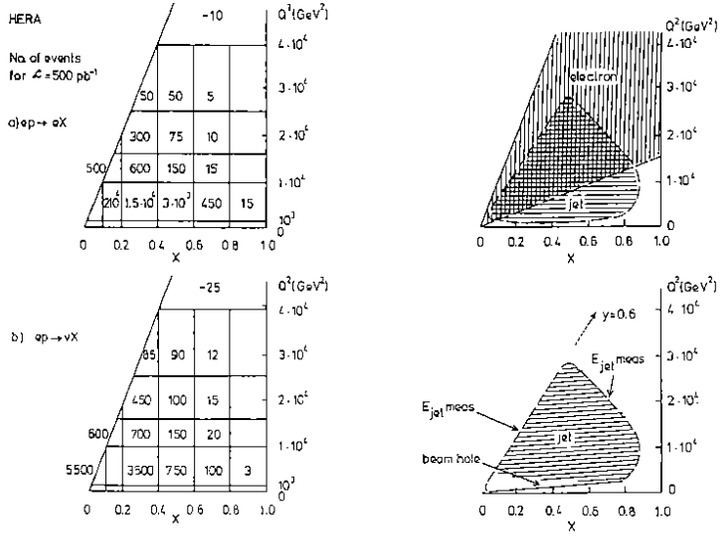

Fig. 27 Event numbers for NC and CC scattering at HERA with L = 500 pb^{-1} calculated with LEPTO and EHLQ structure functions, and the regions where x and Q^2 can be well measured at HERA for NC scattering, from either the electron or the hadronic system, and for CC scattering from only the hadronic system

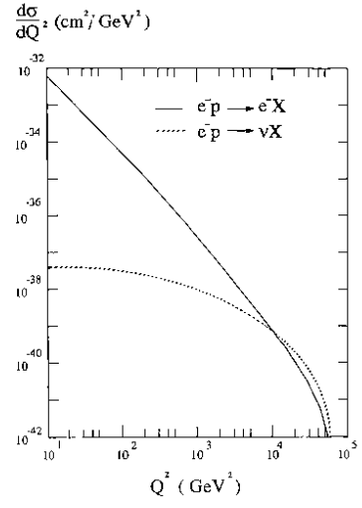

Fig. 28 The cross sections for NC and CC scattering as a function of Q^2

5.6 Small x physics

Small x physics is a new and exciting field of lepton - nucleon scattering. The possibility of accessing this region at HERA has stimulated an intense discussion. Since $x = Q^2/(2m_p\nu)$, small x - values are attained for fixed Q^2 by making the energy transfer ν large. For instance, for Q^2 = 10 GeV^2, x - values as small as 10^{-4} can be reached at HERA which is a factor of 100 smaller than in previous experiments (see table 2). The NC cross section is favorably large in this regime as shown in fig. 29: for instance, the nominal yearly luminosity of 100 pb^{-1} should yield 10^6 events with $10^{-4} < x < 10^{-3}$, $10 < Q^2 < 20$ GeV^2.

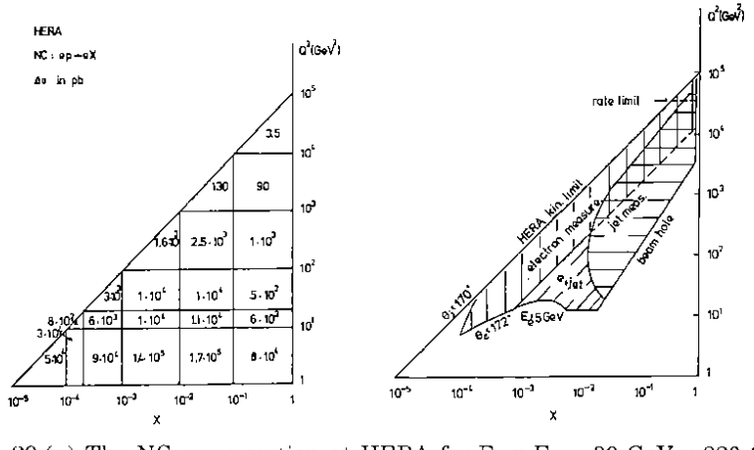

Fig. 29 (a) The NC cross section at HERA for E_e x E_p = 30 GeV x 820 GeV calculated with LEPTO and EHLQ structure functions; the numbers give the cross section (in pb) for given x - Q^2 bins.
(b) The region where x and Q^2 can be well measured

The excitement about the small x region stems from the fact that in perturbative QCD $F_2(x,Q^2)$ grows faster than any power of ln (1/x) as x -> 0 (De Rujula et al. 1974). Intuitively, this can be understood as follows (see Gribov, Levin and Ryskin 1983). Consider scattering (fig. 30a) at small x but not too small Q^2 such that α_s is small, e.g. $Q^2 > Q_0^2 = 10$ GeV^2. As x -> 0, the numbers of gluons and sea quarks in the proton are expected to grow beyond any limits due to bremsstrahlung and gluon splitting; for instance, the number of gluons with momentum fractions x, x+dx should behave as

$$g(x) \sim x^{-(1+\lambda)}, \quad \lambda \approx \alpha_s\,[12 \ln (2)]/\pi \approx 1/2 \text{ (Lipatov 1976 and others).}$$

Since the transverse size of the partons is fixed (~1/Q) and since the partons are confined to the proton and their number grows as x -> 0, there must be an $x = x_{crit}$ below which partons begin to overlap (fig. 31). This must lead to saturation of the structure functions as x -> 0 (fig. 32). A possible mechanism of parton overlap is depicted in fig. 30b : two ladders start from two different partons and begin to interact. A recent review of theoretical developments in small x physics was given by Kwiecinski (1993).

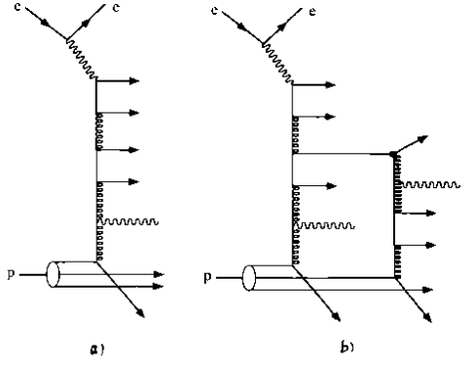

Fig. 30 Diagrams for low - x scattering: (a) with a single ladder, (b) with two ladders starting from two different incoming partons and where the two ladders interact

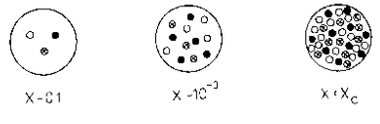

Fig. 31 The parton density in the nucleon for different values of x

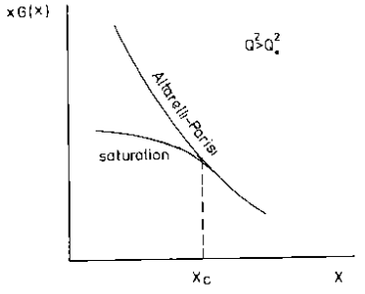

Fig. 32 Expected qualitative behavior of the gluon structure function at very small x values according to the GLDAP and BFKL evolution equations and after inclusion of saturation effects

Two estimates for x_{crit} are given in fig. 33 as a function of Q^2 (Kim and Ryskin 1991). The first is characterized by a parameter R = 5 GeV^{-1} which may be thought of as the radius of the proton for a uniform parton distribution in the proton. In this case the saturation region is barely within reach at HERA. For $Q^2 = 4$ GeV^2 the model predicts $x_{crit} = 10^{-4}$. However, the low - x partons may concentrate, for instance, around the valence quarks and form hot spots (Mueller 1991). Assuming a hot spot radius of 2 GeV^{-1} observation of saturation effects at HERA looks feasible (fig. 33). The amount of saturation one may expect, e.g. for the gluon structure function, is shown in fig. 34 for the two models.

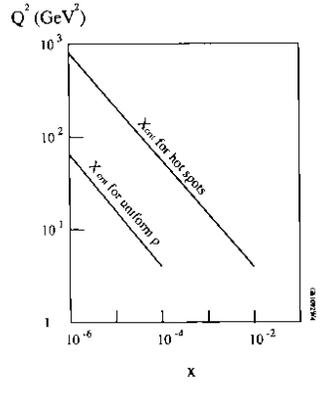

Fig. 33 Model predictions for the x - Q^2 behavior of x_{crit} for a uniformly populated proton (lower curve) and for the hot spot model (upper curve); taken from Kim and Ryskin (1991)

The smallest - x data for $Q^2 > 5$ GeV^2 that were available before HERA were obtained by NMC (1992). Figure 35 shows their recent measurements of F_2 in μp scattering for x - values between 0.008 and 0.5. It is noteworthy that the

predictions for F_2 obtained by fitting previous data from higher x - values (Kwiecinski et al., 1990, Morfin and Tung 1992, Glück et al., 1990) fail to fit the NMC data: the NMC data indicate a faster rise of F_2 as x approaches zero. Inclusion of the new NMC data in the structure function fits has resulted in the predictions (Martin et al., 1992) D_0 and D_- shown in fig. 36. The two sets differ in the assumption of whether the gluon structure function is constant or diverges as x goes to zero: $xG(x,Q^2) \sim$ constant ($\sim x^{-0.5}$) for D_0 (D_-). While the two sets give identical results for $x > 0.01$ they make markedly different predictions for F_2 for $x < 10^{-3}$: at $x = 10^{-4}$ F_2 as calculated from D_- is a factor of three larger. Also indicated in fig. 35 is an estimate of the effects of parton saturation on D_-; they are small for a uniform proton but large in the hot spot model for $x = 10^{-4}$.

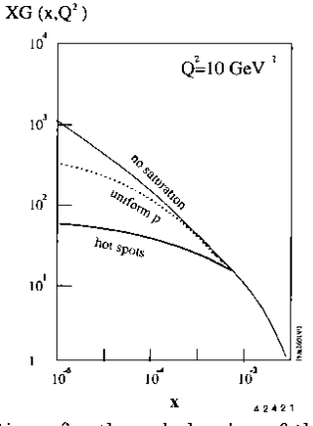

Fig. 34 Model predictions for the x behavior of the gluon structure function at $Q^2 = 10\ GeV^2$ assuming no saturation or saturation for a uniformly populated proton, and for the hot spot model (from Kim and Ryskin 1991)

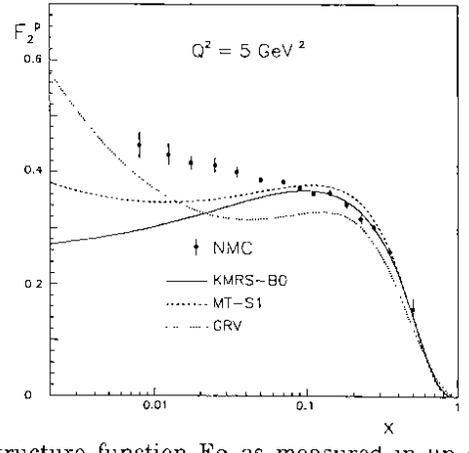

Fig. 35 The structure function F_2 as measured in μp scattering by NMC (1992), with predictions obtained from fits to previous DIS data Kwiecinski et al., 1990, Morfin and Tung 1992, Glück et al.,1990)

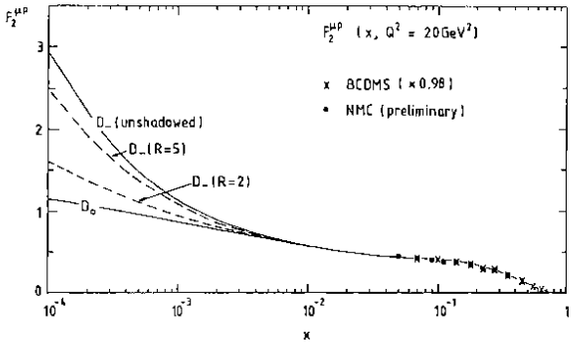

Fig. 36 Prediction for F_2 at very small x - values obtained from a fit (Martin et al., 1993) to new data from NMC (1992) and other experiments assuming as $x \to 0$: $x\,G(x) \sim x^{-0.5}$ (D_-) and $x\,G(x) \sim$ constant (D_0)

Deviations from the standard Altarelli - Parisi (GLDAP) evolution at very small values of x are also expected for a "technical" reason. In the GLDAP evolution for each additional factor of α_s only terms $\sim(\ln Q^2)\cdot(\ln 1/x)$ are kept while ($\ln 1/x$) terms are neglected. This approximation has been avoided in the BFKL evolution (Lipatov 1976, Kuraev et al., 1977, Balitskii and Lipatov, 1978).

5. 6. 1 Experimentally accessible x - Q2 region

Standard x - Q^2 region: The x - Q^2 region accessible to experiments depends on the structure of the events and on the detector. As discussed above, for NC events, the values of x and Q^2 can be determined from the energy and direction of *either* the scattered electron or the current jet. For CC events, where the scattered lepton is a neutrino, x and Q^2 can be measured only with the current jet. Figure 27 shows for nominal beam energies and standard x and Q^2 values the regions over which x and Q^2 can be measured well from the electron and the jet parameters, respectively. The main limitations stem from the precision with which the electron and jet energies can be measured, and from the size of the beam holes (see below). For NC scattering, structure function measurements should be feasible for basically the full range of x and Q^2. In the case of CC scattering precise measurements will be difficult for $y > 0.6$ and below $y \approx 0.04$. The well measured region can be extended by operating HERA at lower beam energies.

Small x - region: The major limitation for NC studies at very small x and low Q^2 values comes from the beam holes provided in the forward and rear calorimeters for beam passage. Typical cross sections of these holes are 20 x 20 cm^2 (ZEUS). The effective hole in the acceptance is somewhat larger since a reliable energy measurement requires the point at which the electron or the jet enters the calorimeter to be some distance away from the cutout. Figure 29 b shows an educated guess for the well measured region. It follows from the requirements

- $\Theta_{\text{current jet}} < 172^\circ$, $\Theta_{\text{electron}} < 172^\circ$, $E_{\text{electron}} > 5$ GeV

and from the size of the beam hole. The HERA experiments should be well suited for the region $x > 10^{-4}$, $Q^2 > 10\ GeV^2$.

6 Photoproduction

The high c.m. energy of HERA allows the study of photoproduction over a wide energy range. An introduction to photoproduction at HERA can be found in the Proceedings of the HERA workshops (e.g. Schuler 1991) and in reports by Levy (1992) and Schuler and Sjöstrand (1993).

Besides $p\bar{p}$ interactions, γp scattering is the only other hadronic or hadron - like reaction which can currently be measured at c.m. energies above 100 GeV. In the Vector Dominance Model (VDM) the photon can fluctuate into a low-mass vector meson V (ρ^0, ω, ϕ ..) which in turn interacts with the proton (fig. 37). As a result, γp scattering can be related to Vp scattering, and via the quark - parton model, to $\pi^{\pm}p$ and $K^{\pm}p$ scattering. For instance, the predictions for forward production of vector mesons are:

$$d\sigma^0/dt\,(\gamma p \rightarrow Vp) = [(\alpha/4) / (\gamma_V^2/4\pi)]\; d\sigma^0/dt\,(Vp \rightarrow Vp)$$

$$= [(\alpha/64) / (\gamma_V^2/4\pi)]\; (1 + \eta_V^2)\; \sigma_{tot}^2\,(Vp)$$

with

$$\sigma_{tot}\,(\rho^0 p) = \sigma_{tot}\,(\omega p) = 0.5\,[\,\sigma_{tot}\,(\pi^+ p) + \sigma_{tot}\,(\pi^- p)]$$

$$\sigma_{tot}\,(\phi p) = \sigma_{tot}\,(K^+ p) + \sigma_{tot}\,(K^- n) - \sigma_{tot}\,(\pi^+ p) \qquad (6.1)$$

where γ_V measures the strength of the γ - V coupling, $\gamma_V^2/4\pi = (\alpha^2/12)\, M_V/\Gamma_{ee}$ = 0.50±0.03, 5.8±0.2 , 3.3±0.13 for ρ^0, ω, ϕ respectively (PDG 1992), t is the four momentum transfer squared, and η_V is the ratio of the real-to-imaginary parts of the elastic scattering amplitude; for diffractive scattering $\eta_V = 0$.

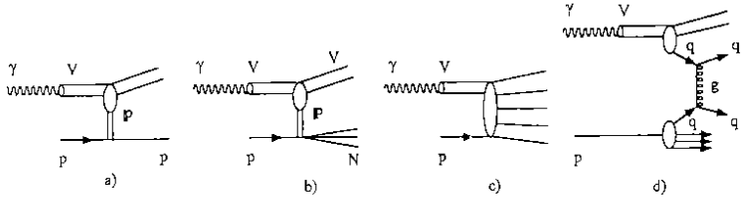

Fig. 37 Diagrams for photoproduction via VDM by (a) elastic and (b) inelastic diffractive scattering, (c) by nondiffractive proceses and (d) hard scattering

Like purely hadronic reactions, photoproduction is expected to have a soft component due to peripheral processes (fig. 37a-c), and a hard component arising from the scattering of a parton from the proton on a parton from a vector meson (fig. 37d). However, in addition to its hadronic features, the photon possesses a property which makes it distinctly different from hadrons: it can couple directly to quarks and the coupling is pointlike. This leads to additional hard scattering processes which become prominent at high energies and which are not present in hadron - hadron interactions. They are represented by two types of diagrams: the first ("direct photon process") results from photon - gluon fusion into a quark - antiquark pair (fig. 38a) and from

photon scattering off a quark in the proton under the emission of a gluon ("QCD Compton process"), see fig. 38b. The quarks coupling to the photon can also emit gluons (e.g. fig. 38c), and either a quark or a gluon may participate in the hard scattering (fig. 38d,e). Together with the hard scattering of the hadronic (VDM) photon the hard scattering due to the quark and gluon content of the photon constitute the "resolved photon processes".

The need for extra contributions beyond those predicted by VDM and direct processes was found in the analysis of high p_T hadron production by $\gamma\gamma$ - scattering at PETRA (JADE 1981,TASSO 1981,1984, PLUTO 1984, see also Kolanoski 1984) and recently at KEK (AMY 1992, 1993, TOPAZ 1993). AMY and TOPAZ showed that resolved processes can in principle provide for these extra contributions.

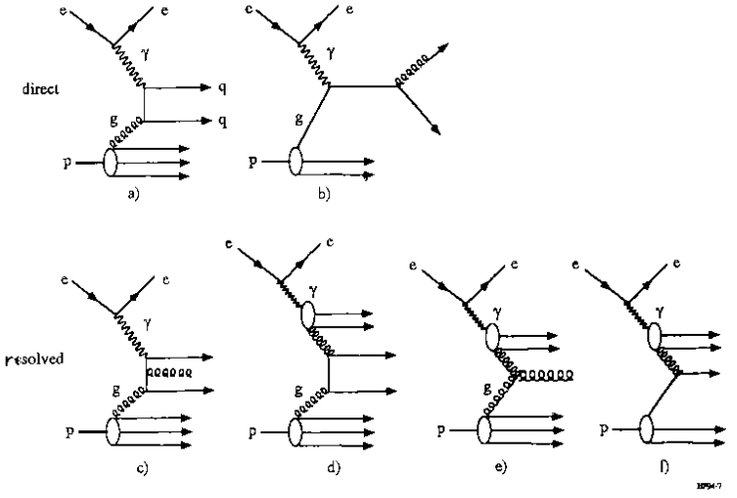

Fig. 38 Diagrams for direct photon processes: (a) BGF, (b) QCDC and (c - f) for resolved photon processes

The resolved contributions are summed in the photon structure functions F^{γ} which describe the quark and gluon content of the photon (note: part if not all of the hard scattering contributions from VDM and from the quark and gluon content of the photon are presumably identical and care must be taken to avoid double counting). A selection of current predictions for F^{γ} labelled DG (Drees and Grassie, 1985), LAC1, LAC2, LAC3 (Abramowicz et al., 1991), GRV (Glück et al. 1993) and GS (Gordon and Storrow 1992) is shown in fig. 39.

The hard photon processes - direct or resolved - give rise to quark and gluon jets (sometimes called "minijets") with large transverse momenta. Their cross sections have been calculated and found to depend critically on the minimum momentum transfer p_{Tmin} down to which the integration is performed. As will be seen below, at HERA energies hard scattering originating from photon constituents is clearly visible.

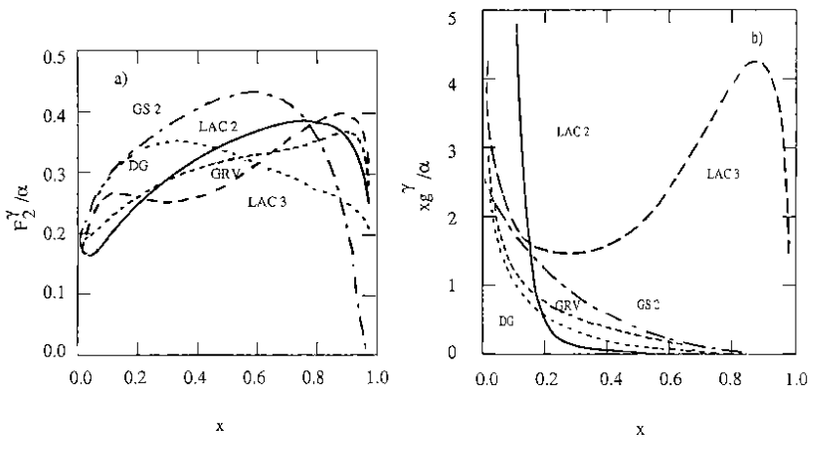

Fig. 39 Parametrizations of the photon structure function (from Drees and Godbole 1992)

6.1 Total photoproduction cross section

In electron - proton collisions quasi-real photons are produced by bremsstrahlung of the electron on the proton. The photon energy E_γ can be determined by measuring the energy of the scattered electron, $E_{e'}$, in the electron calorimeter of the luminosity monitor, yielding $E_\gamma = E_e - E_{e'}$. The photon-proton c.m. energy, W, is given by $W^2 = 4 E_\gamma E_p$. For instance, E_γ = 12 GeV corresponds to W = 200 GeV.

The photon flux is roughly given by $dN_\gamma \approx \alpha/(2\pi) \ln (Q^2_{max})/(m_e^2)\, dE_\gamma/ E_\gamma$ or $dN_\gamma \approx 0.015\, dE_\gamma/ E_\gamma$ which leads to the following relation between the ep and γp cross sections,

$$\sigma(ep) \approx 0.015 \int dE_\gamma/ E_\gamma \; \sigma_{tot}(\gamma p).$$

The complete Weizsäcker - Williams approximation gives the following result:

$$\frac{d\sigma(ep)}{dy} = \frac{\alpha}{2\pi} \{ \frac{[1 + (1 - y)^2]}{y} \ln [\frac{Q_{max}^2}{Q_{min}^2}] - 2 [\frac{1 - y}{y}] [1 - \frac{Q_{min}^2}{Q_{max}^2}] \} \sigma_{trans}(\gamma p) \qquad (6.2)$$

where $y = E_\gamma/ E_e$, Q_{max}^2 is given by the acceptance for the electron detector, $Q_{min}^2 = m_e^2 y^2/(1 - y)$ and $\sigma_{trans}(\gamma p)$ is the cross section for transverse photons. Note, that for typical settings at HERA the second term in (6.2) contributes about 8% (B. Burow 1993) and should not be neglected.

The event rate for photoproduction is very large at HERA; e.g. selecting photon energies between 10 and 20 GeV and assuming $\sigma_{tot}(\gamma p)$ = 140 μb produces 10^5 events for an integrated luminosity of 100 nb^{-1}. The large rate has permitted the two experiments, H1 and ZEUS, to make a measurement of $\sigma_{tot}(\gamma p)$ with a few nb^{-1} of data collected in the first weeks of data taking in 1992. The results were

$\sigma_{tot}(\gamma p)$ = 159 ± 7 (stat) ± 20 (syst) μb <W> = 195 GeV, H1 (1992)
154 ± 16 (stat) ± 32 (syst) μb 210 GeV, ZEUS (1992a).

The main difficulty in the determination of $\sigma_{tot}(\gamma p)$ lies in the fact that the detector acceptance is strongly process dependent. While for soft and hard processes the acceptance is above 80%, it is only 20 - 30% for the "elastic" diffractive reactions, $\gamma p \to Vp$, $V = \rho^0, \omega, \phi$ (fig. 37a) and sensitive to the details of the production mechanism. The truely elastic reaction, $\gamma p \to \gamma p$, is expected to have a cross section which is two orders of magnitude smaller compared to the vector meson processes. The acceptance for inelastic diffraction by dissociation of the photon into higher mass states and/or of the proton into heavier states, $\gamma p \to VX, \to X_1X_2$, lies in between. Figure 40 shows from H1 for charged particles the distributions of the transverse momentum p_T and the polar angle θ. The data (figs. 40a,c) are well described by the Monte Carlo simulation of the sum of diffractive, soft and hard contributions shown separately in figs. 40b,d.

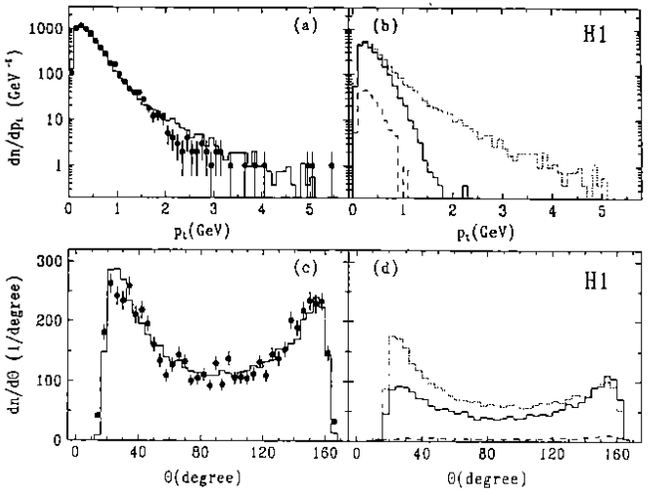

Fig. 40 Inclusive transverse momentum (a) and polar angle (c) distributions of charged particles in photoproduction events (points) compared to the Monte Carlo simulation. In (b) and (d) the MC constributions of the diffractive (dashed), soft (solid) and hard (dotted) components are shown (from H1 1992)

The H1 and ZEUS experiments repeated the measurement of $\sigma_{tot}(\gamma p)$ with the data from Fall 1992 providing an order of magnitude increase in statistics and allowing for a detailed study of the acceptances.

H1, from a study of 16000 photoproduction events obtained with 21.9 nb^{-1}, found (H1 1993 d):

$$\sigma_{tot}(\gamma p) = 156 \pm 2\,(stat) \pm 18\,(syst)\ \mu b.$$

ZEUS analysis: A sample of about 6000 photoproduction events from 13 nb^{-1} was selected with a tagged electron in the energy range 15.2 - 18.2 GeV corresponding to W values between 167 and 194 GeV (ZEUS 1993j,l,m). The value of Q^2 was less than 0.02 GeV^2 which implies an expected change of $\sigma_{tot}(\gamma p)$ compared to its value at $Q^2 = 0$ of less than 1%.

The energy distributions observed for the events in the forward (FCAL), barrel (BCAL) and rear (RCAL) calorimeters are shown in fig. 41. In the E_{FCAL} distribution a distinct class of events is observed with very little energy deposition. These events originate mainly from elastic and inelastic diffractive processes which are characterized by producing very little transverse energy in the forward (= proton) direction.

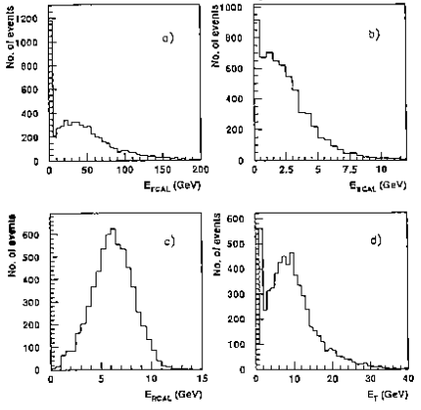

Fig. 41 Distribution in the calorimeter of the energy deposited (a) in the forward, (b) barrel, (c) rear sections and (d) total transverse energy (ZEUS 1993j,l,m)

From a study of the events with $E_{FCAL} < 1$ GeV the acceptances and contributions of diffractive processes were determined by comparing the data with various models and Monte Carlo simulations (PYTHIA 1987, 1989, HERWIG 1986, 1992, Nikolaev - Zakharov 1992, 1993). The spatial distribution of the energy deposition in the rear direction permitted the separation of the elastic and inelastic diffractive contributions: photon dissociation into low-mass states deposits energy more closely to the incoming photon direction than high- mass states. The acceptance and contribution from nondiffractive processes were determined using the events with $E_{FCAL} > 1$ GeV. The result for the total cross section is

$$\sigma_{tot}(\gamma p) = 141 \pm 3\,(stat) \pm 17\,(syst)\ \mu b.$$

Figure 42 shows $\sigma_{tot}(\gamma p)$ as a function of W above the resonance region (W > 1.75 GeV) as measured in previous experiments up to 18 GeV(S. Alekhin et al., 1987) and by H1 and ZEUS. No dramatic rise is observed between 18 and 200 GeV.

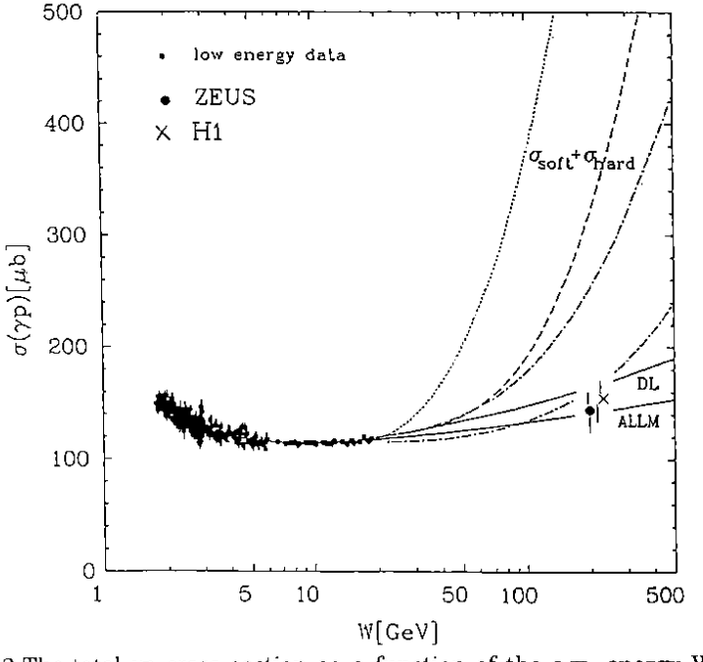

Fig. 42 The total γp cross section as a function of the c.m. energy W as measured below 18 GeV and by H1 and ZEUS near W = 200 GeV. The lower solid curve is the prediction of the ALLM parametrization and the higher solid curve is that of DL. The dotted (dashed) line uses the LAC1 parametrization for F^{γ} with $p_{T min} = 1.4$ GeV/c (2 GeV/c). The dashed-dotted lines use the DG parametrization for F^{γ} with $p_{T min} = 1.4$ GeV/c (upper line) and $p_{T min} = 2$ GeV/c (lower).

The curve labelled DL in fig. 42 is the prediction of a Regge - type fit to hadron -hadron and pre - HERA photon-proton cross sections of the form

$$\sigma_{tot} = X\, s^{\varepsilon} + Y\, s^{-\eta} \qquad (6.3)$$

where the first term describes Pomeron contributions and the second one those from ρ, ω, f and a exchange (Donnachie and Landshoff 1984). The values of ε, η were obtained from fits to pp and $p\bar{p}$ data alone yielding $\varepsilon = 0.0808$ and $\eta = 0.4525$ while the coefficients X, Y were determined by fitting the low energy data on $\sigma_{tot}(\gamma p)$. The curve ALLM (Abramowicz et al., 1991) is also a Regge-type analysis with an ansatz which provides a smooth transition from the

photoproduction to the DIS region. The parameters of the model were obtained by a simultaneous fit to the data for $\sigma_{tot}(\gamma p)$ and DIS at low energy. Both predictions agree rather well with the HERA data.

Observations of "diffractive" air showers (Chacaltaya and Pamir 1990) and an excess of muons in energetic air showers (Yodh 1990) have suggested $\sigma_{tot}(\gamma p)$ to rise much faster than $\sigma_{tot}(p\bar{p})$ at beam energies above ~ 100 TeV. This rise has been attributed to semi-hard scattering involving resolved photon contributions. The other curves shown in fig. 42 are based on the assumption that the total cross section is a sum of a soft part plus the contributions from direct and resolved photons (Drees and Grassie, 1985, Fletcher et al., 1992, Ghandi and Sarcevic, 1991, Forshaw and Storrow, 1991, Schuler and Terron, 1991). They depend critically on the choice of the photon structure function F^{γ} and on the parameter $p_{T\min}$, the lower integration limit for the hard process in QCD, where p_T is the parton transverse momentum. The dashed-dotted lines use the DG parametrization of F^{γ} with $p_{T\min} = 2.0$ GeV/c for the lower (1.4 GeV/c for the upper) line. The dashed (dotted) line uses the LAC1 version with $p_{T\min} = 2.0$ (1.4) GeV/c. Only the dashed - dotted curve - which makes the lowest cross section prediction - is in agreement with the HERA data. Besides experimental data on the photon structure function higher order calculations are needed in order to assess the behavior of $\sigma_{tot}(\gamma p)$ above HERA energies. Furthermore, corrections for multiple parton interactions may have to be taken into account.

6.2 Partial photoproduction cross sections

The ZEUS analysis of $\sigma_{tot}(\gamma p)$ also provided measurements of the cross sections for the nondiffractive and diffractive channels:

$\sigma_{nondiff} = 91 \pm 11$ μb

$\sigma_{el\ diff} = 17 \pm 8$ μb

$\sigma_{inel\ diff} = 33 \pm 9$ μb.

The cross section $\sigma_{el\ diff}$ for $\gamma p \rightarrow Vp$, $V = \rho^0 + \omega + \phi$, is shown in fig. 43 together with measurements at low energies. The full curve is a calculation based on VDM, the quark model and the observed energy dependence of $\sigma_{tot}(\gamma p)$. It agrees with the data.

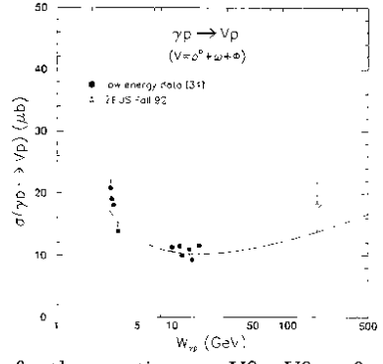

Fig. 43 Cross section for the reaction $\gamma p \rightarrow V^0 p$, $V^0 = \rho^0, \omega, \phi$ ZEUS (1993j,l)

Direct observation of $\gamma p \rightarrow \rho^0 p$ was reported by both experiments. The $\pi^+\pi^-$ mass distribution as measured with the tracking systems is shown in fig. 44 exhibiting a clear ρ^0 signal.

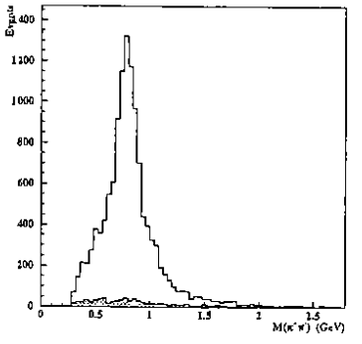

Fig. 44 The $\pi^+\pi^-$ mass distribution from untagged photoproduction (shaded distribution for same sign charged particles); from ZEUS (1993j,l)

A model of the build-up of the total photon proton cross section by soft processes, diffractive scattering and direct and resolved (called anomalous) photon contributions is shown in fig. 45 (Schuler and Sjöstrand 1993).

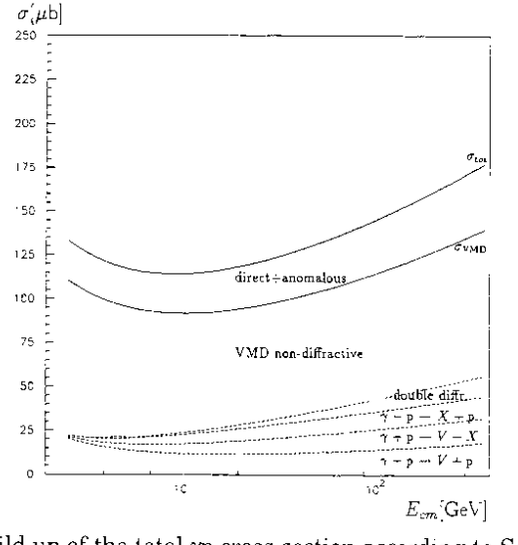

Fig. 45 Build up of the total γp cross section according to Schuler and Sjöstrand (1993)

6.3 Events with a large rapidity gap

In DIS a new class of events was found by ZEUS (1993g) and confirmed by H1(1993j,k) which are characterized by a large rapidity gap between the proton beam direction and the first significant energy deposition away from it. The observation of large rapidity gaps provides a new window for a measurement of the diffractive contribution (elastic and inelastic). It will be discussed in some detail in the section on DIS results.

A search in photoproduction showed the presence of the same type of events (ZEUS 1993j,l). The analysis was performed in terms of the pseudorapidity η = - ln tan (θ/2). In fig. 46a the distribution of η_{max} is shown where η_{max} is the pseudorapidity of the condensate closest to the proton direction - i.e. with the maximum η. A condensate is a group of contiguous calorimeter cells with a total energy > 0.4 GeV. The data fall into two groups, a large peak at η_{max} values between 3 to 6 consisting mainly of nondiffractive events and described by a Monte Carlo simulation of nondiffractive processes (solid histogram), and a second peak near $\eta_{max} \approx -2$ arising from diffractive production. The distribution of M_X^2, where M_X is the mass of the diffractive system, shows the bulk of the events to have low masses, $M_X < 10$ GeV (fig. 46b). Note, the data are not corrected for acceptance.

The elastic and inelastic diffractive processes discussed before contribute to these large rapidity gap events.

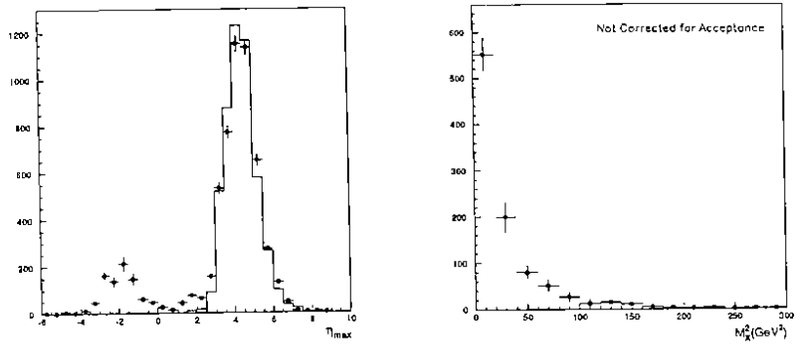

(a) (b)

Fig. 46 Tagged photoproduction (ZEUS 1993j,l):
(a) Distribution of η_{max} for data (points) and prediction for nondiffractive photoproduction (histogram)
(b) Distribution of the mass squared for the hadron system produced in events with a large rapidity gap ($\eta_{max} < 2$)

6.4 Hard scattering in photoproduction

6.4.1 Considerations of kinematics

While the observed size and energy dependence of the total cross section $\sigma_{tot}(\gamma p)$ do not provide evidence for the direct and resolved photon contributions, the analysis of the final states shows the presence of these terms very clearly in the hard scattering contributions.

The direct and resolved processes (fig. 38) produce quarks and gluons in the final state. At sufficiently high energies the final state partons manifest themselves as jets of hadrons. Let us estimate how high the energy has to be in order to recognize these jets. Consider Compton scattering of a photon on a quark carrying a fractional momentum x as depicted in fig. 47a. The c.m. energy squared of the final state qg system is

$$\hat{s} = 4 E_\gamma x E_p = x W^2 \qquad (6.4)$$

or $\hat{s} \sim (0.001 - 0.01)\, W^2$ for typical values of x. In fig. 47b the fragmentation process is sketched in the qg rest system. From e^+e^- data one knows that the average transverse momentum of the outgoing hadrons w.r.t. the parton direction (fig. 47c) is $\langle p_T \rangle \approx 0.3$ GeV, approximately independent of the parton energy, $E_q^* = \hat{s}^{1/2}$; the average hadron multiplicity $\langle n \rangle$ grows slowly with E_q^* ($\langle n \rangle \approx n_0 + a \exp [b (\ln \hat{s}/\Lambda^2)^{1/2}]$, $n_0 = 3$, $a = 0.4$, $b = 1.93$ for $\Lambda = 0.3$ GeV). Therefore the average longitudinal momentum p_L increases rapidly with E_q^* and the half-opening angle of the jet cone $\langle \delta \rangle$ (fig. 47c,d), defined as $\langle \delta \rangle = \langle p_T \rangle / \langle p_L \rangle$, shrinks with energy: jets become more jetty as the energy increases. This is illustrated in table 3 for a few parton energies.

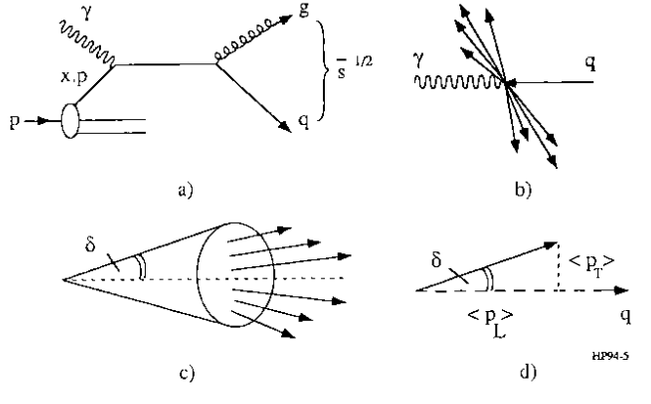

Fig. 47 The QCD Compton process (a) producing (b) two back-to-back jets in the photon-quark c.m. system; (c) the jet cone (d) with opening angle δ defined by the average longitudinal and transverse momenta

Table 3 Jet collimation as function of parton energy

E_q^* (GeV)	<n>	$<\delta> = <p_T>/<p_L>$
2	3	31^0
5	5	19^0
20	11	10^0

As seen from Table 3, $(\hat{s})^{1/2} = 2\,E_q^*$ needs to be at least 10 GeV and therefore W at least ~ 100 GeV for well collimated jets to emerge.

It is convenient to analyze the jet production at HERA in terms of transverse momentum p_T and pseudorapidity η rather than in terms of p_T and the longitudinal momentum p_z. The pseudorapidity is an approximation of the rapidity Y defined as

$$Y = 0.5 \ln [(E + p_z) / (E - p_z)] \qquad (6.5)$$

where E is the particle energy. A longitudinal transformation into a system which moves with velocity ß transforms Y into

$$Y^* = Y + 0.5 \ln [(1 + ß)/(1 - ß)]. \qquad (6.6)$$

The transformation causes a shift, $\Delta Y = Y^* - Y$, but does not alter the shape of the rapidity distribution (fig. 48).

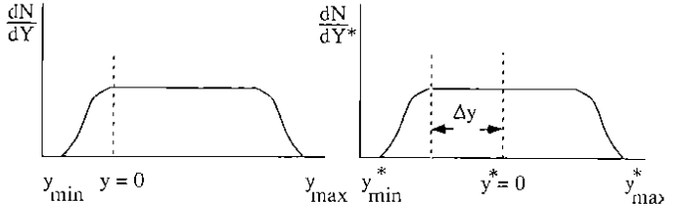

Fig. 48 The rapidity distribution in two Lorentz frames seprated by a longitudinal transformation

The invariant cross section expressed in terms of p_T, Y reads

$$E\, d^3\sigma / d^3p = d^3\sigma / dp_T^2\, dY \qquad (6.7)$$

which is a particularly useful relation when the cross section factorizes into a p- - dependent and a Y dependent term.At energies large compared to the particle's mass, E » m,

$$Y \approx 0.5 \ln [\{1 + \cos\theta + m^2/(2\,p^2)\} / \{1 - \cos\theta + m^2/(2\,p^2)\}] \qquad (6.8)$$

The minimum and maximum rapidities are reached for $\cos\theta = \pm 1$:

$$Y_{min} \approx - \ln (2\,p / m) \qquad Y_{max} \approx \ln (2\,p / m) \qquad \text{for } E » m \qquad (6.9)$$

For $1 - |\cos\theta| » m^2/(2p^2)$ the rapidity can be approximated by the pseudorapidity,

$$\eta = - \ln \tan (\theta/2). \qquad (6.10)$$

In two-to-two parton scattering such as in direct or resolved photon scattering depicted in fig. 49, the momenta of the incoming partons can be calculated from the two partons observed in the final state. Let x_γ and x_p be the fractions of the photon and proton momenta carried by the interacting partons. The assumption that the photon and proton remnants carry no transverse momenta plus energy-momentum conservation lead to

$$x_p = \Sigma_{partons} (E + p_z)_{parton} / (2\,E_p)$$
$$x_\gamma = \Sigma_{partons} (E - p_z)_{parton} / (2\,yE_e) \qquad (6.11)$$

where E_γ is the initial photon momentum and the sum is over the two final state partons. For the direct process, $x_\gamma = 1$. The expression for x_γ can be rewritten in the form (Barger and Phillips 1987):

$$x_p = \Sigma_{partons} E_{Tparton} [\exp(\eta_{parton})] / (2\,E_p)$$
$$x_\gamma = \Sigma_{partons} E_{Tparton} [\exp(-\eta_{parton})] / (2\,y\,E_e) \qquad (6.12)$$

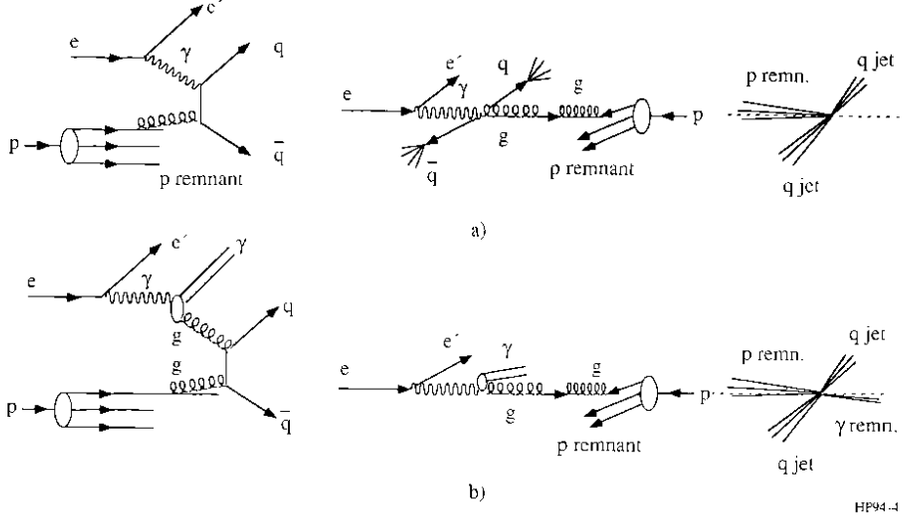

Fig. 49 The topology of hard scattering events from a direct photon process (a) with a proton remnant in the forward direction and two jets, and a resolved photon process (b) with a proton remnant, two jets and a photon remnant in the rear direction

The final state partons fragment into jets. The jet energies and momenta can be used to estimate the energies and momenta of the final state partons. Using the energy observed by the calorimeter cells assigned to the jet to evaluate the jet energy and longitudinal momentum and since $E_\gamma \approx y\, E_e \approx y_{JB}\, E_e$ one can approximate x_γ and x_p as

$$x_p^{meas} = \Sigma_{jets}\,(E + p_z)_{jet} / (2\,E_p)$$

$$x_\gamma^{meas} = \Sigma_{jets}\,(E - p_z)_{jet} / \Sigma_h\,(E - p_z)_h \qquad (6.13)$$

or $$x_p^{meas} = \Sigma_{jets}\,E_{T\,jet}\,[\exp(\eta_{jet})] / (2\,E_p)$$

$$x_\gamma^{meas} = \Sigma_{jets}\,E_{T\,jet}\,[\exp(-\eta_{jet})] / (2\,E_\gamma) \qquad (6.14)$$

where the sum in the denominator runs over all calorimeter cells. Here x_γ is the fraction of $\Sigma_h\,(E - p_z)_h$ carried by jets; the energy of the photon remnant is $(1-x_\gamma)\,E_\gamma$.

6.4.2 Experimental results on hard photoproduction

A first indication for the presence of hard scattering contributions in photoproduction was observed by the Omega-Photon collaboration (1989) when comparing the p_T distribution of charged particles produced by γp and $\pi^{\pm} p$ or $K^{\pm} p$ scattering. The data shown in fig. 50 were obtained for beam energies of 110 - 170 GeV, corresponding to W's of 14 - 18 GeV. The p_T spectrum produced by photoproduction is somewhat harder than in hadron - hadron scattering for $p_T > 2$ GeV.

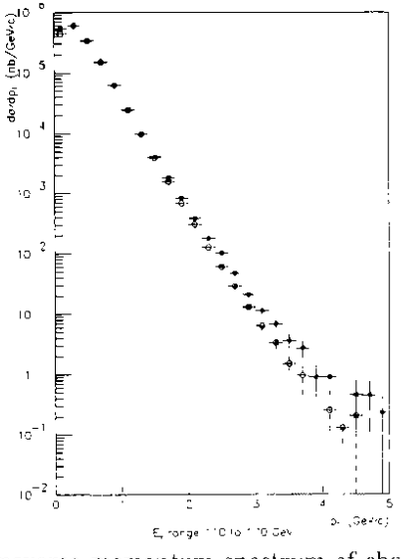

Fig. 50 The transverse momentum spectrum of charged particles produced by photon proton (full points) and hadron proton scattering (open points) for beam energies between 110 and 170 GeV (OMEGA 1989)

H1 analysis (1993e,j,k): The p_T distribution of charged particles measured by H1 for tagged events at an average W = 197 GeV is shown in fig. 51a (H1 1993j, k). The photoproduction result from the Omega experiment is included for comparison. The high energy data reach to much larger p_T values (8 GeV/c versus 4 GeV/c) and exhibit a much harder spectrum; e.g. at $p_T = 4$ GeV the cross section for W = 197 GeV is a factor of ~ 50 larger compared to ~16 GeV. The relative contribution from hard scattering increases with c.m. energy. The p_T spectrum from photopoduction is significantly harder than the one measured by UA1 (1990) for $\bar{p}p$ scattering at the same c.m. energy of 200 GeV (fig. 51b).

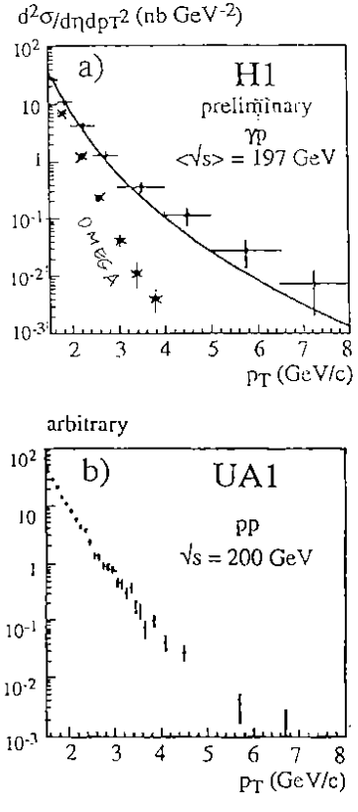

Fig. 51 a) Inclusive charged track ep cross section for $|\eta| < 1$ at W = 197 GeV, $Q^2 \approx 0$ (H1 1993j,k). Also shown are the photoproduction data from OMEGA (1989) for W around 17 GeV arbitrarily normalized. The curve shows an arbitrarily normalized spectrum from an NLO QCD calculation of resolved photon interactions (Borzumati et al., 1993)

b) The same spectrum measured at the same c.m. energy in $\bar{p}p$ interactions by UA1 (1990). Figure taken from H1 (1993j,k)

Evidence for jet formation (H1 1993j,k) can be seen from fig.52 where for charged tracks the p_T flow is shown as a function of $\Delta\phi$, the distance in azimuthal angle from the track with the highest p_T. While soft events show no structure in $\Delta\phi$, when the total transverse energy E_T per event detected by the calorimeter is above 10 GeV particles begin to cluster in opposite cones. A jet search was performed using a cone algorithm (UA1 1983, Huth et al., 1990). Jets were required to have $E_T > 7$ GeV in a cone of $\Delta R = (\Delta\eta^2 + \Delta\phi^2)^{1/2} = 1$. They were selected in the range $-1 < \eta < 1.5$. In fig. 53a , the ep cross section, corrected for detector effects to the hadron level, is shown as a function of E_T. A steep drop is observed with E_T. The η dependence of the jet cross section is given in fig. 53b. The curves show leading order (LO) QCD predictions calculated with PYTHIA for different parametrizations of F^γ : LAC2, LAC3, GRV-LO and GRV-LO without gluons. The predictions agree with the measured E_T dependence - with the exception of LAC3 - while none of them reproduces well the observed η dependence.

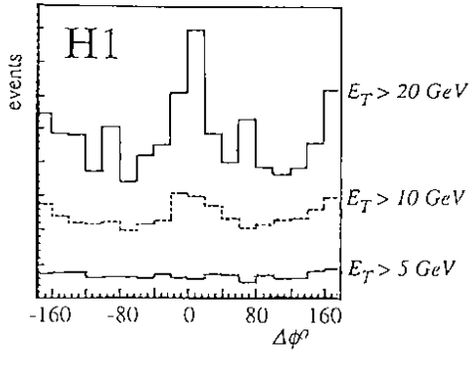

Fig. 52 Distribution of the distance $\Delta\phi$ in azimuth ϕ of charged tracks from the charged track with the largest p_T as a function of the total transverse energy E_T measured in the calorimeter (H1 1993j,k)

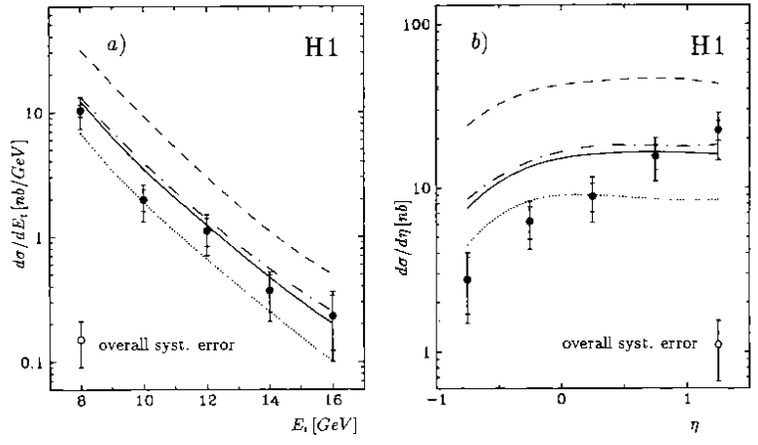

Fig. 53 (a) Inclusive jet E_T spectrum integrated over $-1.0 < \eta < 1.5$.
(b) Inclusive jet η spectrum for jets with $E_T > 7$ GeV. The curves represent LO calculations done with PYTHIA using for F^γ LAC3 (dashed), LAC2 (dashed-dotted), GRV-LO (full) and GRV-LO, but excluding the gluons originating from the photon (dotted); (H1 1993e)

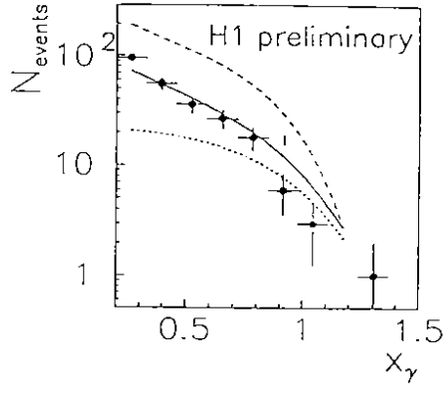

Fig. 54 Momentum fraction of partons from photons. Curves are LO calculations as in fig. 53; (H1 1993e)

The x_γ distribution was determined from a sample of two-jet events according to eq. 6.14. About 800 two-jet tagged photoproduction events were selected with the requirement that each jet has a transverse energy $E_{T\,jet} > 5$ GeV and $|\eta| < 2.5$. The data, not corrected for detector smearing are shown in fig. 54. The distribution falls rapidly with increasing x_γ. The data were compared with the LO QCD model used already for fig. 53. The curves shown in fig. 54 were

calculated by generating events with PYTHIA according to the model and passing them through the H1 detector simulation and reconstruction chain. The choice of a large gluon component in the photon as presented by LAC3 is disfavored by the data. The dotted curve shows the prediction assuming no gluons from the photon are involved in the interaction. The prediction undershoots the data at low x_γ, where gluons are expected to be important.

ZEUS analysis: Hard scattering in photoproduction was studied as follows (ZEUS 1992b). About 20% of all photoproduced events have a total transverse energy $E_T > 10$ GeV while soft photoproduction is expected to have $E_T < 10$ GeV. A substantial fraction of high E_T events shows two back-to-back jets. A spectacular event is shown in fig. 55, where two jets with about 30 GeV are visible plus a proton remnant. Since no energy is deposited in RCAL, where one would expect the fragments of the photon remnant in a resolved process, this event is a candidate for a direct photon interaction.

Clear evidence for resolved photon processes can be seen in the characteristics of the two-jet sample (ZEUS 1992b, 1993i). The kinematics for direct and resolved photon processes is illustrated in fig. 49. In direct processes the final state consists of the two parton jets, the scattered electron close to the electron beam and the proton remnant close to the proton beam. For resolved processes there is in addition the photon remant which is emitted in the direction of the incident photon (= direction of the incident electron) which may reveal itself as energy deposition in the rear calorimeter. In fig. 56 the energy deposited in RCAL coverin η values between -0.75 and -3.8 is plotted against the pseudorapidity, η_{min}, of the most

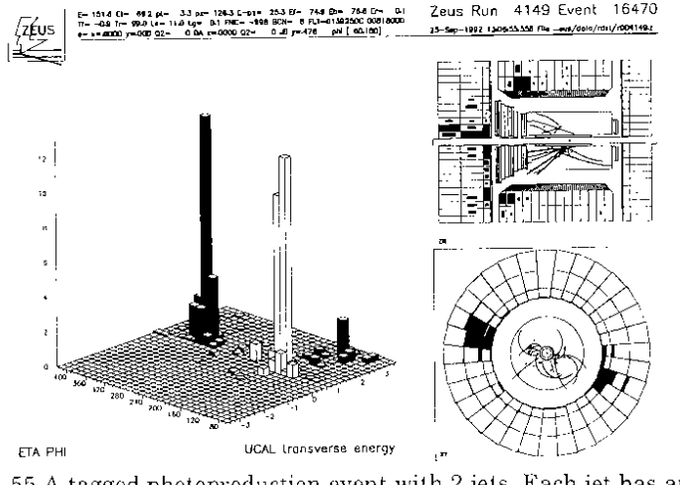

Fig. 55 A tagged photoproduction event with 2 jets. Each jet has an energy of about 30 GeV. This is a candidate for a direct photon interaction since there is no evidence of a photon remnant in the rear calorimeter.

backward jet. If both jets go forward $\eta_{min} > 0$. If direct photon interactions were the sole origin of these events, sizeable energy in RCAL would be expected for

events with $\eta_{min} < -0.25$, falling essentially to zero as the jets become more distant from the RCAL region. This trend is indeed observed in fig. 56. However, there is an additional group of events with energy deposition in RCAL as large as 16 GeV even when both jets are far away from RCAL, the nearest jet being as much as three units of pseudorapidity away. This substantial RCAL energy is explained as the remnant of the photon in resolved photon processes.

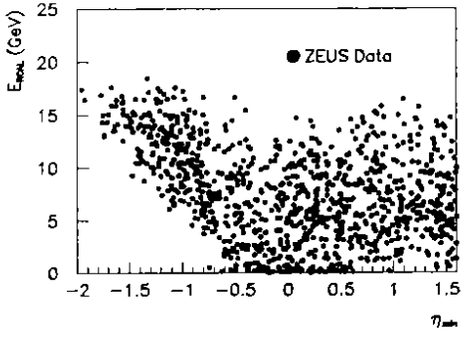

Fig. 56 The energy deposited in RCAL plotted against the pseudorapidity, η_{min}, of the most backward jet (ZEUS 1993j,l)

The distribution of the transverse energy $E_{T\,jet}$ of the photoproduced jets is shown in fig. 57a for $\eta_{jet} < 1.6$ (ZEUS 1993i). Jets with E_T up to 19 GeV are seen. The data are well reproduced by a LO QCD calculation performed within the HERWIG Monte Carlo program which considered direct and resolved processes. Initial and final state parton showers were included and the simulated events were passed through the detector and reconstruction chain. According to the model resolved photon contributions are dominant; the direct contributions approach the resolved ones as $E_{T\,jet}$ increases beyond 20 GeV. The η_{jet} distribution is shown in fig. 57b. Also shown are the LO QCD predictions. The direct and resolved contributions show quite different distributions: in the resolved case only a fraction of the photon's momentum participates in the hard scatter such that the center of mass is in general more strongly boosted in the proton direction. The data require a substantial contribution from resolved processes.

Two-jet production was studied requiring both jets to have $\eta_{jet} < 1.6$. The di-jet mass distribution shows masses up to 40 GeV (fig. 58). The distributions of the proton momentum fraction x_p^{meas} and photon momentum fraction x_γ^{meas} calculated according to (6.13) are displayed in fig. 59 for events with $|\eta_{jet1} - \eta_{jet2}| < 1.5$ and $|\phi_{jet1} - \phi_{jet2}| > 120^o$. The latter cuts were applied in order to improve the resolution for x_γ^{meas}. The bulk of the events have x_p^{meas} values between $3 \cdot 10^{-3}$ and $3 \cdot 10^{-2}$. The x_γ^{meas} distribution rises at both low and high values. The Monte Carlo simulations of the direct and resolved processes have very different characteristics. The resolved processes show a rise towards low x_γ^{meas}, as observed in the data but cannot account for the rise at high x_γ^{meas}.

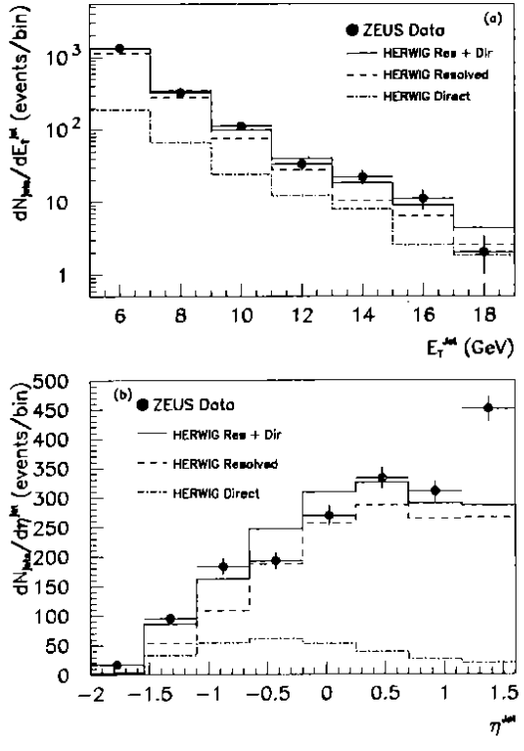

Fig. 57 Inclusive jet distributions for (a) transverse energy of jets, (b) pseudorapidity of jets. The Monte Carlo predictions are normalized to the data in the region $\eta_{jet} < 1.2$. Also shown are the relative contributions of the direct and resolved processes as predicted by Monte Carlo (ZEUS 1993i)

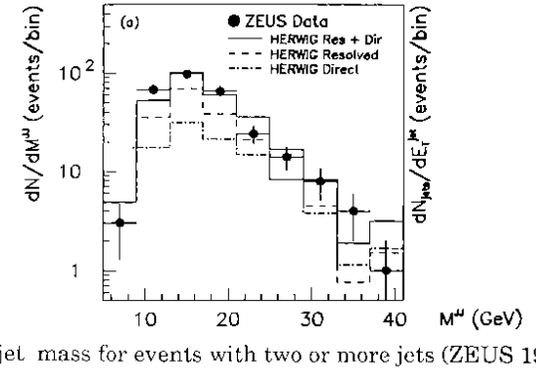

Fig. 58 Two-jet mass for events with two or more jets (ZEUS 1993i)

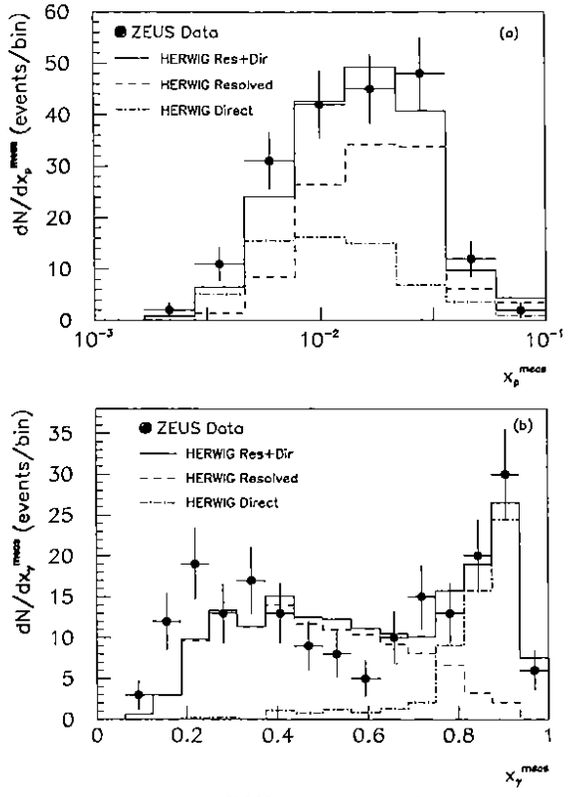

Fig. 59 Distributions of (a) x_p^{meas} and (b) x_γ^{meas} for events with two or more jets. The Monte Carlo distributions show the fit of the resolved plus direct contributions to the data in (b) (ZEUS 1993i)

The direct processes predict a sharp rise towards high x_γ^{meas} as observed in the data, and only a small number of events for $x_\gamma^{meas} < 0.7$. This is an unambiguous signature for the presence of direct processes. The di-jet ep cross sections of quasireal photons in the region $0.2 < E_\gamma/E_e < 0.7$, $E_{T_{jet}} > 5$ GeV and $\eta_{jet} < 1.6$ were found to be

$21.1 \pm 5.2(\text{stat}) \pm 5.7(\text{syst})$ nb for resolved processes, and

$9.4 \pm 2.7(\text{stat}) \pm 2.7(\text{syst})$ nb for direct procceses.

6.5 Discussion of the photoproduction results

The first analyses of H1 and ZEUS have shown that photoproduction is accessible at HERA almost up to the kinematic limit. The total photoproduction cross section does not exhibit a dramatic rise in the HERA regime but behaves rather hadron-like. The final states show very clearly the presence of hard scattering manifesting itself in a hardening of the transverse momentum

distributions and the production of energetic and large transverse momentum jets. The existence of direct and resolved photon processes have been established unambiguously from the study of two-jet production. At moderate transverse momenta the resolved process is the dominant one. The ensuing picture for the photon in hard scattering (fig. 60) is then either a photon which interacts with a parton (direct process) or a photon which is a bag full of quarks and gluons, of which one interacts with a parton (resolved process).

From the observed features of the data, the determination of the photon structure function via photoproduction of jets looks promising. Important prerequisites for such analyses are next-to-leading order (NLO) QCD calculations. First results of such calculations have become available recently (Gordon and Storrow 1992, Bödeker 1992, Borzumati el al., 1993, Kramer and Salesch 1993, Greco and Vicini 1993). The expected dependence of the jet p_T distribution from resolved processes is shown in fig. 61.

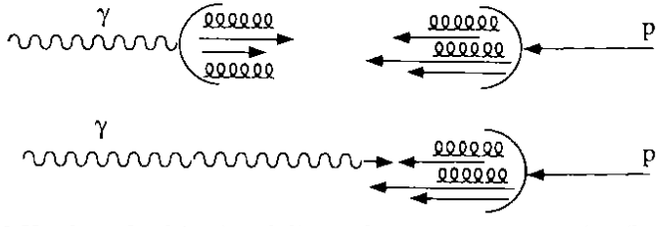

Fig. 60 Hard resolved (top) and direct photon proton scattering (bottom)

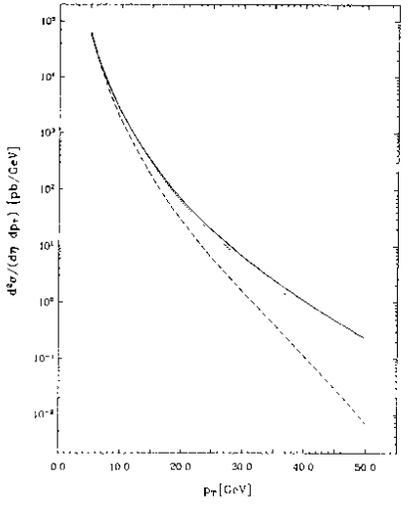

Fig. 61 Dependence on the transverse jet momentum p_T of the full NLO cross section for jet cone radius R = 1 and jet rapidities in the lab. of η = 1 (full), η = 2 (dotted) and η = 3 (dashed); from Kramer and Salesch (1993)

7 DIS and structure functions of the proton

H1 analysis: The inclusive cross section for ep -> eX was determined from Fall 1992 data based on a luminosity of 22.5 nb^{-1} (H1 1993f,i). The scattered electron was detected in the rear (electromagnetic) calorimeter BEMC and by the tracking detectors in front of the BEMC providing the energy E_e' and scattering angle $\theta_{e'}$. The electron variables were determined from the electron based values of x_e, y_e, Q_e^2 according to (5.1). The observed E_e' and $\theta_{e'}$ distributions (fig. 62) are well reproduced by the detector simulation program. The hadron system was measured by a combination of calorimetric measurements and reconstructed charged tracks in the central region yielding the hadron side variables x_h, y_h, Q_h^2 according to (5.3). For Q^2, the electron measurement Q_e^2 was used since it has the better resolution. The y value was taken from y_e except for $y_h < 0.3$ where y_h was chosen since it gave a more precise measurement. For a part of the analysis a mixture of electron and hadron information was used to calculate x, $x_m = Q_e^2/(s\, y_h)$.

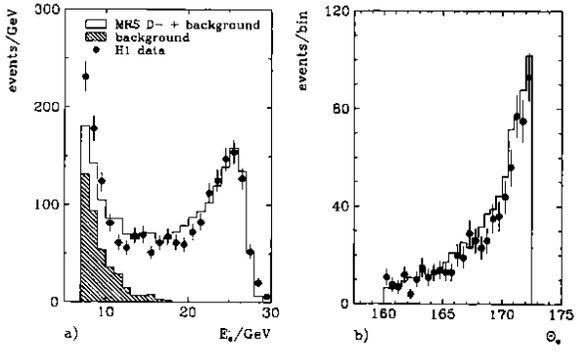

Fig. 62 Distribution of (a) the energy E_e' of the scattered electron before some of the selection cuts; (b) the electron scattering angle $\theta_{e'}$. (H1 1993f,i)

The analysis was restricted to Q^2 - values between 5 and 80 GeV^2. For the extraction of the structure function F_2, the contribution of the longitudinal part, F_L, was calculated from QCD. Its contribution to the DIS cross section was found to be small, being at most 8%. Corrections for QED radiative effects were applied using TERAD91 (1991) or HERACLES (1992). The F_2 results obtained from a total of 1026 events are summarized in figs. 63, 64 for fixed bins of Q^2 and x. The systematic errors range from 15 - 22% to which a global uncertainty from normalization of 8% has to be added.

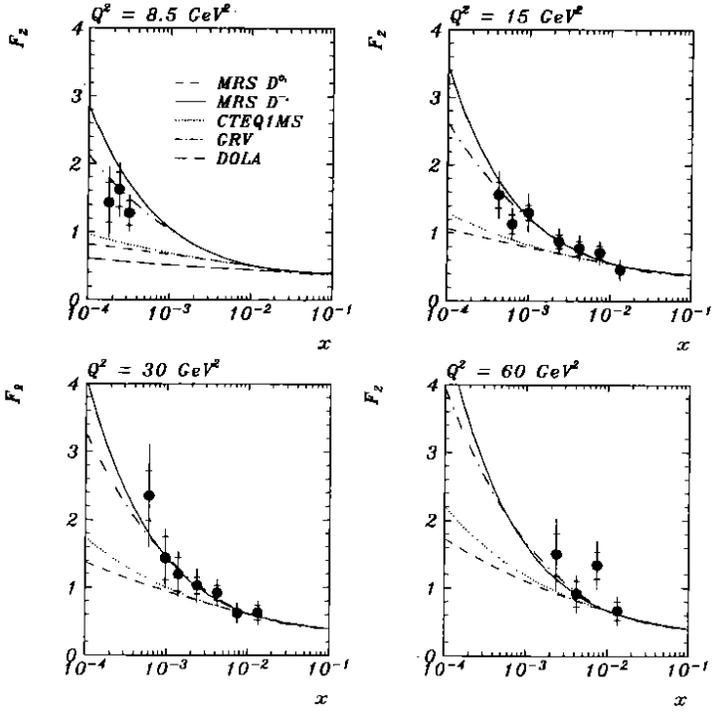

Fig. 63 The structure function $F_2(x, Q^2)$ for different Q^2 intervals. The error bars show statistical and total errors (H1 1993f)

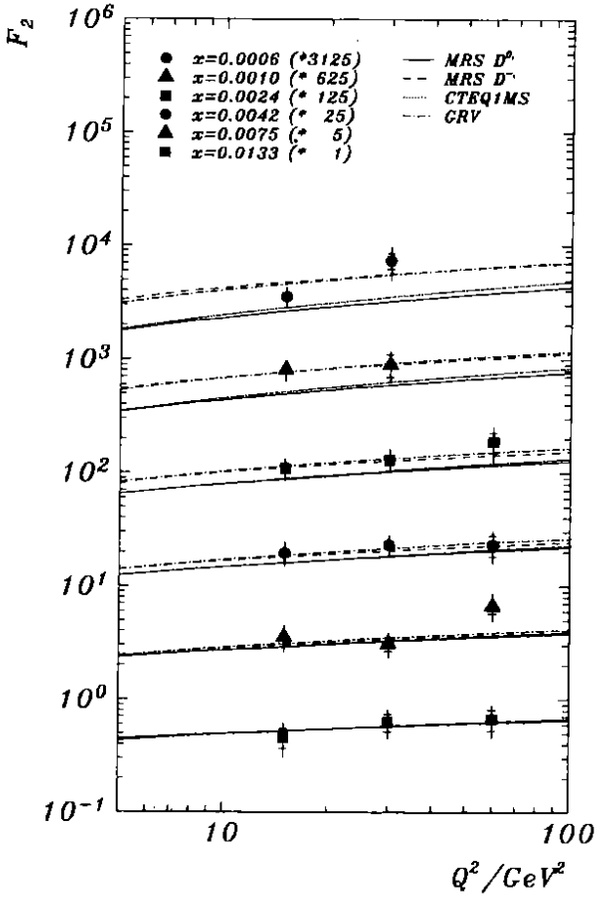

Fig. 64 The structure function $F_2(x, Q^2)$ as in fig. 63 for different x intervals (H1 1993f)

ZEUS analysis: The data sample used for the determination of F_2 was obtained in the fall of 1992 and corresponds to a luminosity of 24.7 nb^{-1}(ZEUS 1993h). The kinematic properties of the scattered electron and produced hadrons were determined with the calorimeter. The values of x and Q^2 were calculated with the double - angle method (eq. 5.6) providing x_{DA}, $Q_{DA}{}^2$ from the measured angles of the scattered electron and the hadron system. The measured x_{DA} and $Q_{DA}{}^2$ distributions are in agreement with the expected ones (fig. 65a,b). The distribution of the events in the x_{DA}, $Q_{DA}{}^2$ plane is displayed in fig. 65c with $Q_{DA}{}^2$ reaching up to 4700 GeV^2. Also indicated in fig. 65c is the kinematical area covered by non-HERA experiments.

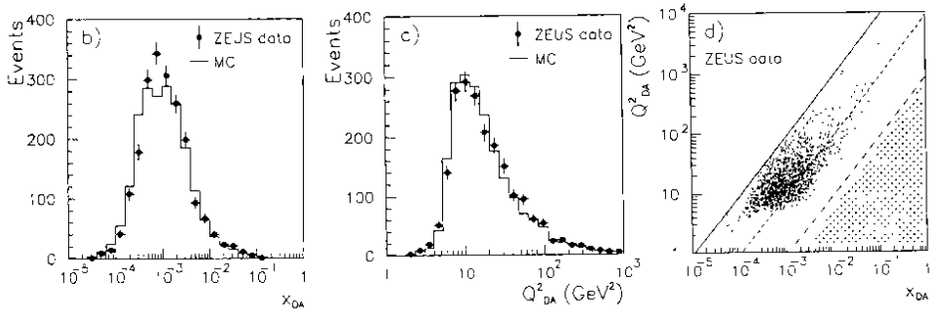

Fig. 65 The measured x and Q^2 distributions and a plot of x versus Q^2 (ZEUS 1993h). The shaded area in (c) shows the x - Q^2 region covered by fixed target experiments

The structure function analysis was performed for $Q^2 > 10$ GeV^2 with 1299 events in the chosen x, Q^2 bins. The contribution from F_L was calculated from QCD giving a maximum correction of 12%. Corrections for radiative effects from QED processes were calculated with HERACLES. Figures 66, 67 show F_2 as a function of x and Q^2. The systematic errors range from 7 to 31%; a global normalization uncertainty of 7% has to be added.

7.1 Discussion of the F_2 results

The results on F_2 from H1 and ZEUS are summarized in fig. 68. Also shown in fig. 68 are measurements from BCDMS (1989) and NMC (1992). The HERA data connect on nicely with the BCDMS and NMC results. The HERA data extend the x-range for F_2 by two orders of magnitude down to $x = 1.6 \cdot 10^{-4}$. As x decreases from 10^{-2} to $4 \cdot 10^{-4}$ the structure function rises by a factor of 2 - 3 as reported for the first time by H1 (1993i). The Q^2 dependence of F_2 for fixed x is

shown to be in good accord with the expected logarithmic violation of scaling (fig. 64, 67).

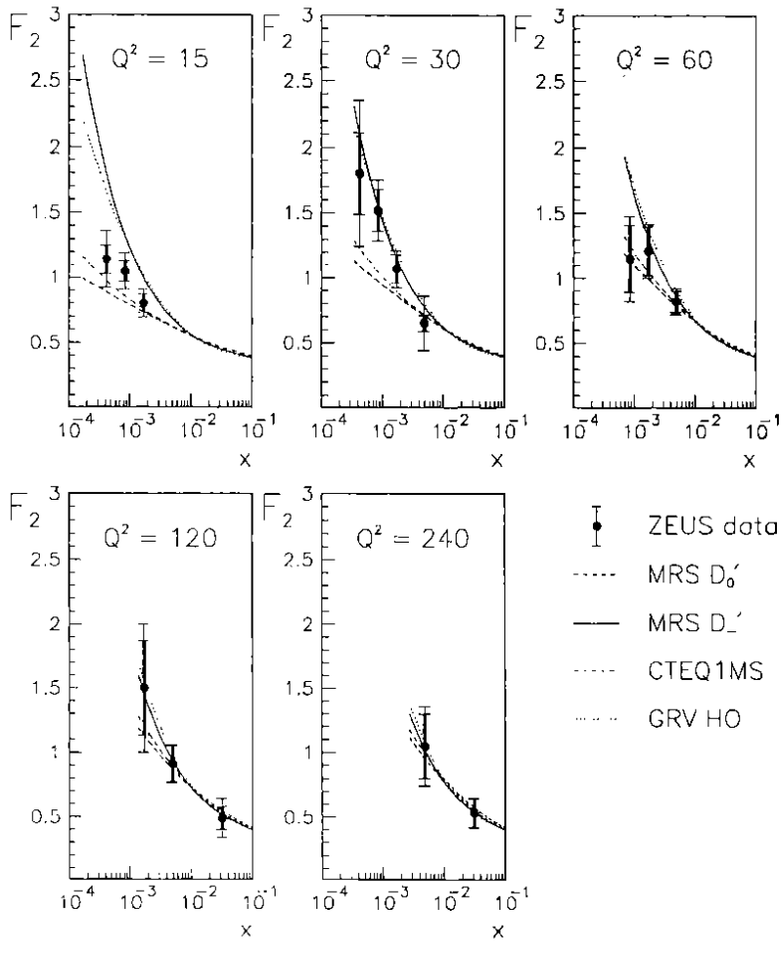

Fig. 66 The structure function $F_2(x, Q^2)$ for different Q^2 intervals. The inner error bars are the statistical errors, and the outer error bars show the systematic errors added in quadrature (ZEUS 1993h)

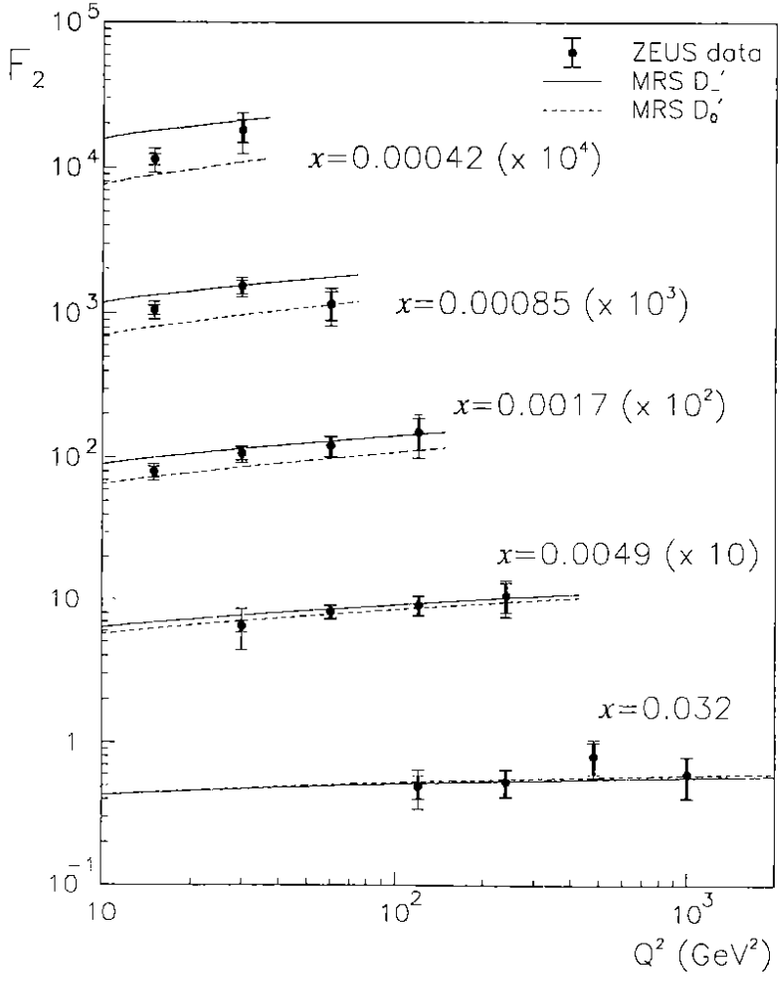

Fig. 67 The structure function $F_2(x, Q^2)$ as in fig. 66 for different x intervals (ZEUS 1993h)

The data on F_2 are compared in fig. 68 with different extrapolations or predictions. MRS (D_') , MRS (D_0') (Martin, Stirling and Roberts 1993) and CTEQ 1MS (CTEQ 1993) are extrapolations of structure function parametrizations obtained from fits to low - energy data at larger x values. For MRS (D_') the small x evolution of the gluon density at Q_0^2 = 4 GeV^2 is singular (x g(x) = G(x) ~ $x^{-0.5}$, Lipatov behavior), while it is constant for MRS (D_0') (G(x) -> const for x -> 0). Note, that MRS D_0' evolved downwards below Q^2 = 4 GeV^2 would lead to negative parton densities. For CTEQ 1MS the gluon density is singular, but the sea quark distribution is not strongly coupled to the gluon density, leading to a slower rise of F_2 with decreasing x. GRV HO (Glück, Reya and Vogt 1993) is the prediction of a higher - order QCD calculation. Following a proposal by Parisi and Petronzio (1976) the small x partons are radiatively generated according to the GLAP equations, starting from "valence like" quark and gluon distributions at Q_0^2 = 0.3 GeV^2 (see fig. 69). This procedure has been questioned because of the small value of $Q_0^2 \approx 5 - 10\ \Lambda^2$ at which the evolution starts (see e.g. Forshaw 1993). The parametrization DL (Donnachie and Landshoff 1993) is a Regge theory motivated fit, which is applicable for Q^2 values up to about 10 GeV^2. It is worth noting that all five sets of structure functions give a good fit to the non-HERA data, covering x values above ~ 0.04, and that it takes measurements at much smaller x values such as available at HERA to select between the different physics possibilities.

The GRV HO and MRS (D.') curves reproduce the F_2 data reasonably well while CTEQ 1MS, MRS (D_0') and DL fall below the measured points (fig. 68). The conclusion then is that the data prefer a rising gluon density leading also to a rising sea quark density as x decreases. An important message from GRV is that F_2 at low x may change rapidly with Q^2 between ~ 0.5 and 10 GeV^2 and precise data in this region will be of great importance. The Q^2 behavior expected by GRV (1992) can be seen from fig. 70. The figure shows also that for Q^2 below 5 GeV^2 higher order QCD corrections become large.

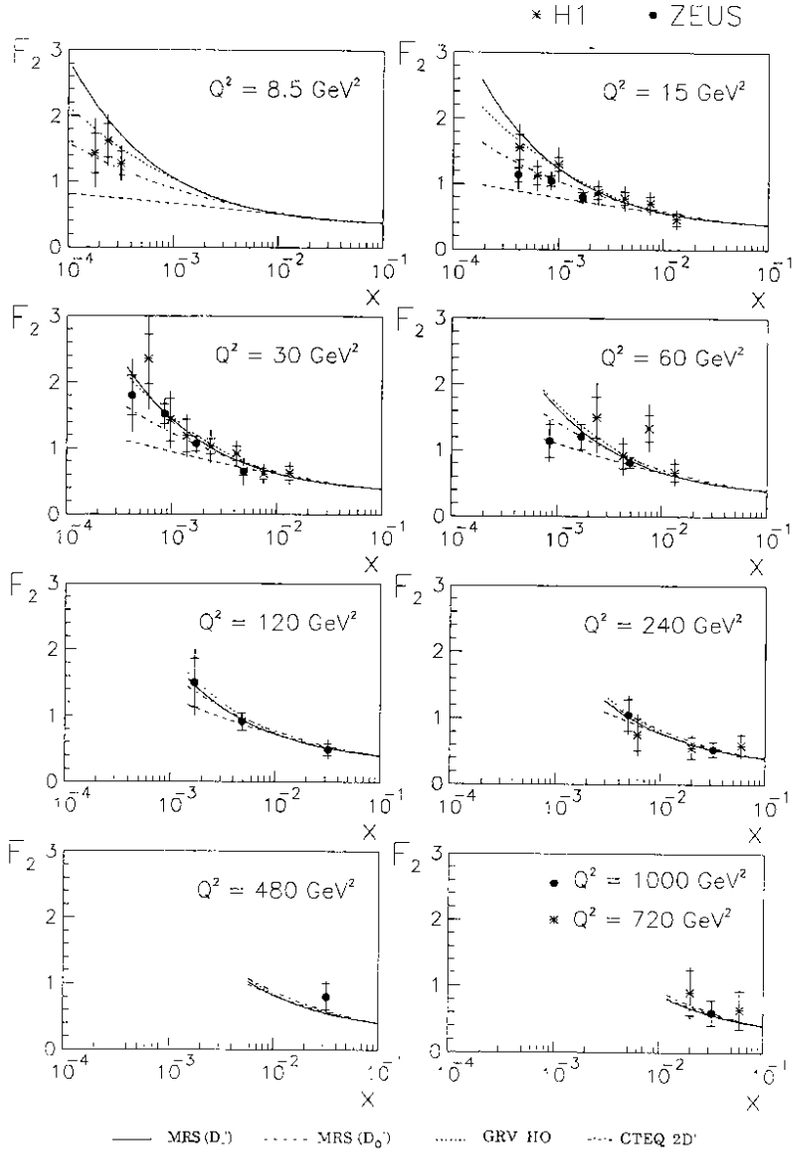

Fig. 68 The $F_2(x, Q^2)$ data from H1 and ZEUS for fixed Q^2. The curves show the prametrizations MRS (D_'), MRS (Do') and CTEQ 2D' and the prediction GRV HO.

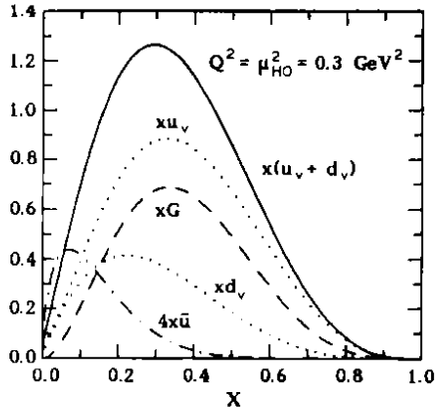

Fig. 69 The "valence" parton distributions of GRV from which the evolution is started at Q_0^2 (GRV 1992)

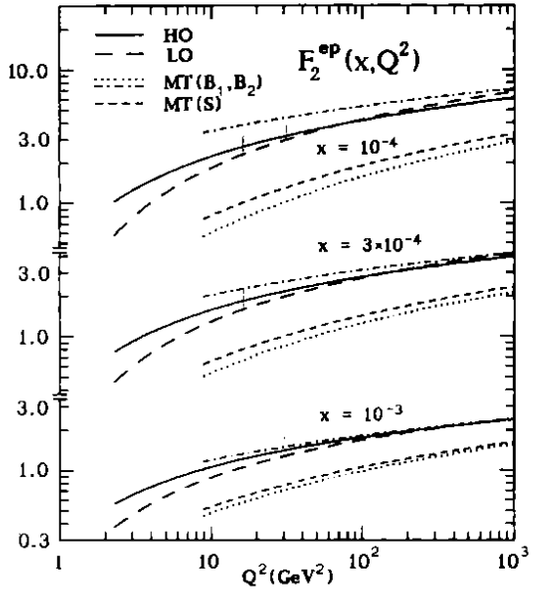

Fig. 70 The GRV (1992) prediction for the Q^2 dependence of $F_2(x, Q^2)$ in leading (LO) and higher order (HO). Shown are also parametrizations by Morfin and Tung (1991)

7.2 Scaling violations of F_2 and the gluon structure function

The Q^2 dependence of F_2 at small values of x can be related in a straightforward albeit approximate way with the gluon density $G(x,Q^2)$ of the proton. This was shown by Prytz (1993) following a procedure which had been applied before to derive $G(x,Q^2)$ from the longitudinal structure function $F_L(x,Q^2)$ (Cooper-Sarkar et al., 1988). It is instructive to follow the exercise in some detail (Roco 1993).

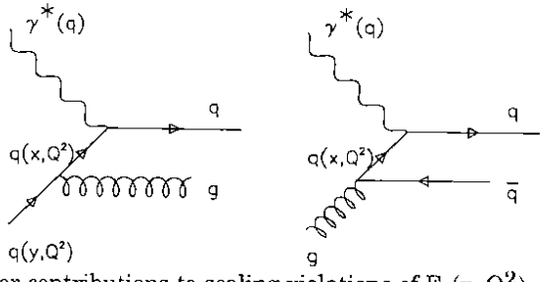

Fig. 71 Lowest order contributions to scaling violations of $F_2(x, Q^2)$

Leading-order (LO) QCD diagrams are shown in fig. 71: in the first process a quark carrying a momentum fraction y of the proton emits a gluon, retains a fraction x of the proton momentum and scatters on the virtual photon. In the second process the proton emits a gluon which splits into a $q\bar{q}$ pair one of which, carrying a fraction x of the proton momentum, interacts with the virtual photon. The GLAP evolution equation for the density of quark i which interacts with the photon reads:

$$dq_i(x, Q^2)/d\ln Q^2 = \alpha_s(Q^2)/(2\pi) \int_x^1 dy/y \; \{P_{qq}(x/y)\, q_i(y,Q^2) + P_{qg}(x/y)\, g(y,Q^2)\} \qquad (7.1)$$

$\alpha_s P_{qq}(x/y)$ is proportional to the probablity that a quark with momentum fraction x has come from an initial state quark with momentum fraction y which has radiated a gluon.

$\alpha_s P_{qg}(x/y)$ is proportional to the probability that a quark with momentum fraction x has come from a $q\bar{q}$ pair created by a gluon.

In LO

$$\alpha_s(Q^2) = 12\pi / [(33 - 2N_f)\ln(Q^2/\Lambda^2)] \qquad (7.2)$$

where N_f is the number of flavors. Since the typical mass of the $q\bar{q}$ pair is < 10 GeV, $N_f = 4$ seems a good assumption. From (5.21) and (7.1) follows:

$$F_2(x,Q^2) = x \sum_q e_q^2\, q(x,Q^2)$$

$$dF_2/d\ln Q^2 = \sum_q e_q^2\, \alpha_s(Q^2)/(2\pi) \int_x^1 dy/y \; \{P_{qq}(x/y)\, q_i(y,Q^2) + P_{qg}(x/y)\, g(y,Q^2)\} \qquad (7.3)$$

At very low x the quark contribution can be neglected. Taking the LO result for

P_{qg},

$$P_{qg}(u) = 0.5\,\{(1-u)^2 + u^2\}, \qquad (7.4)$$

making the replacement $y = x/(1-z)$ and defining $G(x,Q^2) = x\,g(x,Q^2)$ leads to

$$dF_2/d\ln Q^2 \approx \sum_i e_i^2\, \alpha_s(Q^2)/(2\pi) \int_0^{1-x} dz\, P_{qg}(z)\, G(x/(1-z),Q^2). \qquad (7.5)$$

A Taylor expansion of $G(y,Q^2)$ is made around $z = 1/2$. Noting that P_{qg} is symmetric around $z = 1/2$ and that the second and higher derivatives of $G(y,Q^2)$ are small if $G(y,Q^2)$ is of the form $y^d(1-y)^a$, leads to the final result

$$dF_2/d\ln Q^2 \approx \sum_i e_i^2\, \alpha_s(Q^2)/(2\pi)\,(1/3)\, G(2x,Q^2)$$

$$G(2x,Q^2) \approx [27\pi/(10\,\alpha_s(Q^2))]\, dF_2(x,Q^2)/d\ln Q^2. \qquad (7.6)$$

ZEUS (1993 l) and H1 (1993h) analyzed their F_2 data according to (7.6) and obtained the results for $G(x,Q^2)$ shown in fig. 72. The data shown from ZEUS were obtained by recalculating them for $Q^2 = 20$ GeV^2 and $N_f = 4$, as used by H1. The two experiments agree rather well. Since for both experiments, the dominant error is the statistical one, combining the two measurements produces a ~ 30 - 40% measurement of G at small x. The data indicate that $G(x,Q^2)$ could be very large at small x.

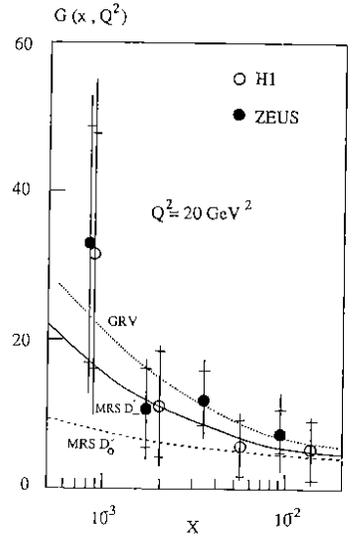

Fig. 72 The gluon distribution function $G(x,Q^2)$ for the proton at $Q^2 = 20$ GeV^2 as measured by H1 (1993h) and ZEUS (1993 l). The inner error bars are the statistical errors, the full have the systematic errors added in quadrature. The curves show different parametrizations or predictions for $G(x,Q^2)$: CTEQ (1993) and GRV (1993) are calculated in LO; the MRS curves are given in the DIS renormalization scheme.

In a recent paper R.K. Ellis, Kunszt and Levin (1993) presented a procedure for extracting $G(x,Q^2)$ from data on $F_2(x,Q^2)$ without neglecting the quark contribution and including terms up to third order in α_s.

7.3 The energy dependence of $\sigma(\gamma^*p)$

The F_2 data from H1 and ZEUS can be approximated by a function of the form $a(Q^2) + b(Q^2)\, x^{-1/2}$. Ignoring the logarithmic scaling violations (see above), a reasonable description is obtained with

$$F_2(x,Q^2) \approx 0.3\,(1 + 0.1\, x^{-1/2}) \qquad (7.7)$$

for the region $x = 4.10^{-4} - 1.10^{-2}$, $Q^2 = 10 - 40\ \mathrm{GeV}^2$. The $x^{-1/2}$ accounts for the rise of the structure function at small values of x (Lipatov term). Neglecting longitudinal contributions, this leads to the following expression for the total cross section of virtual transverse photon proton scattering (see eq. 5.12):

$$\sigma_{T\,tot}(\gamma^*p) \approx 4\pi^2\alpha/Q^2\ F_2(x,Q^2)/(1-x) \approx 4\pi^2\alpha/Q^2 \cdot [0.3\,(1 + 0.1\,W/Q)] \qquad (7.8)$$

For fixed Q^2, the total cross section has a term which is independent of the c.m. energy and a second piece, the Lipatov term, which rises with W. Using the optical theorem, Im $A(\gamma^*p) \sim \sigma_{T\,tot}(\gamma^*p)$, where A (γ^*p) is the invariant amplitude for forward elastic γ^*p scattering, one sees that at very high values of W and fixed Q^2 the elastic cross section will exceed the total one, $\sigma_{el}(\gamma^*p) > \sigma_{T\,tot}(\gamma^*p)$. The Lipatov term will violate unitarity unless it is damped at some $x < x_{crit}$ (see discussion in sect. 5.6).

Comparison with the data on $\sigma_{T\,tot}(\gamma p)$ for *real* photons at W = 18 and 200 GeV (see sect. 6) shows that in the *DIS data* at $Q^2 = 10\ \mathrm{GeV}^2$ the contribution from the W-dependent term is much larger than at $Q^2 = 0$ where

$$\sigma_{T\,tot}(\gamma p) \approx \text{const.}\,[1 + 0.001\,W].$$

8 Final states in DIS

In lowest order lepton - proton NC scattering, the transverse momentum of the scattered electron is balanced by a single jet associated with the struck quark, the proton remnant carrying relatively little transverse momentum. Higher order QCD processes modify this picture. In particular, a hard gluon can be radiated from the struck quark (QCD Compton scattering, QCDC), or a gluon from the proton can interact with the exchanged boson giving rise to quark - antiquark production (Boson Gluon Fusion, BGF), as illustrated in fig. 73.

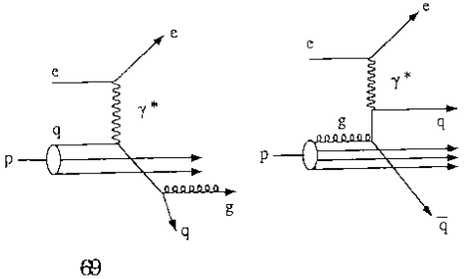

Fig. 73 Diagrams for QCDC and BGF

One consequence of these higher order processes is the broadening of the transverse momentum distribution of the particles with respect to the exchanged boson direction. This was observed e.g. by EMC (1981, 1987). The production of multi-jet events was reported in a fixed-target muon experiment at c.m. energies up to ~ 30 GeV (E665 1992). By virtue of the large photon proton c.m. energies, W, available at HERA the contributions from these higher order QCD diagrams become directly visible as multijet events. This was demonstrated by ZEUS and H1.

8.1 QCD models

For a quantitative comparison of the measurements with QCD predictions, models which describe the QCD processes at the parton level and the fragmentation into hadrons are indispensible. In general, the models are incorporated into Monte Carlo generators which include the simulation of the passage of final state particles through the detector. The features of models which are considered frequently by H1 and ZEUS are briefly summarized.

In LEPTO QCD processes are calculated up to $O(\alpha_s)$ according to exact first order matrix elements (ME). The QPM prediction is obtained by turning $O(\alpha_s)$ matrix elements off. Higher order contributions are simulated in the leading logarithm approximation (= parton shower approach, PS). The struck quark can emit partons either before or after the boson vertex (fig. 74). As the quark is radiating the initial state shower - before the boson vertex - it becomes more off-shell or virtual. After the interaction, the quark may again be off-mass shell and returns to the mass shell by radiating the final state shower. The amount of gluon radiation depends on the scale of virtuality which can be chosen to be either Q^2 or W^2 ($PS(Q^2)$ or $PS(W^2)$), or a function of both. Since $\langle Q^2\rangle$ is much smaller than $\langle W^2\rangle$ in the experiment, $PS(W^2)$ will predict much more gluon radiation than $PS(Q^2)$. The combination of the two approaches (ME + PS) gives the first order parton emission plus the higher order emissions through parton showers. The probabilities for all partonic subprocesses are matched to avoid double counting. The fragmentation into hadrons is performed with the Lund string model as implemented in JETSET (1986).

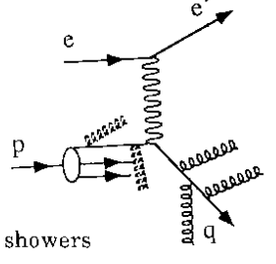

Fig. 74 Diagram with parton showers

In contrast to the bremsstrahlung-like parton shower model PS the color dipole model CDM does not distinguish between initial and final state radiation and includes interference effects between them. The struck parton and the proton remnant form a color dipole. When this dipole radiates a gluon, it splits into two radiating dipoles: one between the struck quark and the gluon and the other between the gluon and the remnant. Repeated gluon emission leads to a chain of such dipoles. Since one end of the dipole is considered nonpoint-like -

the proton remnant - the maximum p_T^2 in the hadronic c.m. for an emitted gluon varies as $W^{4/3}$. The simulation of QCDC for DIS is only approximate because of the extended proton remnant. CDM is implemented in ARIADNE (1992) which in turn is using LEPTO for generating the hard scattering.

The HERWIG (1992) generator does not consider explicitly the $O(\alpha_s)$ matrix elements. Rather, leading - log parton showers are considered. The parton shower takes place inside a cone of angular size set by the incoming and outgoing struck quark. In DIS this correlates the initial and final state parton showers. The characteristic scale is given by $2\ E^2\ (1 - \cos\psi)$ where E is the energy of the parton and ψ is the angle with respect to its color connected partner. The scale is essentially Q^2. It sets the upper limit for the shower evolution variables. Fragmentation into hadrons is modelled with a cluster fragmentation model.

8.2 Jet production

Jet production in DIS was analyzed by ZEUS (1993c) for an integrated luminosity of 27 nb^{-1}. Events were selected with $Q^2 > 4\ GeV^2$, $x \geq 10^{-4}$ and $30 < W < 280$ GeV, the average being 110 GeV. The transverse momentum distribution was determined in the γ^*p rest system with the help of condensates. Condensates are contiguous energy deposits in the calorimeter defined as follows: the calorimeter cell with the highest energy is used as the seed and the cells adjacent to the seed cell are merged. According to simulations, for polar angles above 9^0, the condensate multiplicity agrees with that of the final state particles to 90% and about 80% of the generated stable particles are associated with only one condensate. In the analysis condensates were treated as massless particles.

From the condensates the sphericity axis was determined in the γ^*p rest system. Figure 75 shows the distribution of the square of the transverse momentum, p_T^2, of the condensates w.r.t. the sphericity axis. The data were restricted to the hemisphere around the γ^* direction, which should contain the struck quark, and where one expects the gluon radiation effects to be most visible. The measured distribution is clearly much broader than the quark-parton model (QPM) expectations. The tail extends up to ~ 20 GeV^2 while the QPM predicts no events above 5 GeV^2.

A search was carried out for two or more jets (in addition to the proton remnant and excluding the scattered electron) in the HERA system. Jets were required to have a transverse energy > 4 GeV in a cone of radius $\Delta R = (\Delta\phi^2 + \Delta\eta^2)^{1/2} = 1$ and $\eta_{jet} < 2$. With this algorithm, 2502 (76%), 662 (20%), 95 (2.9%) and 15 (0.5%) events with zero, one, two or three jets were found. Examples of one -, two - and three - jet events are shown in fig. 76. Note that the jets are well isolated and their transverse energies are large, ranging from 5 to 30 GeV for the events shown.

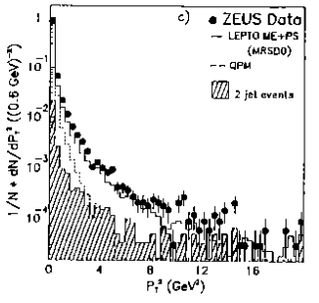

Fig. 75 Distribution of transverse momentum squared of condensates in the γ^*p c.m. system, measured w.r.t. the sphericity axis (ZEUS 1993c)

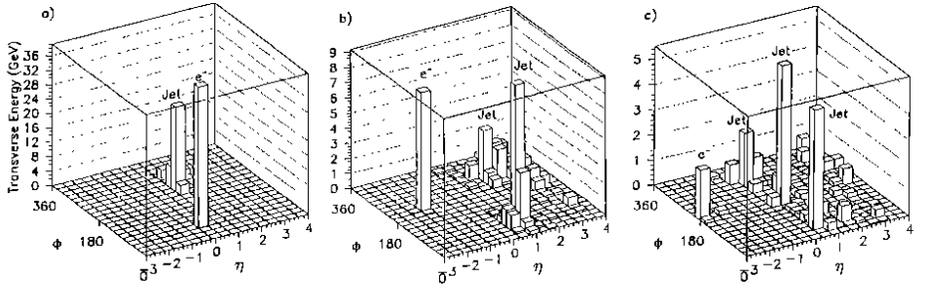

Fig. 76 Transverse energy distributions of events with jets in the (η, ϕ) plane: (a) one-jet event, (b) two-jet event, (c) three-jet event (ZEUS 1993c)

Two - jet events are candidates for the QCDC and BGF processes. The shaded area in fig. 75 shows the distribution for two - jet events. The $E_{T\,jet}$ distribution extends out to 22 GeV (fig. 77a, b). The pseudorapidity distribution rises towards large η values (fig. 77c). The two jets are preferably back-to-back in the plane transverse to the beams (fig. 77d). The jet energy profile, which is sensitive to fragmentation effects, is shown in fig. 78 where the transverse energy flow into cells within a cone radius of R = 2 around the jet axis was computed. The jet width is 0.5 - 0.6 (FWHM) in ϕ and η.

The data were compared with the expectations from QPM and QCD (figs. 75, 77, 78). The simple QPM fails to describe the data. First order QCD matrix elements plus parton showers (ME + PS) are in accord with the data: they reproduce the jet rates, describe the p_T^2 distributions as well as the jet E_T distribution and energy profile. It is noteworthy that the calculation based on exact first order matrix elements alone (ME), i.e. without parton showers, predicts a narrower jet profile than observed (fig. 78). The agreement with the QCD predictions suggests that two - jet production with large transverse jet energies is dominated by the QCD Compton and BGF processes.

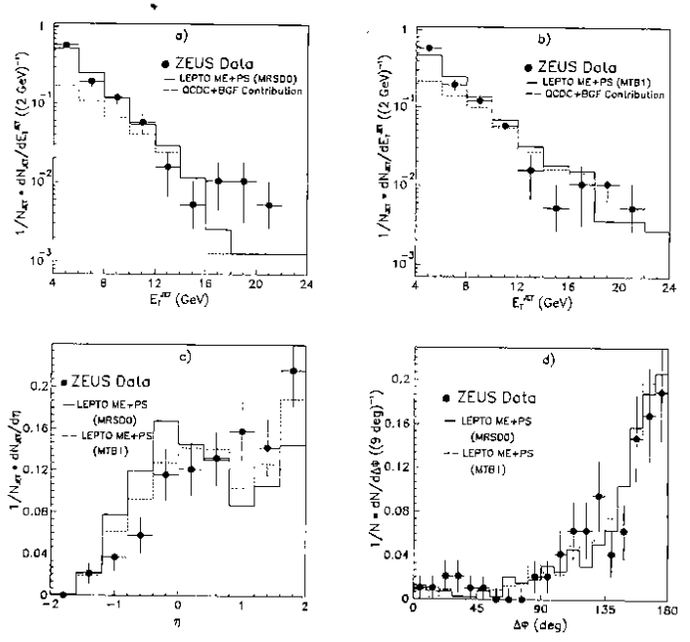

Fig. 77 Distributions of jets for two - jet events measured in the lab. frame w.r.t. the beam direction: (a), (b) transverse jet energy, (c) pseudorapidity and (d) azimuthal angular separation between the two jets (ZEUS 1993c)

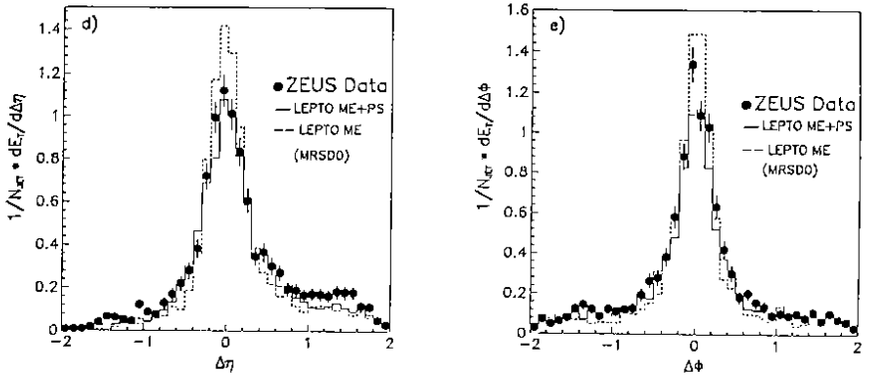

Fig. 78 The profile of jets belonging to the two-jet and three-jet samples (ZEUS 1993c)

8.2 Jet rates

H1 (1993g) studied the jet multiplicity in NC scattering as a function of the jet resolution with the goal to measure α_s. The event sample consisted of 769 (47) events with $12 < Q^2 < 80$ GeV^2 ($Q^2 > 100$ GeV^2) obtained from a luminosity of 22.5 nb^{-1}. Jets were selected with the JADE algorithm (JADE 1986). Two jets were considered to be resolved if their scaled invariant mass satisfied the condition:

$$y_{ij} = m_{ij}^2/W^2 > y_{cut} \qquad (8.1)$$

Here $m_{ij}^2 = 2 E_i E_j (1 - \cos\theta_{ij})$, E_i, E_j are the jet energies and θ_{ij} is the angle between them. Events with N jets in addition to a jet from the proton remnant (spectator jet) were classified as (N + 1) jet events. The lowest order configuration (QPM) with a current quark and a proton remnant in the final state is expected to produce preferentially (1 + 1) events; the first order QCD processes should yield predominantly (2 + 1) events. The fraction of (2 + 1) to (1 + 1) events should therefore be sensitive to the value of α_s.

Figure 79 shows the fractional jet rates for the (1 + 1), (2 + 1) and ($\geq$ 3 + 1) configurations as a function of y_{cut} for the low and high Q^2 samples. The data are uncorrected for acceptance and other detector effects. Note, that the data points are highly correlated since the same event sample is used for each value of y_{cut}.

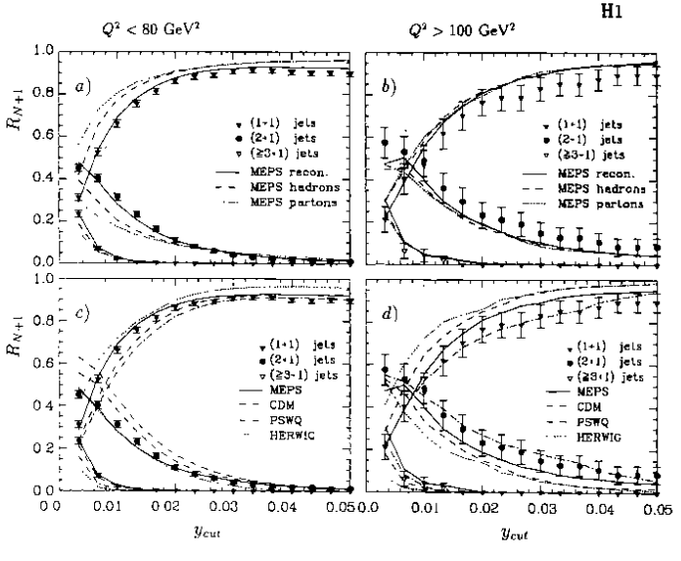

Fig. 79 Fraction of N + 1 jets (R_{N+1}) versus the cut variable of the jet algorithm for $12 < Q^2 < 80$ GeV^2 (a, c) and $Q^2 > 100$ GeV^2 (b, d), compared with simulations of ME + PS at the detector level and at the parton level, and in c, d) to predictions from QCD based models ME + PS, CDM, PS(W·Q) and HERWIG (H1 1993g)

For the test of QCD and the extraction of α_s the optimum value of y_{cut} is one where, firstly, the leading (LO) and all higher order QCD processes and, secondly, the transition from the parton to the hadron level give practically the same (2+1) fraction. Thirdly, the (2+1) fraction should not be too sensitive to detector smearing effects. The curves in fig. 79 show the predictions of various QCD models which were introduced above and which include hadronization and detector smearing; calculation of the hard scattering part is done in LO only. For the ME + PS model the differences between the predictions at the parton and hadron levels become small near $y_{cut} \approx 0.02$ (fig. 79a,c). Detector smearing has a 10 - 15% effect on the (2 + 1) fraction near this y_{cut} value. Of the various models studied ME + PS describes the data best (figs. 79 b,d).

The Q^2 dependence of the (2 + 1) fraction measured for $y_{cut} = 0.02$ is compared in fig. 80 with the predictions a) of ME + PS for a fixed $\alpha_s = 0.25$, and with a running α_s (with $\Lambda = 200$ MeV) for ME alone (b) and for ME + PS (c). The expected Q^2 behavior of α_s for a) and b) or c) is different. Because of the Q^2 dependence of α_s, the matrix element for jet production decreases with increasing Q^2. This decrease is not manifest directly in R_{2+1} because of the increase in phase space for jet production at larger Q^2 with the selection cuts applied. With higher statistics and good control of systematic effects from the detector and theory a test for a running α_s and a measurement of Λ may be feasible.

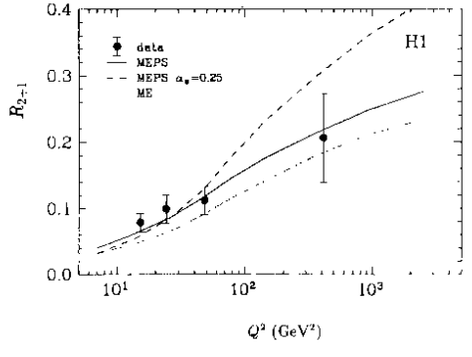

Fig. 80 (2 + 1) jet fraction R_{2+1} at $y_{cut} = 0.02$ versus Q^2, corrected for detector effects for $W^2 > 5000$ GeV^2 and $y < 0.5$, in comparison with the ME + PS model with a running α_s and a constant $\alpha_s = 0.25$, and also with the matrix elements with no showers (ME) (H1 1993g)

ZEUS (1993k) performed a similar study. The jet rates, corrected for detector effects and initial state QED radiation are shown in fig. 81. The correction factor proceeding from the detector level to the produced hadronic final state varies with y_{cut} between 5 and 20%. The difference between the hadron and the parton levels is below 10% for most of the region. ME + PS provides a good description for the (0, 1 + 1) and (2 + 1) rates. The conlcusion on the prospects for measuring α_s are the same as before.

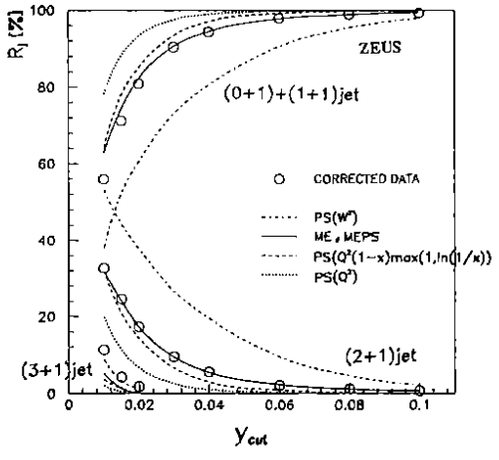

Fig. 81 Fraction of N + 1 jets (R_{N+1}), corrected for detector effects and initial state radiation, versus the cut variable of the jet algorithm for $x < 10^{-3}$ and $Q^2 > 10$ GeV^2. Predictions from QCD based models ME, PS, ME+PS are also shown (ZEUS 1993k)

8.3 Energy flow

In the quark parton model (QPM) the final hadronic state in DIS consists of a jet of particles originating from the struck quark representing the current jet and the particles produced by the proton remnant. Since the proton remnant is assumed to carry very little transverse momentum, the transverse momentum of the scattered electron is balanced by the current jet (fig. 82) . The direction γ_h of the current jet can be calculated from the energy and angle of the scattered electron (eq. 5.6). QCD introduces substantial corrections to this simple picture. The phase space between the current jet and the proton remnant is filled with particles materializing from the emission of additional gluons and quarks created by color transfer between the struck quark and the proton remnant.

The energy flow around the direction of the hypothetical struck quark was found to be very revealing when confronting these ideas with the data from ZEUS 1993e. The analysis was made with DIS events from a luminosity of 30 nb^{-1}. Figure 82 shows the energy flow as a function of the pseudorapidity calculated from the calorimeter cell energies relative to the direction of the struck quark,

$$\Delta\eta = \eta_{cell} - \eta_h$$

where $\eta_h = -\ln \tan(\gamma_h/2)$. The events were required to have $Q^2 > 10$ GeV^2 and $x < 10^{-3}$. Cells with $\theta < 10^0$ ($\eta_{cell} > 2.4$) were removed to reduce the influence of the proton remnant. Averaged over the event sample, the direction of the struck quark is $\gamma_h \approx 169^0$ or $\eta_h \approx -2.4$. In the QPM one expects the final state hadrons coming from the struck quark to concentrate around $\Delta\eta = 0$, and

those from the proton remnant at large positive $\Delta\eta$ (see sketch in fig. 82). The energy flow observed for the data shows several striking features. There are two peaks, one near $\Delta\eta = 0$, the other one at large $\Delta\eta$ values. The peak at low $\Delta\eta$ values is shifted from the expectation of the QPM by about 0.5 rapidity units in the positive direction to $\Delta\eta \approx +0.5$. Furthermore, almost all energy appears at positive $\Delta\eta$ values, between the direction of γ_h and the proton remnant.

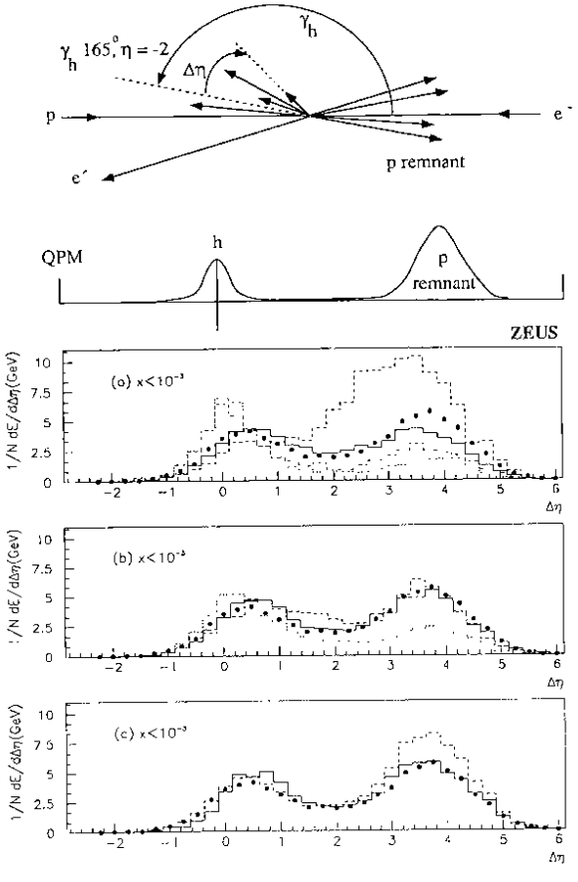

Fig. 82 Deep inelastic neutral current scattering at $x < 10^{-3}$, $Q^2 > 10$ GeV^2: the energy weighted pseudorapidity difference, $\Delta\eta$, measured with the calorimeter w.r.t. the struck quark from the quark-parton model (see sketch on top). The data (dots) are compared with QCD models: (a) ME +PS (full histogram), ME (dashed-dotted), PS(W^2) (dashed), PS(Q^2) (dotted); (b) CDM + BGF (full), CDM (dashed), PS(Q^2(1 - x)) (dotted); (c) HERWIG (full) without soft underlying events (SUE) and including SUE (dashed); from ZEUS (1993e)

Qualitatively, a continuous color flow producing a continuous energy flow between the struck quark direction and the proton remnant at these low-x values (i.e. high W values) is expected from QCD radiation when averaging over many events. Also, if the struck quark radiates a gluon in the final state the intermediate quark has a nonzero positive mass. Therefore, the momentum fraction of the proton carried by the struck quark is *larger* than x, calculated from the electron side (eq. 5.9), causing a shift towards *positive* $\Delta\eta$ values for the energy flow from the struck quark. Furthermore, initial state radiation will emit particles close to the proton direction and will therefore add to the energy flow in this region. Several QCD models, ME + PS, CDM+ BGF (i.e. adding the matrix element for BGF in the calculation) and HERWIG, are found to give a quantitative description of the data.

9 Production of events with large rapidity gaps

The standard DIS events (see fig. 83) show energy deposition in the forward region, presumably coming from the fragmentation of the proton remnant, from initial state QCD radiation or from fragmentation of the struck quark. ZEUS (1993g) has observed a class of events which have different characteristics. In fig. 84 one of such events is displayed. It shows a well identified electron from which a Q^2 value 64 GeV^2 is inferred. The special feature of the event is the absence of enegry deposition in the forward direction: the first significant deposition of energy is found at $\theta > 90^o$. The presence of this new type of events in DIS was confirmed by H1 (1993j,k).

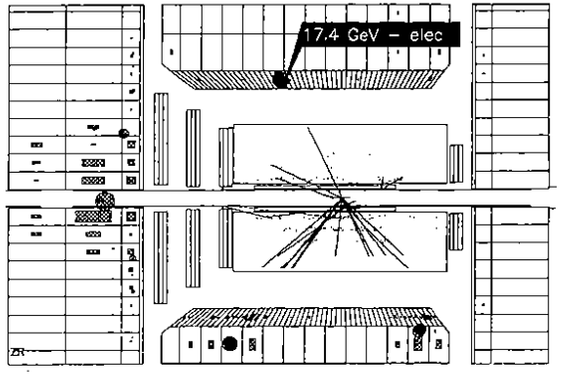

Fig. 83 Typical event of standard deep inelastic neutral scattering with 34 GeV observed in the forward calorimeter (FCAL) (from ZEUS)

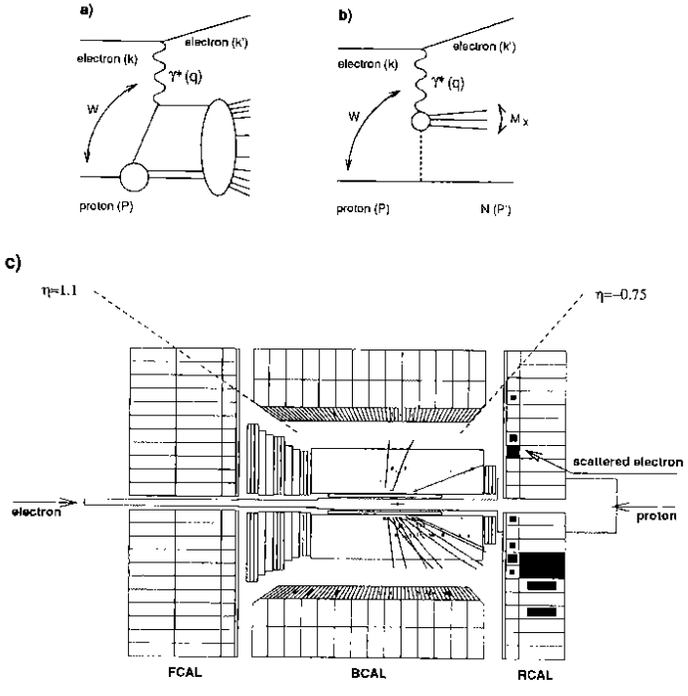

Fig. 84 (a) Schematic diagram describing particle production in DIS;
(b) same for diffractive dissociation in DIS. W is the c.m. energy of the γ^*p system and M_x the invariant mass of the hadronic system measured in the detector. N represents a proton or a low-mass nucleon system.
(c) A DIS event at $Q^2 = 64$ GeV^2 with a large rapidity gap in the ZEUS detector

9.1 Experimental results

In the ZEUS analysis (1993g) the effect was quantified by considering all DIS events (total luminosity 24.7 nb^{-1}) with $Q^2 > 10$ GeV^2. A calorimeter cluster was defined as an isolated set of adjacent cells with summed energy above 400 MeV. The pseudorapidity of the cluster closest to the forward direction, i.e. with the largest η value, was called η_{max}. The distribution of η_{max} for all DIS events (fig. 85a) shows two groups of events, one concentrated at large η_{max} values and a second one with $\eta_{max} < 2$. The standard Monte Carlo simulation for DIS scattering (e.g. CDM) predicts the shaded distribution which does not account at all for the number of events observed with $\eta_{max} < 2$. Figure 85b shows that for these events W and η are correlated, which is not observed for the bulk of the events.

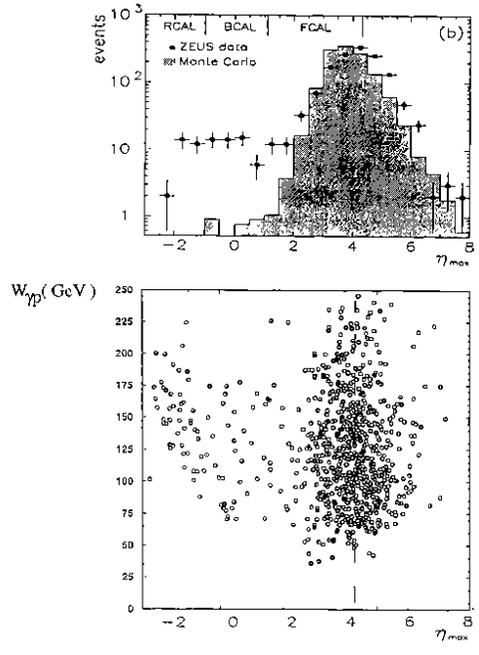

Fig. 85 (a) Distribution for DIS events of the maximum rapidity η_{max} of a calorimeter cluster in an event, for data (points) and Monte Carlo events (shaded histogram)
(b) Correlation between the γ^*p c.m. energy W and η_{max} (from ZEUS 1993g,j,l)

For the further study, events with $\eta_{max} < 1.5$ were denoted as events with a large rapidity gap. An η_{max} of 1.5 corresponds to a rapidity gap of at least 2.8 units. The mass M_x of the hadronic system was calculated from the energies detected in the calorimeter cells. Denote by E_H, p_H and θ_H the energy, momentum and angle of the hadronic system. By comparing with sect. 5.1 one finds:

$$\begin{aligned} \cos\theta_H &= \Sigma_h p_{zh} / | \Sigma_h p_h | \\ E_H - p_H \cos\theta_H &= 2 E_e y_{DA} \\ p_H^2 \sin^2\theta_H &= Q_{DA}^2 (1 - y_{DA}) \\ M_x &= [E_H^2 - p_H^2]^{1/2} \end{aligned} \qquad (9.1)$$

Large rapidity gap events have preferentially small M_X values with typical values around 10 GeV in distinction to the events with $\eta_{max} > 1.5$ (fig. 86a). The M_X^2 distribution falls off rapidly, $dN/dM_X^2 \sim (M_X)^{-n}$, $n \approx 2 - 4$, as shown in fig. 87. For W > 150 GeV, acceptance corrections have little dependence on W. For W > 150 GeV the contribution of large rapidity gap events to the total DIS cross section is, within errors, constant with W (fig. 86b). The contribution of the large rapidity gap events to the DIS cross section as a function of Q^2 is, within errors, also constant with Q^2 (fig. 88). It is worth noting that the data reach Q^2 values as high as 100 GeV^2. The events with $\eta_{max} < 1.5$ represent 5.4% of the total DIS events.

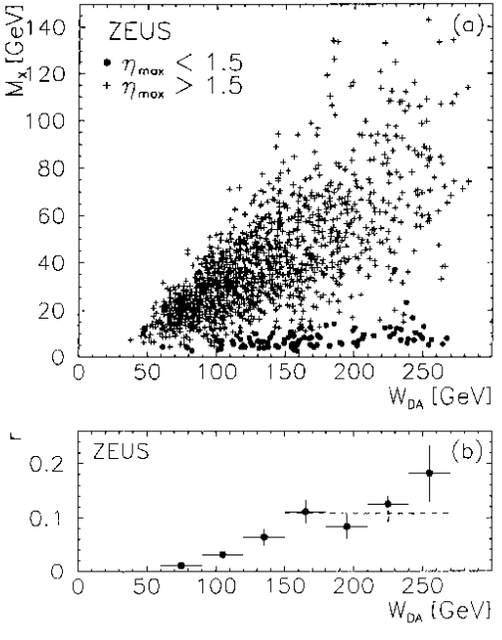

Fig. 86 (a) Correlation between M_X and W for events with $\eta_{max} > 1.5$ (crosses) and $\eta_{max} < 1.5$ (dots);
(b) Fraction of DIS events r with $\eta_{max} < 1.5$ as function of W from ZEUS (1993g)

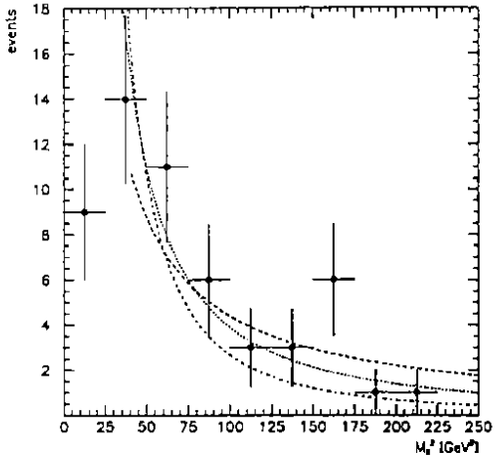

Fig. 87 Distribution (uncorrected) of M_X^2 for events with $\eta_{max} < 1.5$ and W > 150 GeV; the dashed line shows a $1/M_X^2$ dependence, the dotted line - $1/M_X^3$, the dashed-dotted - $1/M_X^4$; from ZEUS (1993j,l)

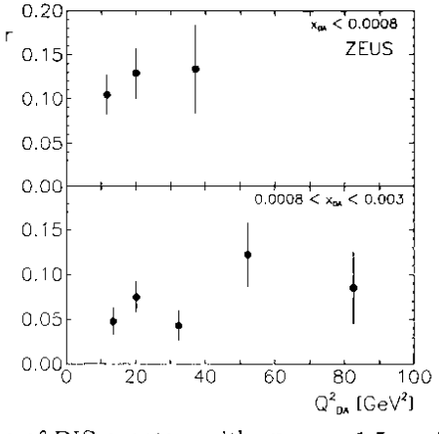

Fig. 88 Fraction of DIS events r with $\eta_{max} < 1.5$ as function of Q^2 for two x intervals (ZEUS 1993g)

The H1 findings for large rapidity gap events in DIS are shown in fig. 89. The maximum η value (η_{max}) for clusters measured in the calorimeter is 3.8. The distribution of the difference in pseudorapidity between this value and the closest cluster with > 400 MeV in an event, $\Delta\eta = 3.8 - \eta_{max}$, is given in fig. 89a. A steep fall-off from zero up to $\Delta\eta \approx 1.4$ is followed by a long tail extending up to $\Delta\eta \approx 6$. Large rapidity gap events are defined to have $\Delta\eta > 2$ ($\eta_{max} < 1.8$); 6% of the DIS events are found to have such a rapidity gap, while a Monte Carlo simulation with LEPTO, which reproduces well the fall-off in the region of small $\Delta\eta$, predicts only 0.1% (see histogram in fig. 89a). The distribution of M_X

(fig. 88b) shows that small M_X values are preferred; note, that the distribution is uncorrected and detector acceptance is particularly important for $M_X < 4$ GeV. The ratio of events with a large rapidity gap to all events does not depend significantly on Q^2 as shown in fig. 89c.

The results obtained by the two experiments on large rapidity gap events in DIS are in good agreement. What is the origin of these events? The behavior of the energy flow in the bulk of DIS events (previous section) suggests to attribute the absence of energy flow over a large rapidity range to missing color flow. The near constancy of the percentage of large rapidity gap events with Q^2 points to a leading twist contribution to the proton structure function or, in other words, since the structure function F_2 shows only logarithmic scaling violations the process leading to large rapidity gap events appears to behave in the same way.

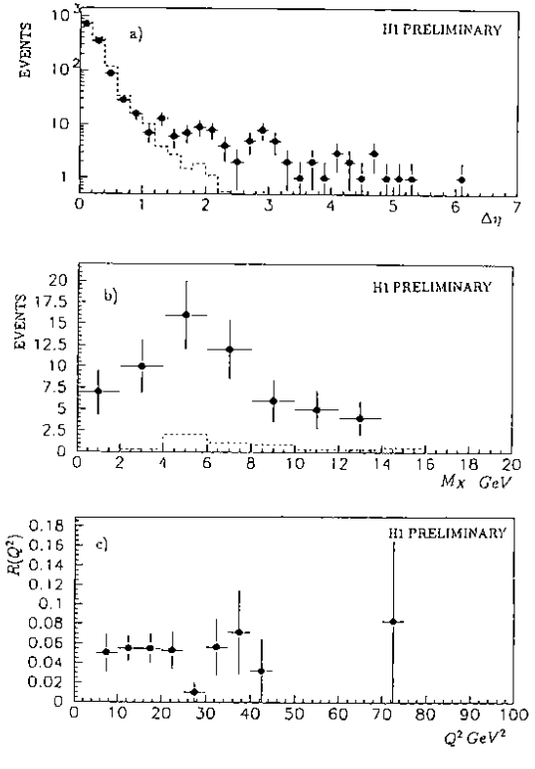

Fig. 89 (a) Distribution of the rapidity gap $\Delta\eta$ for DIS events
(b) Effective mass of the visible hadronic system of events with $\Delta\eta > 2$
(c) Ratio $R(Q^2)$ of events with a rapidity gap $\Delta\eta > 2$ over all DIS events as function of Q^2 (H1 1993j,k)

9.2 Large rapidity gaps by peripheral scattering

In soft processes large rapidity gaps can be produced by peripheral scattering of hadrons. Consider two-body scattering a + b -> c + d sketched in fig. 90 in the c.m. system. The square of the four - momentum transfer at particle momenta p_a, p_b,.. large compared to their masses m_a, m_b, .. can be approximated by

$$t = (a - c)^2 \approx - 2 p_a p_c (1 - \cos\theta) \qquad (9.1)$$

where θ is the scattering angle. Peripheral processes are characterized by small $|t|$ values with negligible cross section for, say, $|t|_{max} > 1$ GeV^2. For $2p_ap_c \gg |t|_{max}$ this limits the scattering to small angles,

$$\cos\theta > 1 - |t|_{max} / (2 p_a p_c) \qquad (9.2)$$

and the rapidities Y of c and d to very large (small) values (see eq. 6.8):

$$Y_c \approx 0.5 \ln \{ [p_c (1 + \cos\theta)] / [p_c (1 - \cos\theta) + m_c^2/(2 p_c)] \}$$
$$> 0.5 \ln \{ 4 p_c^2 / [m_c^2 + |t|_{max} (p_c/p_a)] \} \qquad (9.3)$$

The maximum (minimum) rapidities are

$$Y_c^{max} \approx \ln 2 p_c/m_c \approx 0.5 \ln s/m_c^2$$
$$Y_d^{min} \approx - \ln 2 p_d/m_d \approx - 0.5 \ln s/m_d^2 \qquad (9.4)$$

where s is the square of the c.m. energy. The minimum rapidity gap between c and d is (fig. 90b):

$$\Delta Y > 0.5 [\ln s/(m_c^2 + |t|_{max}) + \ln s/(m_d^2 + |t|_{max})]. \qquad (9.5)$$

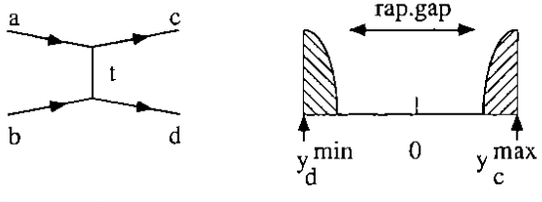

Fig. 90 (a) Diagram for a + b -> c + d; (b) rapidity distributions of c, d

For the example of $\sqrt{s}$ = 200 GeV, c being a proton, d having a mass of 5 GeV and $|t|_{max}$ = 1 GeV^2 the rapidity gap between c and d is $\Delta Y \approx 9$. Suppose d decays into pions. Then for a standard pion multiplicity the pions populate rapidities around the center value Y_d with an rms spread of about $\pm$ (1 - 2) units. The resulting rapidity gap between the proton and the pions from d is 6 to 7 units large. *Peripherality and a c.m. energy which is large compared to the particle masses produce a large rapidity gap.*

For the case that a + b -> c + d proceeds via the exchange of a Regge pole R, the energy dependence of the cross section is given by:

$$d\sigma/dt \approx f(t)\, s^{2\alpha_R(t) - 2} \qquad (9.6)$$

Here $\alpha_R(t)$ is the trajectory for R, $\alpha_R(t) \approx \alpha_R(0) + \alpha' t$, $\alpha' \approx 1$ GeV^{-2}. For the pion trajectory the intercept $\alpha_\pi(0) \approx 0$; for the rho trajectory $\alpha_\rho(0) \approx 0.5$. The resulting energy dependence of the forward cross section is

$d\sigma/dt\,(t = 0) \sim s^{-2}$ for π exchange

$\sim s^{-1}$ for rho exchange.

The implication is that cross sections for peripheral processes of this type, which are characterized by the exchange of quantum numbers in the t channel (e.g. isospin, charge, ..), decrease very fast with s.

There exists a special class of peripheral processes due to diffractive scattering where no quantum numbers are exchanged and which show (almost) energy independent cross sections (for a review of experimental data see e.g. Goulianos 1983, 1990). They are described by the Regge trajectory of a hypothetical particle, the pomeron,

$$\alpha_P(t) \approx 1 + 0.5\, t$$

which leads to $d\sigma/dt\,(t = 0) = \text{const}$ as a function of s. Therefore, of the possible Regge exchanges, only pomeron exchange has a chance to survive with a significant cross section at high c.m. energies.

9.2 Discussion

The large rapidity gap events observed by ZEUS and H1 in DIS are produced at high γ^*p c.m. energies (W's up to 270 GeV) with large rates (5 - 20 % of the total DIS events). It is therefore suggestive to attribute them to pomeron exchange (fig. 91a). One must keep in mind, however, that in general diffractive production has been studied in *soft* processes. The large rapidity gap events observed by ZEUS in photoproduction (sect. 6.3) are an example of this. In contrast, the events under discussion here from DIS are produced by *hard* scattering at Q^2 values above 10 GeV^2 and up to 100 GeV^2. The low - x data on the proton structure function F_2 indicate two pieces which build up the total virtual photon proton cross section at large Q^2, one which is independent of the total c.m. energy W, and one whose contribution increases with energy. It is suggestive to associate the constant piece with the soft pomeron and the energy dependent component (Lipatov term) with a hard pomeron.

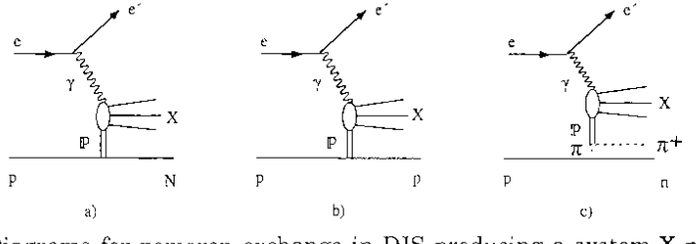

Fig. 91 Diagrams for pomeron exchange in DIS producing a system X plus (a) a nucleon state N, (b) a proton, (c) a neutron plus a mesonic state m via pion exchange, where m is a pion or a higher mass state

The concept of the pomeron structure function was studied in terms of perturbative QCD (Gribov, Levin and Ryskin 1983, Berger et al. 1987, Bartels and Ingelman 1990, Ryskin 1991, Levin and Wüsthoff 1992, Nikolaev and Zakharov 1992, Ingelman and Pryrtz 1993, Collins, Frankfurt and Strikman 1993). It was suggested that the pomeron structure could be probed with a virtual photon at HERA (Ingelman and Schlein 1985, Donnachie and Landshoff 1987, 1992, Streng 1987). Rapidity gaps as a means for detecting new physics were discussed by Bjorken (1992).

On the basis of pp data from R608 (1985) taken at the CERN ISR Ingelman and Schlein (1985) suggested that the pomeron may have a partonic structure. Proton - proton collider data from the UA8 collaboration (1988, 1992) gave strong evidence for high transverse momentum jets in diffractively produced high mass systems suggestive of the hard scattering from partons within the pomeron. Observation of events with large rapidity gaps by $p\bar{p}$ collisions were reported recently also by D0 (Forden 1993). A new study from UA8 (UA8 1993, Schlein 1993) suggests that the pomeron may have a superhard part with one parton carrying almost all of the pomeron momentum in a significant fraction of the events.

Deep inelastic electron proton scattering is well placed for unravelling the properties of the pomeron. By keeping Q^2 fixed and varying x the relative contributions from the conjectured soft and hard pomerons can be changed. The analysis of the (jet) structure of the system X will tell us more about the partonic structure of the pomeron. Important information can also be gained from an analysis of the produced nucleon system N (fig. 91a). For a fraction of the events one expects N to be just a proton (fig. 91b). The momentum of this proton (p_f) will be almost equal to the momentum of the incoming proton (p_{beam}),

$$x_{pom} = [p_{beam} - p_f] / p_{beam} \approx [M_x^2 + Q^2] / [W^2 + Q^2] \sim O(10^{-2}) \qquad (9.7)$$

where x_{pom} is the momentum fraction of the proton carried by the pomeron. Such protons can be detected in the Leading Proton Spectrometer (LPS) of the ZEUS detector (sect. 3.2). Information from the LPS will provide another signature for diffractive events.

Pomeron exchange can also occur as part of a multiperipheral process such as depicted in fig. 91c where the incoming proton emits a virtual pion which scatters on the pomeron emitted at the photon vertex. The contribution of a pomeron - pion ladder to inelastic diffractive ρ^0 production by real photon proton scattering was predicted to increase with photon energy E_γ and to be substantial at high energies (Wolf 1971). The cross section was calculated for $\gamma p \to \rho^0 N + i\pi$, $i \geq 1$, taking into account the diagrams of fig 92. The result is shown in fig. 93 as a function of the photon energy, E_γ, assuming a stationary proton: at E_γ = 300 GeV (W = 24 GeV) the cross section amounts to about 5μb which is ~ 50% of the elastic ρ^0 cross section.

A subprocess of inelastic diffractive scattering is e p -> e X n π^+ where X results from diffraction dissociation of the virtual photon (analoguously to fig. 92b). In this case the neutron n carries almost the full momentum of the beam proton and can be tagged with a calorimeter close to the proton beam as pointed out by Levman and Furutani (1992). During the 1993 running ZEUS had a prototype of a Forward Neutron Calorimeter (FNC) installed and found that detection of these neutrons is feasible. A full FNC will complement the LPS

information from protons on diffractive production.

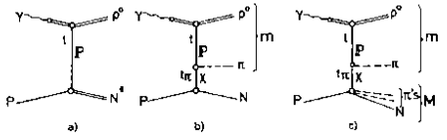

Fig. 92 Diagrams for inelastic diffractive ρ^0 photoproduction: (a) isobar production by pomeron exchange; (b) and (c) double peripheral scattering with pomeron and pion exchange

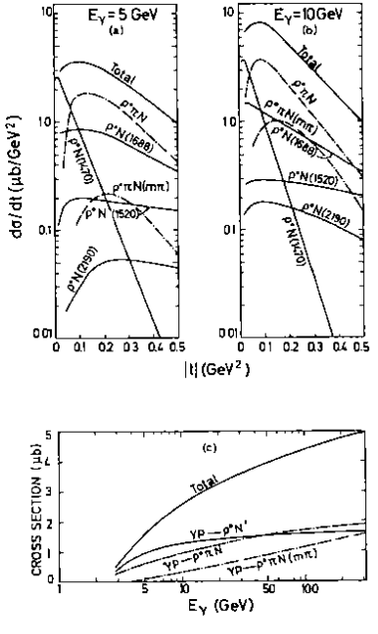

Fig. 93 Cross sections for inelastic diffractive ρ^0 photoproduction via isobar production (diagram (a) of fig 92) and double peripheral scattering (diagrams (b) and (c) of fig. 92). The curves labelled 'total' show the incoherent sum of all contributions (from Wolf 1971)

10 Concluding remarks

The experimental results presented in this report were extracted from data obtained by H1 and ZEUS during the 1992 running. The 1993 data which are currently under study represent a twentyfold increase in luminosity and promise a wealth of new information. They will allow, for instance, to increase the Q^2 range in NC scattering by an order of magnitude and to make a first study of CC scattering at large Q^2. The search for exotic particles such as leptoquarks and excited leptons and quarks will also benefit from the increased statistics. The results reported from the 1992 data (H1 1993c, ZEUS 1993d) for some species have already exceeded the sensitivity of previous searches. Running in 1994 will presumably lead to a further tenfold increase in luminosity. The large growth in event statistics will help to perform the studies discussed here with much improved precision and will bring many more channels in the reach of the two experiments.

11 Acknowledgements

Prof. D. Saxon as director and Drs. A.T. Doyle, P. Negus, K. J. Peach L. Vick and A. Walker as organisers have provided a most stimulating and enjoyable atmosphere for the participants of the school. I am grateful to Prof. J. Bartels for discussions and to Prof. W. Buchmüller, Dr. R. Klanner, Profs. E. Lohrmann and J. Whitmore for a critical reading of the manuscript and for many comments. S. Gharavi has prepared diagrams and figures. I want to thank Mrs. I. Harm for her help with the manuscript.

References

In the following "HERA Workshop 1991" stands for Physics at HERA, Proc . Workshop 1991, ed. by W. Buchmüller and G. Ingelman, April 1992.

Abramowicz, H, Charchula, K and Levy, A, 1991, Phys. Lett. **B269** 458.
Abramowicz, H et al., 1991, Phys. Lett. **B269** 465.
Alekhin, S I et al , 1987, CERN - HERA 87-01 and references given there.
Altarelli, G and Parisi, G, 1977, Nucl. Phys. **126** 297.
AMY collaboration, Tanaka, R et al., 1992, Phys. Lett. **B277** 215.
AMY collaboration, Kim, B J et al., 1993, KEK preprint 93 - 97.
ARIADNE, Lönnblad, L, 1992, Comp. Phys. Com. **71** 15, and references given there.
Balitskii, Y Y and Lipatov, L N, 1978, Sov. J. Nucl. Phys. **28** 822.
Barber , D B et al., 1992, DESY Report 92 - 136; 1993 private communication by Zetsche, F.
Barger, V D and Phillips, R J N, 1987, Collider Physics, Frontier in Physics Series (Vol. 71), Addison - Wesley.
Bartels, J and Ingelman, G, 1990, Phys. Lett. **B235** 175.
BCDMS collaboration, Benvenuti, A C et al., 1989, Phys. Lett. **B223** 485.
Bentvelsen, S, Engelen, J and Kooijman, P, HERA Workshop 1991, Vol. 1, p.23.
Berger, E et al., 1987, Nucl. Phys. **B286** 704.
Bjorken, J D, 1969, Phys. Rev. **179** 1547.
Bödeker, D, 1992, Phys. Lett. **B292** 164.
Borzumati, F M, Kniehl, B A and Kramer, G, 1993, Z. Phys. **C59** 341.
Buchmüller, W and Ingelman, G, 1991, Proc. Workshop: Physics at HERA, April 1992, ed. by W. Buchmüller and G. Ingelman, DESY, Hamburg.
Buon, J and Steffen, K, 1985, DESY report 85 - 128.
Burow, B 1993, thesis Univ. Toronto.
CTEQ collaboration, Brock, R et al., 1993, Handbook of Perturbative QCD.
Chacaltaya and Pamir collaborations, 1990, contrib. VI Int. Symp. on V. H. E. Cosmic Ray Interactions, ICRR-Rpt-216-90-9.
Chang, C et al., 1975, Phys. Rev. Lett. **35** 901.
Chaves, H, Seifert, R J and Zech, G, 1991, HERA Workshop 1991, Vol. 1, p. 57.
Collins, J C, Frankfurt, L and Strikman, M, 1993, Phys. Lett. **B307** 161.
Cooper-Sarkar, A M et al., 1988, Z. Phys. **C39** 281.
D0 collaboration, Forden, G, 1993, 28th Renc. Moriond, Les Arcs, Savoie, 1993.
Donnachie, A and Landshoff, P V, 1984, Nucl. Phys. **B244** 322.
Donnachie, A and Landshoff, P V, 1987, Phys. Lett. **B191** 309; 1992, ibid. **B285** 172.
Donnachie, A and Landshoff, P V, 1994, Z. Phys. **C61** 139.
Dokshitzer, Y L, 1977, Sov. Phys. JETP **46** 641.
Drees, M and Grassie, K, 1985, Z. Phys. **C28** 451.
Drees, M and Godbole, R M, 1992, Bombay Univ. Report BU-TH 92-5.
E1665 collaboration, 1992, Adams, M R et al., 1992, Phys. Rev. Lett. **69** 1026.
Eichten, E et al., 1984, Rev. Mod. Phys. **56** 579; 1986, ibid. **58** 1047.
Ellis, R K, Kunszt, Z and Levin, E M, 1993, Fermilab-PUB-93/350-T, ETH-TH/93/41
EMC collaboration, Aubert, J J et al., 1981, Phys. Lett. **B100** 433; Arneodo, M et al., 1987, Z. Phys. **C36** 527.
Feynman, R P, 1972, Photon-Hadron Interactions, Reading, Mass., Benjamin.
Fletcher, R S et al., 1992, Phys. Rev. **D45** 377.
Forshaw, J R and Storrow, J K 1991, Phys. Lett. **B268** 116
Forshaw, J R, 1992, RAL 92-073.
Fox, D J et al., 1974, Phys. Rev. Lett. 41 1504.
Fritzsch, H and Gell-Mann, M, 1972, Proc. 16th Int. Conf. High Energy Physics, Chicago, Vol. 2, p. 135, Batavia, Ill., Fermi Nat. Accel. Lab.

Fritzsch, H, Gell-Mann, M and Leutwyler, H, 1973, Phys. Lett. **47** 365.
Ghandi, R and Sarcevic, I, 1991, Phys. Rev. **D44** R10.
Glück, M, Reya, E and Vogt, A, 1990, Z. Phys. **C48** 471.
Glück, M, Reya, E and Vogt, A, 1992, Z. Phys. **C53** 127.
Glück, M, Reya, E and Vogt, A, 1993, Phys. Lett. **B306** 391.
Gordon, L E and Storrow, J K, 1992**a**, Phys. Lett. **B291** 320; 1992**b**, Z. Phys. **C56** 307.
Greco, M and Vicini, A, 1993, Frascati LNF-93/017.
Gribov, V N and Lipatov, L N, 1972, Sov. J. Nucl. Phys. **15** 438, 675.
Gribov, L V, Levin, E M and Ryskin, M G, 1983. Phys. Rep. **100** 1.
Goulianos, K, 1983, Phys. Rep. **101** 169,; 1990, Nucl. Phys. B, Proc. Suppl. **12** 110.
Gross, D J and Wilczek, F, 1973, Phys. Rev. Lett. **30** 1343, Phys. Rev. **D 8 3663; 1974**, Phys. Rev. **D 9** 980.
H1 Collaboration, 1986, Technical Proposal for the H1 Detector.
H1 collaboration, Ahmed, T et al., 1992, Phys. Lett. **B297** 205.
H1 collaboration, Ahmed, T et al., 1993**a**, Phys. Lett. **B298** 469; 1993**b**, Phys. Lett. **B299** 374.
H1 collaboration, Abt, I et al.,1993**c**, Nucl. Phys. **B396** 3; 1993**d**, DESY 93 - 103; 1993**e**, Phys. Lett. **B314** 436; 1993**f**, Nucl. Phys. **B407** 515; 1993**g**, DESY 93 - 137; 1993**h**, DESY 93 -146.
H1 collaboration, De Roeck, A and Klein, M, 1993**i**, DESY 93-014.
H1 collaboration, De Roeck, A, 1993**j**, 1993 EPS Conf. Marseille, DESY 94-005; Dainton, J 1993**k**, 1993 Lepton-Photon Conference at Cornell.
HERA, A Proposal for a Large Electron - Proton Colliding Beam Facility at DESY, DESY HERA 81 -10 (1981).
HERA-B collaboration, 1992, Experiment to Study CP Violation in the B System Using an Internal Target at the HERA Proton Ring.
HERACLES, Kwiatkowski, A, Spiesberger, H and Möhring, H-J, 1992, Comp. Phys. Com. **69** 155, and references given there.
HERMES collaboration, 1990, Proposal to Measure the Spin-Dependent Structure Functions of the Neutron and the Proton at HERA.
HERWIG, Webber, B R, 1986, Ann. Rev. Nucl. Part. Sci. **36** 253; and Marchesini, G et al. 1992, Comp. Phys. Comm. **67** 465.
Huth, J et al., 1990, Proc. 1990 DPF Summers Study on High Energy Physics, Snowmass, Colorado, ed. Berger, E L, (World Scientific, Singapore, 1992) p. 134.
Ingelman, G and Schlein, P, 1985, Phys. Lett. **B152** 256.
Ingelman,G and Rückl, R, 1987, DESY Report 87 - 140; 1988, Phys. Lett. **201** 369.
Ingelman, G and Prytz, K, 1993, Z. Phys. **C58** 285.
Jacquet, F and Blondel, A, 1979, Proc. Study of an ep Facility in Europe, ed. U. Amaldi, 79/48, p. 391.
JADE collaboration, W. Bartel et al., 1981, Phys. Lett. **107B** 163.
JADE collaboration, Bartel, W et al., 1986, Z. Phys. **C33** 23.
Janssens, T, Hofstadter, R et al., 1966, Phys. Rev. **142** 922.
JETSET, Sjöstrand, T 1986, Comp. Phys. Com. **39** 347; Sjöstrand, T and Bengtsson, M 1987, ibid **43** 367 (1987) and CERN-TH 6488/92 (1992).
Kim, V T and Ryskin, M G, 1991, DESY 91 - 064.
Kolanoski, H 1984, Two - Photon Physics at e^+e^- Storage Rings, Springer Tracts in Modern Physics 105.
Kramer G and Salesch, S G, 1993, DESY 93-10.
Kuraev, E A, Lipatov, L N and Fadin, V S, 1977, Sov. Phys. JETP **45** 199.
Kwiecinski, J et al., 1990, Phys. Rev. **D42** 3645.
Kwiecinski, J, 1993, Lecture Notes in Physics, Substructure of Matter as Revealed with Electroweak Probes, Proc. Schladming, 1993, ed. by L. Mathelitsch and W. Plessas, Springer Verlag 1994, p. 215.
LEPTO, Ingelman, G, LEPTO5.2, program manual, unpublished; Bengtsson, H, Ingelman, G and Sjöstrand, T, 1988, Nucl. Phys. **B301** 554.
Levin, E M and Wüsthoff, M, 1992, DESY 92-166 and FERMILAB-PUB-92/334.
Levman, G and Furutani, K 1992, ZEUS internal note, unpublished.
Levy, A, 1992, Photoproduction at HERA, DESY Acad. Training Progr., 27 - 29/4/1992,

unpublished.
Lipatov, L N, 1974, Sov. J. Nucl. Phys. **20** 181.
Lipatov, L N, 1976, Sov. J. Nucl. Phys. **23** 338.
Martin, A D, Stirling, W J and Roberts, R G, 1993, Phys. Rev. **D47** 867.
Martin, A D, Stirling, W J and Roberts, R G, 1993, Phys. Lett. **B306** 145.
Martin, A D, Stirling, W J and Roberts, R G, 1993, RAL 93-77/DTP 93/86.
Milsztajn, A and Virchaux, M, 1993, Lecture Notes in Physics, Substructure of Matter as Revealed with Electroweak Probes, Proc. Schladming, 1993, ed. by L. Mathelitsch and W. Plessas, Springer Verlag 1994, p. 257.
Morfin, J G and Tung, W K, 1991, Z. Phys. **C52** 13.
Mueller, A H, 1990, Proc. Small x - Workshop at DESY, 1990, ed. by A. Ali and J. Bartels, 1991, Nucl. Phys. **18C** 125.
Nikolaev, N N and Zakharov, B G, 1992, Z. Phys. **C53** 331, and 1993, LANDAU 16 - 93.
NMC collaboration, Amaudruz et al., 1992, Phys. Lett. **B295** 159.
OMEGA- Photon collaboration, Apsimon, R J et al., 1989, Z. Phys. **C43** 63.
Parisi, G and Petronzio, R, 1976, Phys. Lett. **B62** 331.
Peccei, R, Proc. HERA Workshop 1987, ed. by R. Peccei, August 1988. DESY, Hamburg.
PDG Particle Data Group, Physical Review **D45** (1992).
PLUTO collaboration, Berger, Ch et al., 1984, Z. Phys. **C26** 191.
Prytz, K, 1993, Phys. Lett. **B311** 286.
PYTHIA Bengtsson H-U and Sjöstrand, T, 1987, Comp. Phys. Com. **46** 43; Sjöstrand, T, 1989, Z. Phys. **C42** 301.
R608 collaboration, Smith, A M et al., 1985, Phys. Lett. **B163** 267; 1986, ibid. **B167** 248; Henkes, T et al., 1992, Phys. Lett. **B283** 155.
Roco, M, 1993, unpublished.
De Rujula, A et al., 1974, Phys. Rev. **D10** 1649.
Ryskin, M G, 1991, Sov. J. Nuc l. Phys. **53** 668.
Rutherford, E, 1911, Phil. Mag. **21** 669.
Schlein, 1993, 1993 EPS Conf. Marseille and UCLA-PPh0061.
Schuler, G, 1991, HERA Workshop 1991, Vol. 1, p. 131
Schuler, G and Terron, J, 1991, HERA Workshop 1991, Vol. 1, p. 599.
Schuler, G and Sjöstrand, T, 1993, Phys. Lett. **B300** 169; 1993, Nucl. Phys. **B407** 539.
SLAC-MIT collaboration, Riordan, E M et al., 1974, Phys. Lett. **B52** 249; see also SLAC-PUB-1634.
SLAC-MIT collaboration, Atwood, W B et al., 1976, Phys. Lett. **64B** 479.
Sokolov, A A and Ternov, M, 1964, Sov. Phys. Doklady **8** 1203.
Streng, K H, 1987, Proc. HERA Workshop vol. 1, 365, ed. by R. Peccei, and 1988, CERN TH 4949.
Taylor, R R, 1969, Proc. 4th Intern. Symp. Electron Photon Interactions at High Energies, p. 251, Daresbury, England, Daresbury Nucl. Phys. Lab.
TASSO collaboration, Brandelik et al., 1981, Phys. Lett. **107B** 290.
TASSO collaboration, M. Althoff et al., 1984, Phys. Lett. **138B** 219.
TERAD91, 1991, Akhundov, A et al., 1991, HERA Workshop 1991, 1285.
TOPAZ collaboration, Hayashii, H et al., 1993, KEK preprint 93-47.
UA1 collaboration, Arnison, G et al., 1983, Phys. Lett. **123B** 115.
UA1 collaboration, Albajar, C et al., 1990, Nucl. Phys. **B335** 261.
UA8 collaboration, Bonino, R et al., 1988, Phys. Lett. **B211** 239; Brandt, A et al., 1991, Proc. Joint Intern. Lepton - Photon Symp. and 1991 EPS Conf. High Energy Physics, Geneva, ed. by S. Hegarty, K. Potter, E. Quercigh, p. 741; Brandt, R et al., Phys. Lett. **B297** 417.
Voss, G-A, 1988, Proc. First Euro Acc. Conf., Rome, 1988, p. 7.
Watanabe, Y et al., 1975, Phys. Rev. Lett. **35** 898.
Weinberg, S, 1973, Phys. Rev. Lett. **31** 494.
Wiik, B H, 1982, Electron - Proton Colliding Beams, The Physics Programme and the Machine, Proc. 10th SLAC Summer Institute, ed. A. Mosher, 1982, p. 233; Proc. XXVI Int. Conf. High Energy Physics, Dallas, 1992.
Wolf, G, 1971, Nucl. Phys. **B26** 317.

ZEUS Collaboration, 1986, The ZEUS Detector, Technical Proposal (1986).
ZEUS collaboration, Derrick, M et al., 1992a, Phys. Lett. **B293** 465; 1992b, Phys. Lett. **B297** 404.
ZEUS collaboration, 1993a, The ZEUS Detector, Status Report 1993, ed. by U. Holm.
ZEUS collaboration, Derrick, M et al., 1993b, Phys. Lett. **B303** 183; 1993c, Phys. Lett. **B306** 158; 1993d, Phys. Lett. **B306** 173, 1993e, Z. Phys. **C59** 231; 1993f, Phys. Lett. **B316** 207; 1993g, Phys. Lett. **B315** 481; 1993h, Phys. Lett. **B316** 412; 1993i, DESY 93-151 and Phys. Lett. **B**, to be published.
ZEUS collaboration, Klanner, R, 1993j, 1993 EPS Conf. Marseille; Park, I, 1993k, ibid and DESY 93-186; Martin, J 1993 l, 1993 Lepton-Photon Conf. Cornell; 1993m, Abramowicz, H, Klanner, R and Martin, J, 1993, DESY 93-158.